Design Considerations for Maximizing Cooling Package Performance

Bhaskar Bhatnagar, Dan Schlesinger

Freightliner LLC, USA
bhaskarbhatnagar@freightliner.com

Abstract More stringent heavy vehicle emissions legislation demands considerably higher performance out of engine cooling systems. Presented is a study of various design parameters that can be used to maximize the cooling airflow for a Freightliner Class 8 truck. CFD analysis was used to analyze various fan shroud profiles, different fan immersions (overlap between the fan and fan shroud) and with two different engines. All of these design parameters lead to significantly different flow behavior inside the fan shroud and in the underhood region, in turn creating adverse or favorable pressure gradients. A series of isothermal CFD simulations are used to determine the effects of these flow characteristics on the radiator mass flow. For one of the simulation setup the predicted radiator coolant inlet temperature is compared to measured physical test data at different fan speeds. The methodology for the optimization of the cooling performance is outlined. It is shown that the presented simulation approach can provide accurate predictions of cooling airflow and coolant temperature.

Optimization and Correlation of a Class 8 Truck Cooling System

Clinton Lafferty, Kevin Horrigan, Ales Alajbegovic

Volvo Trucks North America, USA
clinton.lafferty@volvo.com

Abstract Development in engine technology to meet recent heavy vehicle emissions legislation has increased the demand on heavy vehicle cooling systems. The use of PowerFLOW®, a commercial computational fluid dynamics (CFD) software, allows a product development team to access a variety of cooling system improvements with no impact to the vehicle external appearance. This paper provides an overview of the PowerFLOW® modeling process and the results for several studies involving modifications to engine and cooling system parts. The design changes include the repositioning of the exhaust gas recirculation (EGR) cooler, changes to the fan diameter and position, and modifications to the exit shape of the shroud. Initial work focused on increasing cooling air mass flow and used a body force fan model with isothermal calculations. Results indicated only minimal changes with the EGR cooler repositioning, however, fan modifications resulted in a 13 percent cooling air massflow increase. The impact of the fan shroud exit shape on fan blade tip loss was computed with a multiple reference frame (MRF) fan model. Finally a detailed cooling system correlation study was performed involving a comparison to isothermal air mass flow rates and later thermal calculations involving heat exchangers modeled with PowerCOOL®.

Aerodynamic Improvements and Associated Energy Demand Reduction of Trains

Alexander Orellano and Stefan Sperling

Bombardier, Center of Competence for Aerodynamics and Thermodynamics, Germany,
Alexander.orellano@de.transport.bombardier.com

Abstract The importance for developing energy efficient rail vehicles is increasing with rising energy prices and the vital necessity to reduce the CO_2 production to slow down the climate change. This study shows a comparison of different train types like regional and high-speed trains and provides estimation for improvements of the aerodynamic drag coefficient. Out of this estimation an assessment of the associated energy reduction is shown taking into account typical operational cycles with acceleration, constant speed and deceleration phases. Traditionally, aerodynamic improvements of high-speed trains were in the focus of the engineering community as the resistance to motion is increasing with the square of the velocity. However, this study reveals that it is necessary to consider regional and commuter applications equally. This transport sector is not only the one with the highest share in the market but exhibits also much higher potential for aerodynamic improvements then present day already optimized high-speed trains.

1 Introduction

In order to focus the engineers attention to the dominant and therefore relevant area related to energy demand reduction it is necessary to first get an overview of the energy fluxes and to fix the boundaries and the scope of the investigation. Figure 1 shows one specific example of the distribution of the traction energy demand of an electrical multiple unit covering the energy flux from the power supply substation up to a specific train within the line. A substantial portion of the energy provided by the substation to the line is already lost on the way to the train. The energy demanded by the train can be subdivided into a part which dissipates to heat and a part that is converted to kinetic energy due to the momentum gained by the accelerated mass of the train. The part of the energy dissipated to heat is marked with E_{Vd}. The most important contributors to this part are the aerodynamic drag and the losses of the traction system including the cooling devices. This energy is usually not used anymore and is released to the environment. Principally it would be possible to convert these cooling losses back to electrical energy by an appropriate thermodynamic process like Clausius-Rankine or heat absorption process. Nevertheless, the efficiency cannot be higher then the Carnot process [1]. The temperature difference of the cooling liquid (usually water) to the environment ranges from 50 to 80 Kelvin which limits the theoretical efficiency of the thermodynamic process to be not greater then around 20 % which would lead to efficiencies around 10 to 15 % in a practical application. This fact prevents an economically justified operation of such a device for water cooling systems of trains. The part of the energy converted to kinetic energy can more easily be converted back to electrical power in conjunction with regenerative braking. This is common practice in most mainline applications. The rate of energy recovery during braking is dependent on the voltage, the relative number of driven axles and the capability of the substations control. The part of the kinetic energy which cannot be transferred back to the line is being dissipated in the brake resistor (E_{BR}). This analysis of the losses helps to determine the dominant terms of energy losses. However, when it comes to implementation of energy demand reduction technology it is important to analyse the decrease of energy demand related to the operational boundary conditions including speed profile, altitude profile and environmental temperatures. The losses can be divided in the following components:

- E_{VI} infrastructure losses
- E_{Vd} driving losses
- E_{Vb} braking losses
- E_{BR} brake resistor losses

The scope of the present investigation is to analyse the potential to reduce the driving losses of the train by reducing the aerodynamic drag of the train. It should be also noted that the analysis shown does not comprise the energy used for the auxiliaries of the train as e.g. the HVAC system. The energy demand for the HVAC system is extremely dependent on the application and on the external atmospheric boundary conditions and is not within the scope of the present investigation. The investigation presented here is thus restricted to the driving losses only.

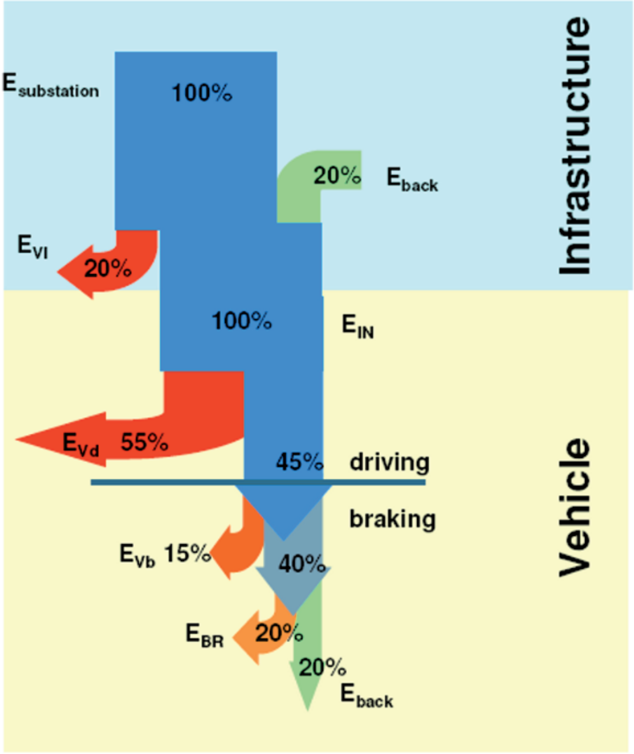

Fig. 1 Traction energy demand distribution.

2 Running Resistance

The total running resistance can be approximated by a quadratic approach, i.e. the Davis Formula [2]

$$R = a+b * v + c * v^2 + d + e \tag{1}$$

$R[N]$ is the total running resistance in Newton
$v[km/h]$ is the train speed
$a[N]$, $b[Nh/km]$, $c[Nh2/km2]$ are the Davis coefficients
$d[N]$ is the curve resistance and
$e[N]$ is the slope resistance

The term a represents the mechanical rolling resistance. The term b is linearly dependent on the velocity and reflects the mechanical resistance and momentum losses due to air mass exchange of the train with the environment. The momentum losses are mainly associated with the power needed to accelerate the air taken in to the speed of the train. The term c represents the classical aerodynamic drag which consists of the skin friction and the pressure drag. Typical contributors for the aerodynamic drag are [3]

- head and tail loss
- skin friction
- bogies
- protruding objects
- pantographs
- inter-car gaps
- ventilated brake
- underbelly friction

From an engineering point of view it is important to first determine the various contributions to the drag coefficient of the vehicle under investigation. The general train data for the regional and high-speed train considered within this study is given in Table 1.

Table 1 General data of investigated trains

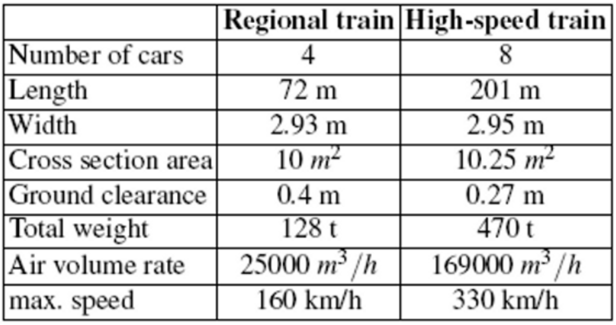

	Regional train	High-speed train
Number of cars	4	8
Length	72 m	201 m
Width	2.93 m	2.95 m
Cross section area	10 m^2	10.25 m^2
Ground clearance	0.4 m	0.27 m
Total weight	128 t	470 t
Air volume rate	25000 m^3/h	169000 m^3/h
max. speed	160 km/h	330 km/h

2.1 Rolling Resistance

The velocity independent Davis coefficient a represents the force which is necessary to roll the train at zero speed on a track. An illustrative model for the A-coefficient refers to a small slope for the wheel to climb (see Fig. 2). The wheel and rail surfaces deform due to the axle load at the point of contact. Accordingly, the superstructure of the track deforms in a similar way. The magnitude of this deformation depends predominantly on the axle load and the properties of the involved material of the track and the wheel.

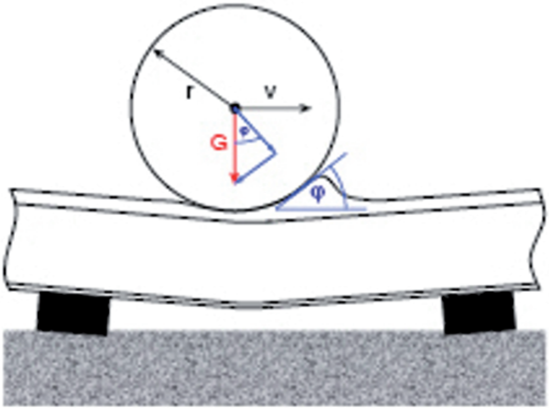

Fig. 2 Rolling resistance [3].

2.2 Momentum Resistance

The mechanical resistance scales linearly with the train velocity. The term is separated into two different parts; i.e the actual mechanical resistance (b_1) and the air momentum drag (b_2). The corresponding parts of the Davis formula read

$$b = b_1 + b_2. \tag{2}$$

The b_1-term supplements the rolling resistance with respect to modelling the wheel/tracksliding friction including brake and transmission drag, the resistance of friction bearings, friction inside gear units and suspension-drag contributions. b_1 depends on the specific track design and details of the suspension and transmission. The air-momentum drag coefficient b_2 is dependent on the following parameters: brake drag, transmission losses and air momentum drag. The air momentum drag is the energy required to accelerate the mass of air intake, e.g. cooling, air conditioning, etc. to the speed of the running train. Thus, b_2 exclusively hinges on the amount of exchanged air.

2.3 Aerodynamic Resistance

The coefficient for the aerodynamic drag is calculated as follows:

$$c_d = \frac{F_x}{0.5 * \quad * V^2 * A} \tag{3}$$

Where F_x is the force in driving direction, is the air density, V denotes the driving speed and A represents the reference area which is standardized to be $10m^2$ within the train aerodynamics community [4]. Note that the non-dimensional c_d value is not the same as the c value with dimensions within the Davis formula described above. The formula to derive the c_d value out of the Davis coefficient is

$$c_d = c_{Davis} * 2 * 3.6 * 3.6 / (\rho * A) \tag{4}$$

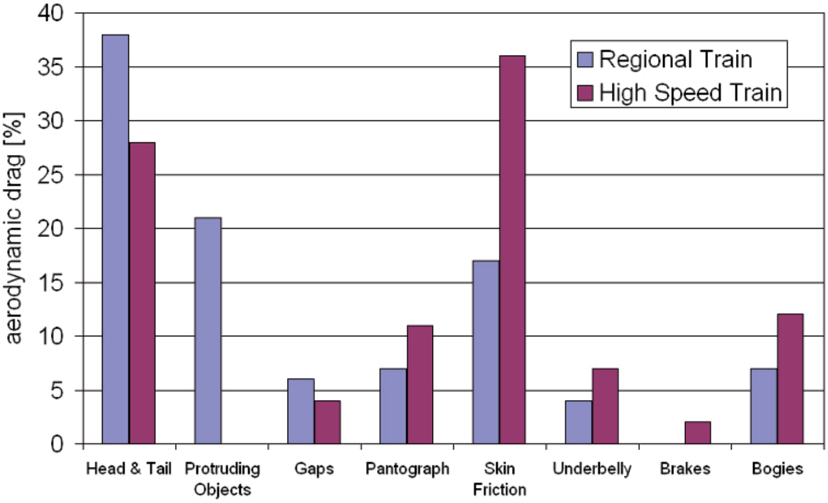

Fig. 3 Typical drag distribution for high-speed trains and regional trains.

Figure 3 gives a general overview of the specific contributions of the different components of a typical regional and high-speed train. The figures presented in the graph are highly dependent on the specific train under investigation. Nevertheless, a typical and electrical or Diesel multiple unit (see Fig. 4) exhibits objects, like HVAC, motor coolers, transformers, inverters and other equipment which are usually sticking out of the body shell and which are a major source of drag compared to a typical electrical multiple unit high-speed train with smooth surfaces and integrated components (see Fig. 5). The ratio between the surface of the train perpendicular to the flow direction, i.e. side walls, roof and underbelly, and the cross section area determines the relative importance of the skin friction. Thus, for high speed trains with approximately 200 m length it is the skin friction which dominates the drag. The drag of the regional train investigated here with 4 cars is dominated by the front and tail drag and the drag generated by the unshielded roof equipment. However, it should be noted that the drag value of one specific part of a train is highly influenced by the incoming flow and thus dependent on the surrounding flow which is influenced by near by objects. The engineering approach to derive the total drag by summarising the individual drag of different components is not taking into account this interrelationship.

Fig. 4 Talent II, modern electric multiple unit regional train.

Fig. 5 ICE3, electric multiple unit high-speed train.

3 Energy Demand for Typical Driving Cycles

3.1 *Regional Traffic*

The parameters of the regional train used in this study are listed in Table 1. To quantify the effect of reducing the aerodynamic coefficient on the energy consumption for regional traffic a driving cycle has been taken into account. This study focuses on Dortmund to Münster with 10 stations and 51 minutes journey time according to the time table of the German operator "Deutsche Bahn". Figure 6 shows the velocity of the train over the time. The total journey time is in our study 12 minutes shorter than the time table of the German operator "Deutsche Bahn" is telling. The station stopping time is in both cases the same (360 seconds). Therefore, the maximum velocity of the train used by the German operator "Deutsche Bahn" is not going up to 160 km/h.

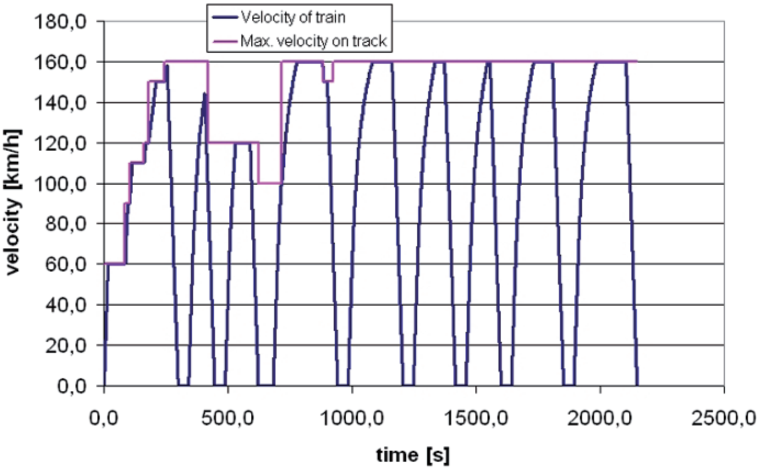

Fig. 6 Velocity profile of a Regional Train running up to 160 km/h.

However, the speed profile (see Fig. 6) shows a relatively short time where the train is running at maximum speed of 160 km/h which diminishes the importance of the aerodynamic drag and increases the relative importance of mass slightly related to the energy demand. Figure 7 shows the effect on the energy demand of the train dependent on the aerodynamic drag. A typical 70 m long regional train exhibits drag values around c_d =1.1. Furthermore, Fig. 7 shows the traction energy, regenerated energy and the total energy. The traction energy herein stands for the energy that can be metered between the line and the train. The regenerated energy is the energy that can be fed back to the line while the train is braking. Therefore the train has to be equipped with electrical brakes. Last but not least, the total energy is the difference between the traction energy and the regenerated energy.

Figure 7 shows the impact of the aerodynamic drag on the energy demand of the regional train running on the reference line described above. It can be seen that approximately one third of the aerodynamic drag reduction in percentages can be saved in energy for the traction effort. Thus, the relative importance of reducing the drag of a regional train is lower compared to a high-speed application.

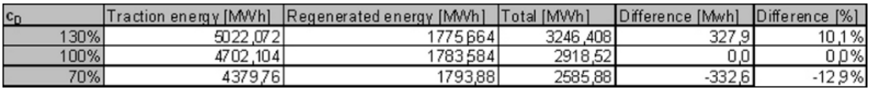

c_D	Traction energy [MWh]	Regenerated energy [MWh]	Total [MWh]	Difference [Mwh]	Difference [%]
130%	5022,072	1775,664	3246,408	327,9	10,1%
100%	4702,104	1783,584	2918,52	0,0	0,0%
70%	4379,76	1793,88	2585,88	-332,6	-12,9%

Fig. 7 Impact on the energy demand by varying the aerodynamic drag.

3.2 High-Speed Traffic

In order to quantify the effect of reducing the aerodynamic coefficient on the energy consumption a driving cycle has been taken into account with in a manner analogous to the regional train example above. This study focuses on Frankfurt to Köln (Cologne) with 6 stations and 83 minutes journey time according to the time table of the German operator “Deutsche Bahn”. Despite the fact that this stretch is part of the high-speed line in Germany it should be noted that it exhibits a relatively high number of stops within a short distance. Therefore, the speed profile (see Fig. 8) shows a relatively short time where the train is running at maximum speed of 300 km/h. This is particularly important as the relative importance of the aerodynamic performance of the train related to energy demand is determined by the speed of the train and by the frequency of stops. The higher the top speed and the lower the number of stops the more important becomes the aerodynamic drag. Figure 9 shows the effect on the energy demand of the train dependent on the aerodynamic drag. A typical 200 m long high-speed train exhibits drag values around c_d = 1.1 [5]. On the right coordinate the impact on the journey time is also displayed. The journey time decreases with decreasing aerodynamic drag as the train is able to accelerate better with reduced drag.

Figure 10 shows the impact of the aerodynamic drag on the energy demand of the train running on the reference line described above. It can be seen that approximately half of the aerodynamic drag reduction in percentages can be saved in energy for the traction effort.

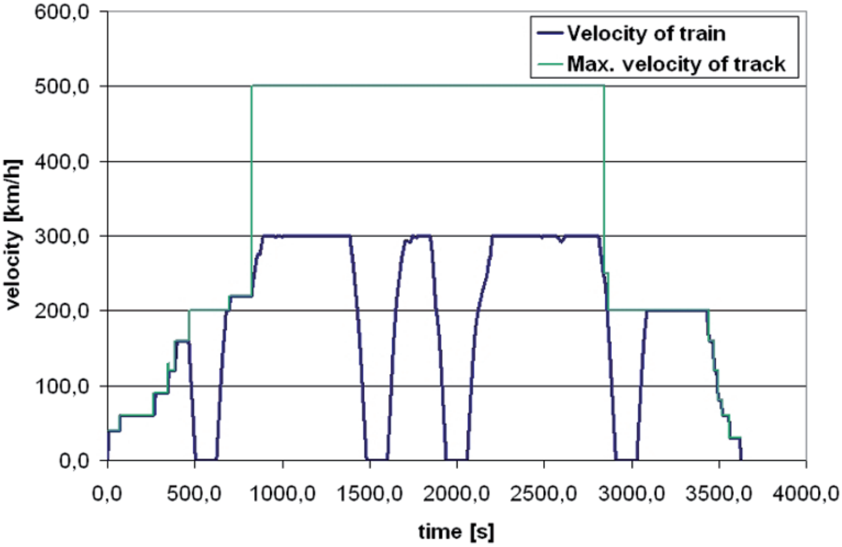

Fig. 8 Velocity profile of a High-Speed Train running up to 300 km/h.

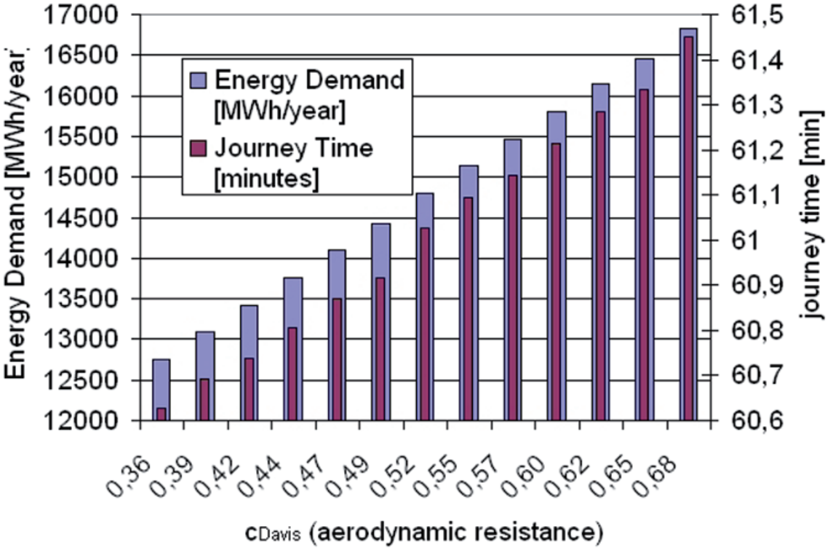

Fig. 9 Impact of the aerodynamic drag on the energy demand and the journey time.

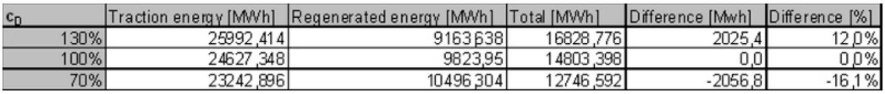

c_D	Traction energy [MWh]	Regenerated energy [MWh]	Total [MWh]	Difference [Mwh]	Difference [%]
130%	25992,414	9163,638	16828,776	2025,4	12,0%
100%	24627,348	9823,95	14803,398	0,0	0,0%
70%	23242,896	10496,304	12746,592	-2056,8	-16,1%

Fig. 10 Impact on the energy demand by varying the aerodynamic drag

4 Potential for Reducing the Energy Demand by Drag Reduction

The potential for reducing the drag depends on the train type and on the vehicle chosen for reference. Nevertheless, the author will try to quantify the potential in terms of percentages of reduction of drag related to present day solutions that can be found on the track. The estimated drag reduction potential for a regional train is shown in Fig. 11. The biggest potential for improvements can be achieved by an optimisation of the head and the tail of the train. The tail drag can be reduced by reducing the longitudinal vortices which are produced at the tail of a regional train and by introducing a boat tailing shape in order to recover the pressure to certain extend. The longitudinal vortices can be reduced by either forcing a separation near to the position where they are produced (spoiler) or by keeping the pressure gradient in the circumferential direction as low as possible which can be achieved by a proper front shape. The potential to reduce the overall drag of a regional train is estimated to be around 20-25 %. This drag reduction would lead to an energy reduction of about 6-8 %. This in turn would lead to an energy saving of about 200 MWh/year and train. The assumption is that this train is running 17 hours per day on 360 days per year.

In terms of high-speed trains (see Fig. 12) the potential for improvement is not as big as for regional trains due to the fact that this type of trains has already received much attention from the aerodynamic community. Nevertheless, the highest potential is seen to be the head and tail and a proper design of the bogie cutout in conjunction with bogie fairings [6]. The potential for a reduction of the aerodynamic drag of a high-speed train is estimated to be around 14 %. This would lead to energy demand reduction of about 6-8 %. Thus, the potential to reduce the energy demand by improving the aerodynamics performance is the same for high-speed trains as for regional trains.

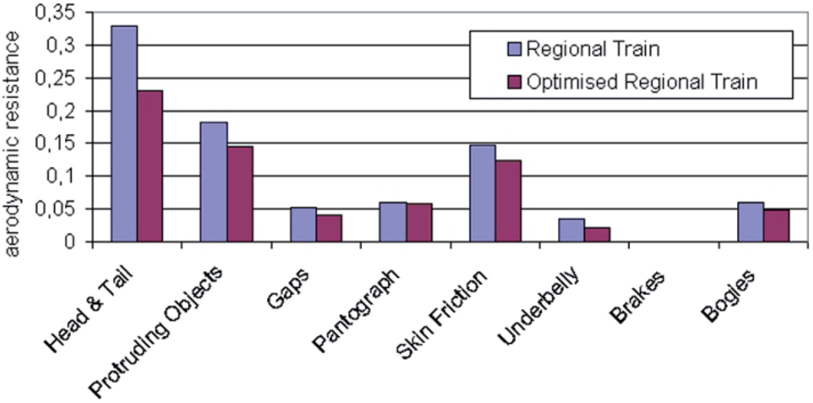

Fig. 11 Estimated potential for reducing the drag of a regional train

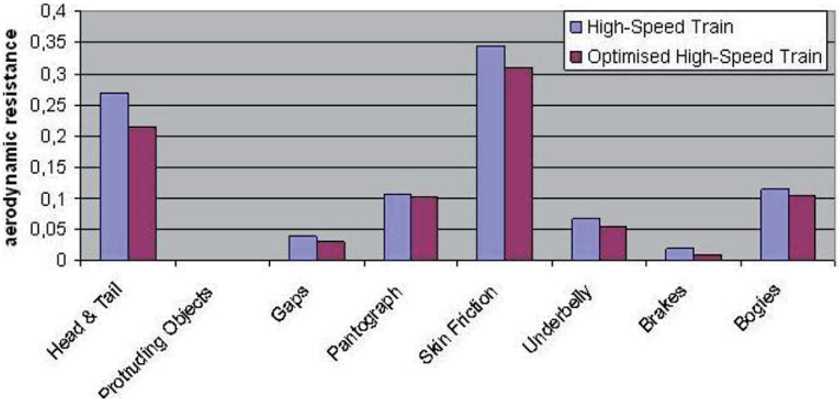

Fig. 12 Estimated potential for reducing the drag of a high-speed train

5 Conclusions

The present study shows that when it comes to energy reduction it is first important to know the distribution of the losses of the various components in order to focus the attention to the dominant losses. Secondly, it is important to define an operational cycle and proper boundary conditions in order to be able to simulate the effect of implementing technical measures on the averaged energy demand during a typical operational cycle. This study shows that a considerable amount of energy is being dissipated to heat and therefore lost due to the aerodynamic resistance of a train. Additionally, this study shows that aerodynamic drag is not only important for high-speed train applications but that the reduction of aerodynamic drag is equally important for regional train applications. This is due to the fact that the potential for reducing the drag of a present day high-speed train is considerably lower then the potential of a reducing the aerodynamic drag of a present day regional train.

References

[1] H.D. Baehr, S. Kabelac, *Thermodynamik, Grundlagen und technische Anwendungen,* 13th ed. (Springer Verlag, 2006)

[2] Davis, W.L.: General Electric Review (1926) 3. T. Schill, *Rechnerbasierte Fahrwiderstandsprognose von Schienenfahrzeugen*, Student thesis (TU Berlin and Bombardier, 2004) 4. European Norm, EN 14067-4 Railway Applications. Aerodynamics. Requirements and test procedures for aerodynamics in open track, 2005 5. Peters, J.L.: Windkanaluntersuchungen zum Widerstandsverbesserungspotential von konstruktiv abgesicherten Drehgestellsch¨urzen und Dachgeräteverkleidungen am ICE

[3] Technical report, (Krauss Maffei Verkehrstechnik. August 1996) 6. Peters, J.L.: Aerodynamics of very high-speed trains and maglev vehicles: State of the art and future potential. Int. J. of vehicle design. Special Publication SP3, 308–341

[4] European Norm, EN 14067-4 Railway Applications. Aerodynamics. Requirements and test procedures for aerodynamics in open track, 2005

[5] Peters, J.L.: Windkanaluntersuchungen zum Widerstandsverbesserungspotential von konstruktiv abgesicherten Drehgestellschürzen und Dacheräteverkleidungen am ICE 3. Technical report, (Krauss Maffei Verkehrstechnik. August 1996)

[6] Peters, J.L.: Aerodynamics of very high-speed trains and maglev vehicles: State of the art and future potential. Int. J. of vehicle design. Special Publication SP3, 308–341 (1983)

The use of Aeronautical Experimental Facilities and Measurement Techniques for the Aerodynamic Investigation of High Speed Trains

Andreas Dillmann

German Aerospace Center (DLR), Germany
andreas.dillmann@dlr.de

Abstract The development of future high speed trains is driven by commercial and ecological requirements which determine the increase of speed and payload while reducing weight and improving thermal and acoustical passenger comfort. To ensure the same level of safeness then for today's rolling stock, additional issues like Reynolds-Number and Mach-Number dependencies have to be explored. The influence of unsteady flow phenomena as well as the impact of the train's induced flow field on humans and infrastructure has to be investigated. For this purpose, special experimental facilities and techniques originally developed for aeronautical research proved to be extremely useful. For the investigation of viscous flow effects like separation and other boundary layer phenomena, a pressurized wind tunnel can realize high Reynolds numbers without entering the compressible flow regime. Validated results for the Göttingen high pressure wind tunnel show that it is possible to use extremely small models, down to a scale of 1:100, and to get good results if the accuracy of the model manufacturing process is high enough. A second possibility to increase the Reynolds number in a wind tunnel is to cool down the working fluid, thus increasing the Reynolds number up to a factor of 5.5. The main advantage of cryogenic wind tunnels is the possibility of independent adjustment of the Mach and Reynolds number. A third possibility to increase the Reynolds number is to change the working fluid of the facility, e.g. by using water instead of air. Advanced measurement techniques, which were originally developed for aeronautical research, allow a deep insight into the physical mechanisms governing the aerodynamic performance of high speed trains. A broad variety of experimental results is presented, showing that high Reynolds number facilities are in many cases an indispensable research tool for the aerodynamics of railroad vehicles.

Reduction of Skin-Friction Drag on a Generic Train Configuration

Sigfried Loose

German Aerospace Center (DLR), Germany
sigfried.loose@dlr.de

Abstract Wind-tunnel experiments were carried out to determine the drag-reduction potential of dimpled surfaces on a generic train model as well as the influence of the dimpled surface on the flow field. Forces and moments were measured with an external six component balance. The flow field investigation was done by use of particle image velocimetry (PIV). The measurements were executed over a wide range of Reynolds numbers in a cryogenic wind tunnel. The use of this wind tunnel allows the variation of Reynolds number while the Mach number remains constant and vice versa. The experiments were undertaken with a standard set up i.e.: the models consist of a complete end car and half mid car (Model scale 1:20); a fresh boundary layer on the ground realized by splitter plate; no force closure between mid car and end car. Two similar models were investigated. The first model was manufactured with a smooth, polished surface. The second model was similar to the first but with a dimpled surface. The dimples were circularly shaped and arranged in a certain pattern. The results of force measurements show for some configuration, depending on the Reynolds number, an overall drag reduction of more than 20%. In consideration of the fact that the total drag of the investigated configurations is mainly determined by friction drag this drag reduction can only come from a decrease of skin friction drag. To ensure that this interpretation is correct, pressure measurements were done in the intercarriage gap for all configurations. The influence of the dimpled surface on the flow field is directly visible at the leeward vortex system, which is resulting from the flow under yaw angles. All characteristic values of the vortex become weaker than for the non dimpled configuration.

Head Pressure Effects of Trains and Locomotives – Engineering Calculation Approaches for Homologation Purpose

Arnd Rueter

Siemens AG, Transportation Systems, Germany
arnd.rueter@siemens.com

Abstract The head pressure pulse and the head pressure drop of a train are the pressure signals measured during the passage of the first few meters of the train at a fixed position in open air or in a tunnel, respectively. Train pressure pulses are part of the pressure loading on objects (like other trains) and persons. A new train is admitted to operation if measured data statistically satisfies certain threshold values. Nowadays train homologation in Europe predominantly relies on measurements, yet appropriate prediction tools are needed during the engineering process. The described pressure effects are well reported in literature and calculation methods are available providing for adequate accuracy. The methods are reviewed, examples from engineering applications and comparisons to data from full scale measurements are presented. The prevalent flow features are discussed covering a typical range of vehicle shapes and operational conditions (regional to high speed). The use of CFD methods is evaluated. The modeling error is estimated and error mitigation is attempted. A virtual homologation approach is proposed. The open fields of the issue are outlined.

Numerical Analysis for Aerodynamics of High-Speed Trains Passing Tunnels

Jing Zhao, Renxian Li

National Key Laboratory of Traction Power, Southwest Jiaotong University, China
zhaojing_555@sina.com

Abstract High-speed trains running at 200~350km/h will be operated on Chinese high-speed railways after 2010. Some of the high-speed railways in China will be built in mountainous areas. Many tunnels have to be constructed for the railways. However, the tunnel aerodynamic effect of high-speed trains is not very clear, especially the aerodynamic influence when the train is running in or out of tunnels. Examples are the effect of air pressure impulse on the train window strength and on the ear films of passengers, the relationship between the tunnel section size and the aerodynamic force acted on the train body, the relationship between the buffer structure of the tunnel entrance and the intensity of air pressure impulse, and so on. Based on Reynolds average Navier-Storkes equations of viscous incompressible fluid, and on two equation turbulent models, the aerodynamic effect of high-speed train in tunnels was investigated by means of the technology of moving grids in computational fluid dynamics method. Flow fields of high-speed train for 4 running speeds (200, 250, 300, 350km/h), 3 sizes of tunnel sections and 2 kinds of buffer structures for tunnel entrance were calculated. The results show that the aerodynamic effect of the tunnel's blockage ratio is larger than that of train's speed when the tunnel section size is smaller than a finite blockage ratio; the buffer structure for a tunnel entrance may reduce the aerodynamic influence effectively. Based on the simulation results of the investigation, some suggestion values between tunnel blocking ratio and train running speed were presented.

A Study of the Influence of Aerodynamic Forces on a Human Body near a High-Speed Train

Renxian Li, Jing Zhao and Shu Zhang

School of Mechanical Engineering, Southwest Jiaotong University, Chengdu, P. R. China
rxli@swjtu.edu.cn

Abstract A study of the influence of aerodynamic force on human body near the high-speed train was completed by the means of the technology of moving grids in computational fluid dynamics method. 60 running situations, which includes 3 types of locomotive shape, 4 running speeds of train combining 5 distances from human body to the sidewall of the train (human-train distances), were simulated. The 4 running speeds are 200km/h, 250km/h, 300km/h and 350km/h. The 5 human-train distances are 1.0m, 1.5m, 2.0m, 2.5m and 3.5m. The study results show that the aerodynamic force acting on human body strongly affected by the shape of the passing train head. The aerodynamic force produced at 1.0m human-train distance by extremely blunt train head at 350km/h speed is 7 times more than that produced by a streamline train head at the same operating condition. With an increase of human-train distance, the differences among the aerodynamic forces produced by the different shape of train head decreases. The decrease is about a quadratic function of the human-train distance, and has nothing to do with train speed. The ratio of the maximum aerodynamic force produced by train head and that produced by train tail at a given human-train distance is about a constant and independent of train speed. The ratio of the maximum aerodynamic forces for any two different human-train distances produced by train head or train tail is about a constant and has nothing to do with train speed. The direction of the aerodynamic force acting on the human body is nearly the same in different running conditions independent of train head/tail shape. The direction of the aerodynamic force changes over 300 degrees when train head or train tail passes. Based on the calculation results, formulas for calculating the aerodynamic force acting on the human body and the maximum wind speed near the human body were presented. Safety distances for people walking or working near passing train were recommended.

1 Introduction

The operation of high-speed trains in the world provides a convenient, quick, safe and cheap way to travel for ordinary people in the high population density area. Since the first high-speed train was operated successfully in Japan in *1960s*, the high–speed trains of *200km/h* or faster have operated in Germany, France, Italy, United Kingdom and Sweden. The technology improvements in railway construction and railway vehicle manufacture make possible very high running speeds. In tests, the running speed of the French train *TGV* reaches *574km/h* while its operation speed is over *300km/h*. For the German high-speed train *ICE*, its test running speed is *406.9km/h* and its operating speed is over *250km/h*. Right now, there are many high-speed railways under construction in China and trains with running speeds over *200km/h* will be operated in the near future. According to the railway development program, about *12000* kilometers of high-speed railway will be built in the coming *15* years in China.

Many aerodynamic problems will be produced by the operation of high-speed trains, however. Some unfavorable influences on trains will emerge due to interaction of running train and surrounding air, such as aerodynamic drag and aerodynamic pressure waves acting on the train body caused by surrounding buildings. Many experimental and simulation studies have been done in this area[1~7]. There will also be adverse effects on the surrounding environment and persons near the railway due to induced air flow caused by passing trains. Most importantly, the air flow induced by high-speed trains (train wind) may impose some safety issues on people near high-speed railways.

Generally speaking, the strength of train wind will decrease with the distance increase between human body and trains, but what constitutes a safe distance for people to walk or work near high-speed railway? The standard of safety distance is different in different countries for high-speed trains. The average train wind velocity near the human body is used as a criterion to determine the safety distance in United Kingdom and Japan[8]. *9m/s* train wind velocity is used to determine platform safety distance in Japan. In the United Kingdom *25mph(≈11.1m/s*) train wind velocity is used to determine the platform safety distance and *38mph(≈16.9m/s*) train wind velocity is used to determine the safety distance for railway employees. Aerodynamic force is used as a criterion to decide the safety distance in Germany and in France[9]. The safety distance is defined as that for which a *100N* maximum allowed aerodynamic force acts on a human body. In the USA, the aerodynamic pressure acting on the ear drum (*0.2psi*) or train wind velocity about Beaufort number *7* is used to decide the safety distance.

In China, there is no corresponding standard for safety distance yet. Despite that it is a task of human safety engineering to draft the safety distance standard; it is an important prerequisite to understand the patterns of the aerodynamic forces acting on the human body as a function of train speed and distance between train and human before setting the standard.

The aerodynamic effect of train wind on the human body and surroundings is produced by the relative motion between the train, the air, and the surrounding objects. It is difficult to model this kind of flow field in wind tunnel because of the relative motion between the train and its surroundings. Real measurement around operating trains have been performed using instrumented human models by scientists of Japan, France and China[11~13]. These experiments were expensive and had many limitations, such as the condition of railways, maintaining the train velocity through the measurement point, the operation condition of test line and so on. Moreover, the measurement results exhibited dispersion in the survey data. Therefore, it is quite difficult to get accurate aerodynamic influence data using field measurements. Simulation by means of computational fluid dynamics is another method to study the vehicle aerodynamic problems. It has no limitation for train operating condition; it is convenient to compare the aerodynamic influence for different operating conditions and is less expensive than field experiments.

There are still some difficulties to simulating a flow field around bodies in relative motion. In early attempts, researchers first computed the wind field data near the train head using various CFD methods, and then estimated the force acting on a human body based on distribution of fluid velocity and pressure. Nevertheless, presence of the human body has an effect on the distribution of velocity and pressure of the train flow field. The moving train and human bodies should be simulated simultaneously and the relative motion between the train and human bodies should be simulated. In this paper, aerodynamic influence acting on human body near high-speed train was studied based on the moving mesh simulation method in CFD.

2 Methodology

2.1 Basic hypothesis

(1) Because Reynolds number of flow field around the high-speed train is larger than 10^6 due to the train running at high speed, the fluid is in turbulent state. The $k \sim \varepsilon$ two equation turbulent model has been used in the simulations.

(2) Train speed ranges *200~350km/h* in this study, and the flow velocity of induced air around the train is less than Mach *0.3*, so the flow is assumed to be incompressible.

(3) Some detail structures on vehicle body have been ignored to simplify the calculations, (e.g. pantograph, bogies, link section of carriages and the like).

(4) Shape of human body is too complicated to simulate. Some cylindrical bodies were used to model human bodies in this project following previous re-

search[14~16]. Height and diameter of the cylindrical body is set to *1.75m* and *0.45m* respectively. If these two size express height and shoulder width of human body, this cylindrical body simulates *90%* of Chinese adults.

2.2 Mathematical model

Based on Reynolds average Navier-Stokes equations of viscous incompressible fluid and *k~ε* two equations turbulent model, the flow field around train can be described as

$$u_{j,j} = 0 \tag{1}$$

$$\rho u_{j,t} + \rho u_j u_{i,j} = -p_{,i} + (\mu + \mu_t)(u_{i.jj} + u_{j,ij}) \tag{2}$$

$$\rho k_{,t} + \rho u_j k_{,j} = (\mu + \frac{\mu_t}{\sigma_k}) k_{,jj} + \mu_t G_k - \rho \varepsilon \tag{3}$$

$$\rho \varepsilon_{,t} + \rho u_j \varepsilon_{,j} = (\mu + \frac{\mu_t}{\sigma_\varepsilon}) \varepsilon_{,jj} + c_1 \frac{\varepsilon}{k} \mu_t G_k - \rho c_2 \frac{\varepsilon^2}{k} \tag{4}$$

Where

$$G_k = (u_{i,j})^2 + u_{i,j} u_{j,i} , \qquad \mu_t = \rho c_\mu \frac{k^2}{\varepsilon}$$

u_j —— Velocity component of flow field (m/s);

p —— Pressure (Pa);

μ —— Dynamic viscosity coefficient (N·s/m^2);

ρ —— Density (kg/m^3);

μ_t —— Turbulent viscosity coefficient (N·s/m^2)；

□ —— Turbulent kinetic energy (J/kg)；

ε —— Dissipation rate of turbulent kinetic energy (J/kg)；

$C_1, C_2, C_\mu, \sigma_k, \sigma_\varepsilon$ —— Constants，as *1.44, 1.92, 0.09, 1.0, 1.3*

The equations (1) to (4) were solved by finite volume method[18, 19].

2.3 Geometric model

The train is modeled as a *60m* long vehicle with same shape at the head and tail. Three cylindrical bodies, to model the human body, were put on one side of the train at the head and tail respectively. Three types of train head/tail shapes were modeled. Model 1 is a streamline head/tail shape; with a head/tail length of *8m*.

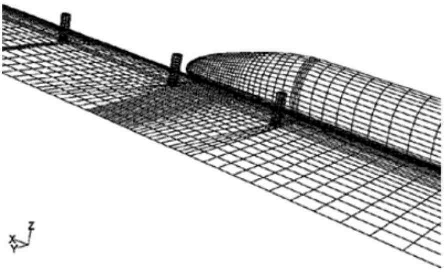

Fig. 1 A part of calculation mesh for model 1

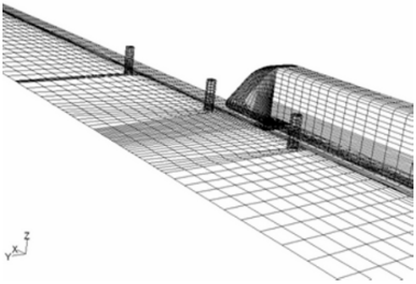

Fig. 2 A part of calculation mesh for model 2

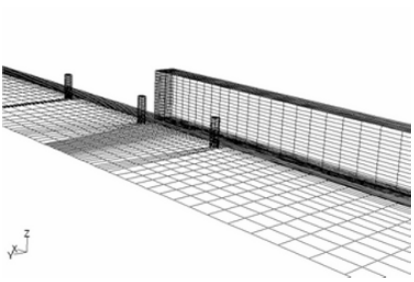

Fig. 3 A part of calculation mesh for model 3

Model 2 is a train with a fairly blunt head, with head/tail length of *3.9m*. Model 3 is an extremely blunt head train model having a length of *0m*. A part of the three train models calculation mesh is shown in Figs. 1 to 3 respectively. Length, width and height of the three train models were exact the same and are summarized below:

	Train length (*l*)	Train width (*b*)	Train height (*h*)	Length of changeable section at head/tail (*s*)
Model 1	60m	3.1m	3.7m	8.0m
Model 2	60m	3.1m	3.7m	3.9m
Model 3	60m	3.1m	3.7m	0.0m

3 Numerical calculation and result analysis

3.1 Calculation cases

In order to study the aerodynamic forces acting on a person near a high-speed railway, computational simulations of *4* train running speeds (*200km/h, 250km/h, 300km/h, and 350km/h*) and *5* human-train distances (*1.0m, 1.5m, 2.0m, 2.5m, and 3.5m*) were performed. 20 calculation cases were simulated for each train model for a total of cases simulated for the three train models. The effective moving distance of train relative to one cylindrical body was *33.75m* in each of the simulations. Mesh moving distance for each time step was *0.125m*. This means that *270* effective time steps were performed in each calculation case.

3.2 Simulation result analysis

3.2.1 Analysis of aerodynamic force acting on human body with different train shapes

Calculation result shown that there is a big effect for aerodynamic force acting on human body due to train wind produced by different train head/tail. Change tendency of aerodynamic force in horizontal direction produced by 3 model train head at *1.5m* human-train distance are shown in Figs. 4 to 6

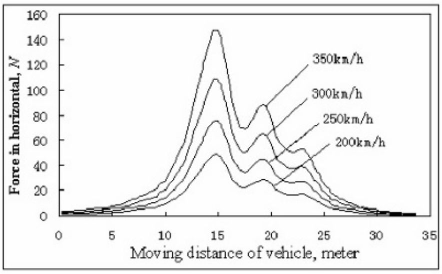

Fig. 4 Aerodynamic force acting on human body as train model 1 head passes

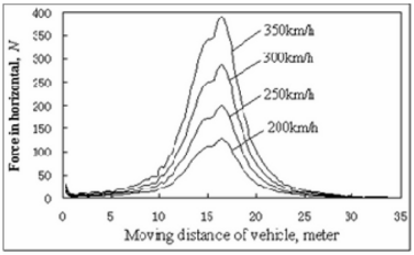

Fig.5 Aerodynamic force acting on human body as train model 2 head passes

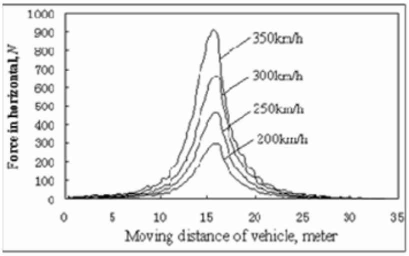

Fig.6 Aerodynamic force acting on human body as train model 3 head passes

Figures 4~6 show that, for the aerodynamic force acting on a human body produced by different train head shapes, not only there are big differences in value, but also there is a difference in the time over which the force acts. Comparing the change of aerodynamic force with different train head shapes, we find that the blunter the train head shape is, the larger the aerodynamic force acting on human body, and the shorter the acting time of the force. When different shapes of train tail pass, change in aerodynamic force is similar to the changes as train head passes. Figure 7~9 shown the change tendency of aerodynamic force produced by train tail of the 3 models at *2.5m* human-train distance.

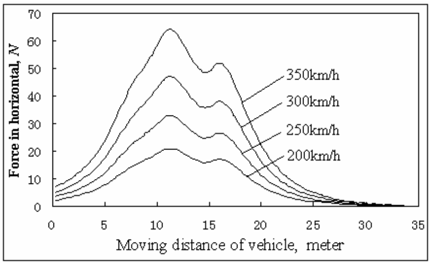

Fig. 7 Aerodynamic force acting on human body as train model 1 tail passes

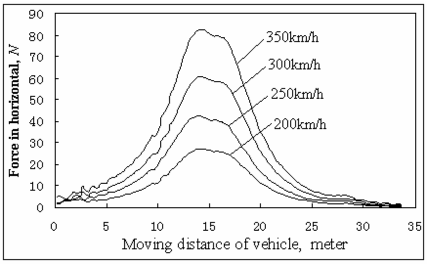

Fig.8 Aerodynamic force acting on human body as train model 2 tail passes

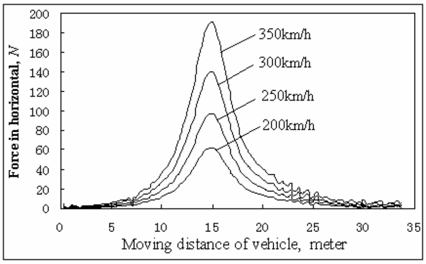

Fig.9 Aerodynamic force acting on human body as train model 3 tail passes

The maximum aerodynamic force acting on human body in all cases for the three models are listed in table 1. Keeping the train running speed and human-train distance constant, a ratio of the maximum aerodynamic force F_T produced by train-head wind and that F_W produced by train-tail wind are also listed in Table 1. The ratios of maximum forces produced by train head and by train tail in different human-train distances for each train model are listed in Table 2. Where $F_{T1.0m}$

means the maximum aerodynamic force produced by train-head wind at *1.0m* human-train distance. $F_{W1.0m}$ means that the maximum aerodynamic force produced by train-tail wind at the same distance. The others have similar meaning.

Table 1 The maximum aerodynamic force produced by train head/tail and their ratio

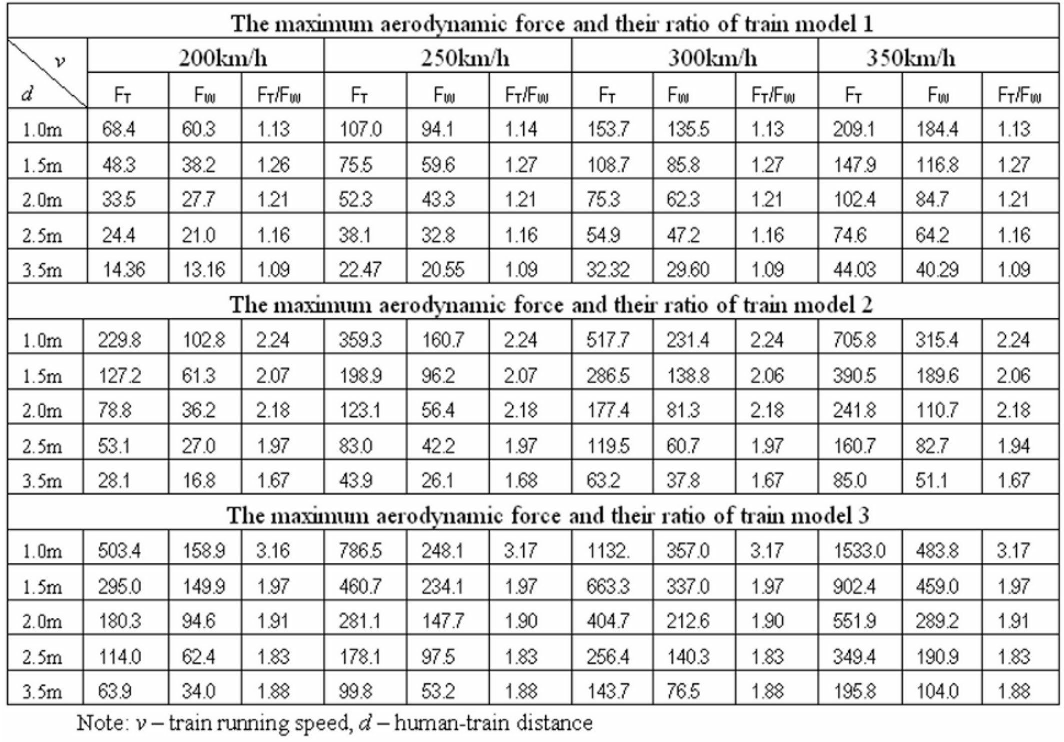

The maximum aerodynamic force and their ratio of train model 1												
v / d	200km/h			250km/h			300km/h			350km/h		
	F_T	F_W	F_T/F_W	F_T	F_W	F_T/F_W	F_T	F_W	F_T/F_W	F_T	F_W	F_T/F_W
1.0m	68.4	60.3	1.13	107.0	94.1	1.14	153.7	135.5	1.13	209.1	184.4	1.13
1.5m	48.3	38.2	1.26	75.5	59.6	1.27	108.7	85.8	1.27	147.9	116.8	1.27
2.0m	33.5	27.7	1.21	52.3	43.3	1.21	75.3	62.3	1.21	102.4	84.7	1.21
2.5m	24.4	21.0	1.16	38.1	32.8	1.16	54.9	47.2	1.16	74.6	64.2	1.16
3.5m	14.36	13.16	1.09	22.47	20.55	1.09	32.32	29.60	1.09	44.03	40.29	1.09
The maximum aerodynamic force and their ratio of train model 2												
1.0m	229.8	102.8	2.24	359.3	160.7	2.24	517.7	231.4	2.24	705.8	315.4	2.24
1.5m	127.2	61.3	2.07	198.9	96.2	2.07	286.5	138.8	2.06	390.5	189.6	2.06
2.0m	78.8	36.2	2.18	123.1	56.4	2.18	177.4	81.3	2.18	241.8	110.7	2.18
2.5m	53.1	27.0	1.97	83.0	42.2	1.97	119.5	60.7	1.97	160.7	82.7	1.94
3.5m	28.1	16.8	1.67	43.9	26.1	1.68	63.2	37.8	1.67	85.0	51.1	1.67
The maximum aerodynamic force and their ratio of train model 3												
1.0m	503.4	158.9	3.16	786.5	248.1	3.17	1132.	357.0	3.17	1533.0	483.8	3.17
1.5m	295.0	149.9	1.97	460.7	234.1	1.97	663.3	337.0	1.97	902.4	459.0	1.97
2.0m	180.3	94.6	1.91	281.1	147.7	1.90	404.7	212.6	1.90	551.9	289.2	1.91
2.5m	114.0	62.4	1.83	178.1	97.5	1.83	256.4	140.3	1.83	349.4	190.9	1.83
3.5m	63.9	34.0	1.88	99.8	53.2	1.88	143.7	76.5	1.88	195.8	104.0	1.88

Note: v – train running speed, d – human-train distance

Table 2 Ratio of the maximum forces in different human-train distances for three models

v / ratio	Model 1, train head				Model 2, train head				Model 3, train head			
	200 km/h	250 km/h	300 km/h	350 km/h	200 km/h	250 km/h	300 km/h	350 km/h	200 km/h	250 km/h	300 km/h	350 km/h
$F_{T1.0m}/F_{T1.5m}$	1.42	1.42	1.41	1.41	1.81	1.80	1.81	1.81	1.71	1.71	1.71	1.70
$F_{T1.5m}/F_{T2.0m}$	1.44	1.44	1.44	1.44	1.61	1.62	1.62	1.62	1.64	1.64	1.64	1.64
$F_{T2.0m}/F_{T2.5m}$	1.37	1.37	1.37	1.37	1.48	1.48	1.48	1.48	1.58	1.58	1.58	1.58
$F_{T2.5m}/F_{T3.5m}$	1.70	1.70	1.70	1.69	1.89	1.89	1.89	1.89	1.78	1.78	1.78	1.78
	Model 1, train tail				Model 2, train tail				Model 3, train tail			
$F_{W1.0m}/F_{W1.5m}$	1.58	1.58	1.58	1.58	1.68	1.67	1.67	1.66	1.06	1.06	1.06	1.05
$F_{W1.5m}/F_{W2.0m}$	1.38	1.38	1.38	1.38	1.70	1.70	1.71	1.71	1.58	1.58	1.59	1.59
$F_{W2.0m}/F_{W2.5m}$	1.32	1.32	1.32	1.32	1.34	1.34	1.34	1.34	1.52	1.51	1.52	1.51
$F_{W2.5m}/F_{W3.5m}$	1.60	1.60	1.59	1.59	1.61	1.62	1.61	1.62	1.84	1.83	1.83	1.84

By analyzing Table 1 and 2, we find an interesting phenomenon. The ratio of aerodynamic forces acting on a human body produced by train head wind over that produced by train tail wind at a given human-train distance for each train model is independent of train running speed. This phenomenon means that it is possible to infer a relationship for the force acting on a human body as a function of train running speed, distance from the train, and train head/tail shape.

3.2.2 Analysis of the direction of the aerodynamic force acting on human body

The change of the force direction in the horizontal plane acting on a human body for the different train models is almost the same. The change of the force direction produced by train head wind and by train tail wind in one calculation case for each train model is shown in figure 10 (a) and (b) respectively. From the figures we find that the force direction angles produced by train head wind and that by train tail wind for different train models changed over 300 degree. The force direction angle is the angle from the train running direction anticlockwise rotation to the aero-force direction.

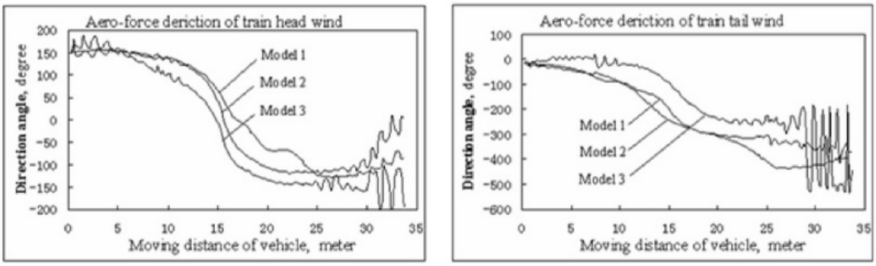

Fig. 10 Aerodynamic force direction change as various shape train head or train tail passes

3.3 Analysis of train wind velocity around human body near high-speed train

The maximum train wind velocity around human body in different calculation cases for train models 1, 2 and 3 are shown in Figs. 11-13 respectively. The wind velocity at human-train distance 0m is assumed to be equal to the train running speed. After summarizing all simulation results in 20 calculation cases for each train model, we find that the maximum wind velocity around human body is about a quadratic function of human–train distance when train running speed is held constant and the maximum wind velocity is about a linear function of train running speed when human-train distance is kept constant. According to these conclusions, we infer a relationship formula for the maximum wind velocity u around human body with train speed v and human-train distance d for each train model.

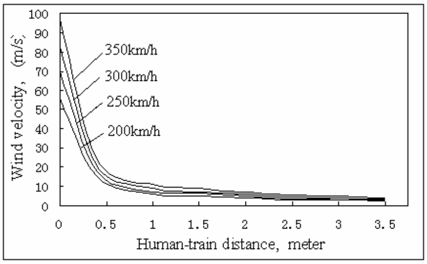

Fig. 11 Change of train wind velocity for model 1

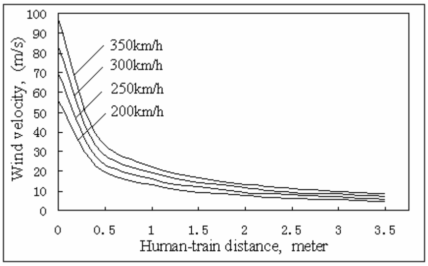

Fig.12 Change of train wind velocity for model 2

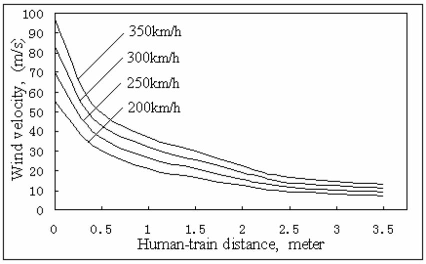

Fig. 13 Change of train wind velocity for model 3

Which are

$$u_{m1} = (1.2319)^{0.072v-4} \times (0.4575d^2 - 3.5496d + 9.1545) \tag{5}$$

$$u_{m2} = (1.1912)^{0.072v-4} \times (1.2549d^2 - 8.8644d + 20.7939) \tag{6}$$

$$u_{m3} = (1.2454)^{0.072v-4} \times (2.1907d^2 - 15.4286d + 34.2111) \tag{7}$$

where u_{mi} —— the maximum wind velocity around human body near model *i* (*m/s)*;

d —— human-train distance （*m*）；

v —— train running speed （*m/s*）；

$m1, m2, m3$ —— means model 1, model 2 and model 3 respectively.

Application range of the formulae (5) - (7) are $55.56 < v < 97.22 m/s$ and $1.0 < d < 3.5m$ .The dimension of *m/s* used here for train running speed *v*. For reference, *55.56m/s* is equivalent to *200km/h* and *97.22m/s* is equivalent to *350km/h*. If the calculated train wind velocities are assumed to be correct values, the curve-fitting errors from formulae (5), (6) and (7) are less than 5%. For relationships between the train wind velocity and train head/tail shape, we were unable to infer accurate formulae from the current computational results.

4 Relationship among train wind force, train speed, human-train distance and train head/tail shapes

The aerodynamic force acting on human body produced by train wind is related to many factors, such as train running speed, human-train distance, train head/tail shapes, smoothness of train surface, relative height between human and train, temperature and moisture of ambient air and so on. But the main factors are three: train running speed, human-train distance and train head/tail shape. Of these three main factors, the train head/tail shape is the most complicated to describe. There are many geometric parameters to describe train head/tail shape even if height and width of the train are kept constant. In order to simplify the analysis, we use only one geometric parameter, length of changeable section at train head/tail *S*, to describe the shape variation of train head/tail here. Thereupon, the aerodynamic force *F* acting on human body produced by train wind is a function of human-train distance *d*, train running speed *v* and the length of changeable section at the train head/tail, *S*. Based on the summary of the simulation results on maximum aerodynamic force in 60 calculation cases, include 3 train models, 4 train running speeds and 5 human-train distances, we infer the following relationship:

$$F_d = \alpha^{0.072v-4} \times (A \times S^2 - B \times S + C)$$

$$55.56 \le v \le 97.22 m/s\text{，}\quad 0 \le S \le 8m \tag{8}$$

where F —— human body aero-force produced by train wind in horizontal (N);

d —— human-train distance（m）;

v —— train running speed（m/s）;

S —— length of changeable section at train head/tail（m）;

α, A, B, C —— coefficients。

The human-train distance *d* as a subscript in formula (8) means that we use separate formula to describe the aerodynamic force for different human-train distance. The purpose is to guarantee precision of the formulae. The formulae for the aerodynamic force at each human-train distance as a function of train running speed and length of changeable section at train head/tail are:

$$F_{1.0} = (1.369)^{0.072v-4} \times (4.559S^2 - 95.7655S + 567.82) \tag{9}$$

$$F_{1.5} = (1.451)^{0.072v-4} \times (3.071S^2 - 56.526S + 305.735) \tag{10}$$

$$F_{2.0} = (1.452)^{0.072v-4} \times (1.927S^2 - 34.403S + 186.53) \tag{11}$$

$$F_{2.5} = (1.462)^{0.072v-4} \times (1.112S^2 - 20.389S + 116.896) \tag{12}$$

$$F_{3.5} = (1.487)^{0.072v-4} \times (0.775S^2 - 12.392S + 63.901) \tag{13}$$

If the computed aerodynamic forces are assumed to be correct values, formulae (9)-(13) have errors less than 5%. Formula (9) is accurate to 5% except for some points where the errors are as large as 10%. If allow the errors of the inferred formulae to be somewhat larger, it is possible to integrate formulae (9) ~ (13) to a single formula for calculating the human aerodynamic force. That is:

$$F = (1.656)^{2(3.5-d)} \times (1.4442)^{0.072v-4} \times (0.6863S^2 - 12.5392S + 69.064) \tag{14}$$

If the human aerodynamic force is calculated by formula (14), except for calculation error large than 20% in a few case points of train model 1, the calculation errors from formula (14) are less than 15%.

5 Conclusions and Suggestions

5.1 Conclusions

Based on Reynolds average Navier-Stokes equations of viscous incompressible fluid, and on $k \sim \varepsilon$ two equations turbulent model, the aerodynamic effects of train wind on human body near high-speed railway were investigated by finite volume method with moving mesh technology. From the numerical results of 60 calculation cases, the following findings can be gained:

(1) There is a big difference in the aerodynamic force acting on human body produced by different shapes of train head/tail. In running speed at *350km/h* and human-train distance of *1m*, the aerodynamic force produce by extremely blunt train head is 7 times more than that produced by a highly streamlined train head. The difference in the force decreases with the increase of human-train distance. The decrease pattern of the force difference is about a quadratic function with the distance and is independent of train running speed.

(2) For a single type of train head at a fixed human-train distance, the ratio of the maximum aerodynamic force produced by the train head over that produced by the train tail is nearly a constant and has nothing to do with train running speed. The ratio of the maximum aerodynamic forces produced by train head from different human-train distance is about a constant regardless of train running speed. The same situation appears around train tail.

(3) According to the conclusions mentioned above, formulae for calculating the aerodynamic force acting on human body produced by train wind may be inferred from the numerical results, listed in formulae (9) - (13). If the calculation precision of the formulae is reduced, it is possible to integrate formulae (9) - (13) into a unified formula for calculating the human aerodynamic force, which is given in formula (14).

(4) The change of the force direction acting on a human body in the horizontal plane in different calculation cases for each train model is almost the same. The change tendency of the force direction for different train models appears a similar type. The force direction angles produced by train head wind and that by train tail wind for different train models changed over 300 degree.

(5) In the numerical calculation range, the maximum wind velocity around human body is about a quadratic function of human–train distance for a given train running speed. The maximum wind velocity is about a linear function of train running speed when human-train distance is kept constant.

(6) According to conclusion (5), the maximum wind velocity u around human body as a function of train speed v and human-train distance d for each train model can be inferred, and are presented in formulae (5) - (7).

5.2 Suggestion of human safety distance

There are many shapes of heads/tails for high-speed trains in the world. The length of changeable section of these high-speed train head/tail is different each other. For example, the length for *E* system high-speed train head in Japan is more than *6m*, the head length of *TGV* in France is *5~7m*, *ICE* in Germany is *3~5m*, while for Chinese high speed trains it ranges from 2.7~*5.3m*. According to formulae (9) - (13), we can approximate the aerodynamic force acting on human body in the different train running speed based on the different head length. If the maximum aerodynamic force that a human can bear could be decided, the human safety distance could be obtained from these formulae. Based on *100N* aerodynamic force as human body bearing force, the safety distances for different train head lengths and different train running speeds are listed in Table 3.

Table 3 Suggestion of human safety distance based on *100N* criterion (*m*)

S(m) *v(km/h)*	1	2	3	4	5	6	7	8
200	2.48	2.28	2.10	1.79	1.50	1.32	1.01	0.7*
250	3.16	2.82	2.46	2.21	1.92	1.54	1.39	1.09
300	3.7*	3.42	3.11	2.62	2.39	2.14	1.82	1.58
350	4.1*	3.9*	3.6*	3.35	3.03	2.66	2.34	2.11

Note: The data with * is estimate value from of the formula by extrapolation

The maximum wind velocity around a human body near a high-speed train for different train running speeds and human-train distances can also be obtained from formulae (5) - (7). Based on these formulae, it is possible to get the wind velocity around human body for different train head lengths. If the maximum wind velocity that a human can stand could be decided, the human safety distance can be obtained from the formulae. Based on *11m/s* velocity as human body limit, the safety distances for different train head lengths at different train running speeds are listed in Table 4.

Table 4 Suggestion of human safety distance based on *11m/s* criterion (*m*)

S(m) *v(km/h)*	1	2	3	4	5	6	7	8
200	1.99	1.79	1.69	1.37	1.16	0.96*	0.75*	0.55*
250	2.46	2.24	1.97	1.72	1.46	1.21	0.96*	0.70*
300	3.12	2.76	2.41	2.07	1.75	1.45	1.15	0.85*
350	3.54*	3.17	2.81	2.46	2.11	1.77	1.42	1.07

Note: The data with * is estimate value from of the formula by extrapolation

From Tables 3 and 4 we can find that the safety distances calculated based on *11m/s* as criterion (United Kingdom) is less than that based on *100N* as criterion (Germany, France). If 9m/s is used as a criterion (Japan), we can get the fairly similar results.

Acknowledgments

Funding from doctoral education base (No. 20040613010) and from innovation engineering for university (No.705044) of Chinese Education Ministry is gratefully acknowledged. The thanks also give to funding of outstanding young scientist (No. 50525518) of China from NSFC.

References

1. Gawthorpe R G, Aerodynamics of trains in the open air [J] Railway Engineering International, 1978, 3: 7~12
2. Brockie N J W, Baker C J, Aerodynamic drag of high-speed trains [J] Journal of Wind Engineering and Industry Aerodynamics 1990, 34: 273-290.
3. Robert A M, Samuel H, Harvey S L, Measurement of aerodynamic pressures produced by passing trains [C] Proceedings of the 2002 ASME/IEEE joint rail conference, Washington DC, 2002, Apr.: 57~64
4. Samuel H, Martin S, High-speed passenger and intercity trains aerodynamic computer model [C] Proceedings of the 2000 international mechanical engineering congress & exposition, Orlando, Florida, 2000, Nov. 83~91
5. Joseph A S, Aerodynamics of high-speed trains [J] Annual review of fluid mechanics, 2001, 33: 371~414
6. Ben D, Mats B, Siniša K, Large eddy simulation of a typical European high-speed train inside tunnels [C] 2004 SAE world congress, SAE Paper 2004-01-0229, Detroit USA
7. Federal Railroad Administration of USA, Aerodynamic effects of high-speed trains [R] RR03-07, 2003, 7: 1~6
8. Federal Railroad Administration of USA, Aerodynamic effects of high-speed trains on people and property at stations in the Northeast Corridor [R] ORD-99/12, 1999, 12: 65~68
9. Federal Railroad Administration of USA, Assessment potential aerodynamic effects on personnel and equipment in proximity to high-speed train operations [R] DOT/FRA/ORD-99/11, 1999, 12: 25~32
10. Tezduyar T E, Finite Element Methods for Flow Problems with Moving Boundaries and Interfaces [J] Archives of Computational Methods in Engineering, 2001, 8: 83-13

11. Horie Toku, Hotoai Sokunan, Train Wind Surveying on Gongqi Test Railway Under the Nature Wind Condition, [R] Report of railway research, No. 1281, Tokyo, Railway society of Japan, 1983，10：29-33.
12. Houxiong Wang, Dezhao He, Heshou Xu, Aerodynamic characteristics of human body acted by train wind [C] Proceeding of the forth conferences on wind engineering and industrial aerodynamics of China, 1994，11：375~380
13. Montagne M S, Mesure du souffle provoque par le passage de la rame TGV 001 a grande vitesse, [C] Informations Techniques – SNCF-Equipment, Paris (1973), Nr, 12：60~62
14. Bo Lei, A study of high-speed train induced air flow and train passing pressure pulses in the open air [D] PhD dissertation of Southwest Jiaotong University, 1995：69~77 (in Chinese)
15. Neppert H, Sanderson R, Vorbeifahrt und ein- und beidseitigen säulernreihen und mauern sowie tunneleinfahrten [R] MBB-UH-22-73, 1973
16. Yasushi U, Motohiko Y, Aerodynamic force on circular cylinders of finite height [J] Journal of Wind Engineering and Industry Aerodynamic, 1994,51: 249~265
17. Autruffe M, Marty P, Aerodynamische untersuchungen an den schnelltriebzug TGV 001 der tranzösischen staatsbahn, [C] Z Leichtbau Verkehrsfahrz, 1975 Nr. 4: 70~73
18. Versteeg H K, Malalasekera W, An introduction to computational fluid dynamics [M] England, Longman Group Ltd 1995
19. Wenquan Tao，Numerical heat transfer [M] Xi’an Publish house of Xi’an Jiaotong University, 2001 (in Chinese)

Application of CFD to Rail Car and Locomotive Aerodynamics

James C. Paul[1], Richard W. Johnson[1], and Robert G. Yates[2]

[1] Airflow Sciences Corporation, 12190 Hubbard Street, Livonia, MI 48150, USA,
jpaul@airflowsciences.com

[2] The Greenbrier Companies, 149 Saddle Oaks Court, Walnut Creek, CA 94596, USA,
bob.yates@gbrx.com

Abstract CFD methods have been employed to solve a number of efficiency, safety and operational problems related to the aerodynamics of rail cars and locomotives. This paper reviews three case studies: 1) numerical models were employed to quantify the drag characteristics of two external railcar features; namely, well car side-posts and inter-platform gaps. The effects of various design modifications on train resistance and fuel usage were evaluated. 2) An operational safety issue facing railroad operators is wind-induced tip-over. A study was completed using CFD and wind tunnel tests to develop a database of tip-over tendencies for a variety of car types within the Norfolk Southern fleet. The use of this database in the development of a speed restricting system for the Sandusky Bay Bridge is also discussed. 3) Another safety issue involves the behavior of diesel exhaust plumes in the vicinity of locomotive cabs. Numerical simulations were performed for a variety of locomotives operating under a number of ambient conditions (wind speed, wind direction). The concentration of diesel exhaust at the operator cab window was quantified. Where appropriate, the studies provide information on the correlation of the CFD results with previously collected wind tunnel and field data.

Introduction

Railcar aerodynamic studies are typically undertaken to improve safety and increase fuel efficiency. A number of approaches are available to assist the engineer in developing improved designs, including numerical simulation, laboratory (wind tunnel) methods, and field tests.

Significant advances have been made in the development of 3-D CFD codes, including Reynolds-Averaged Navier-Stokes (RANS), Unsteady Reynolds-Averaged Navier-Stokes (URANS), Large Eddy Simulation (LES), Detached

Eddy Simulation (DES), Direct Numerical Simulation (DNS), spectral methods, vortex methods, and Lattice-Boltzmann methods [1, 2]. All of these have been applied to the evaluation of heavy vehicle aerodynamics [3, 4]. For the three studies presented below, appropriate tools were sought to provide practical engineering solutions within commercial timeframes and budgets. Because of the many configurations to be modeled, computationally-intensive methods such as LES, DES, and DNS could not be accommodated. Two 3-D RANS finite-volume simulation codes were selected: 1) a proprietary code, VISCOUS [5, 6], and 2) a commercial code, FLUENT [7]. The Reynolds stress tensor was addressed using the κ-ε equations [8, 9]. Although this method does not model detailed turbulent structures, it does predict average surface pressures and force differences with sufficient accuracy for rail car design and tipping moment determination [10]. The CFD simulations were supplemented with both wind tunnel and field tests.

Section I: Aerodynamic Drag Reduction

Studies aimed at reducing the tractive resistance of railroad trains have been performed since the advent of iron rails during the late 18th century [11]. Aerodynamic drag is a major contributor to locomotive power requirements, along with climbing resistance (gravity), frictional resistance (rolling, track, flange, bearing, suspension losses), and the force required for acceleration or deceleration. Measurements made using instrumented cars and coast-down methods indicate aerodynamic resistance can account for over 90% of the tractive effort at higher train speeds [12 through 19].

Review of Past Work

The earliest study of train aerodynamics reported in the literature involved small-scale wind tunnel tests performed during 1898 at Purdue University [20]. A significant amount of research on this topic was conducted during the 1920s and 1930s and is reviewed by Hoerner [21] and Tietjens [22]. Results of research on train resistance components are included in papers by Davis [23], Hay [24], Engdahl [25], and Paul [26]. Following the 1973-1974 OPEC oil embargo [27], many U.S. railroads and railroad equipment manufacturers initiated research programs to evaluate methods of reducing tractive resistance of freight trains [28 through 39]. A significant series of studies was supported by the Association of American Railroads during the 1980s [25, 40, 41, 42]. Airflow Sciences Corporation served as primary contractor for this program and has continued to conduct engineering analysis and design studies for a variety of railroads and rail car manufacturers [43 through 48]. Recent increases in fuel prices have once again generated interest in reducing train resistance.

Approach

During the current study, the aerodynamic performance of two types of well-type intermodal cars, each capable of transporting containers of varying lengths, were evaluated. Various design modifications aimed at reducing aerodynamic drag were modeled using RANS methods. Photos of the two well cars are shown in Figs. 1 and 2.

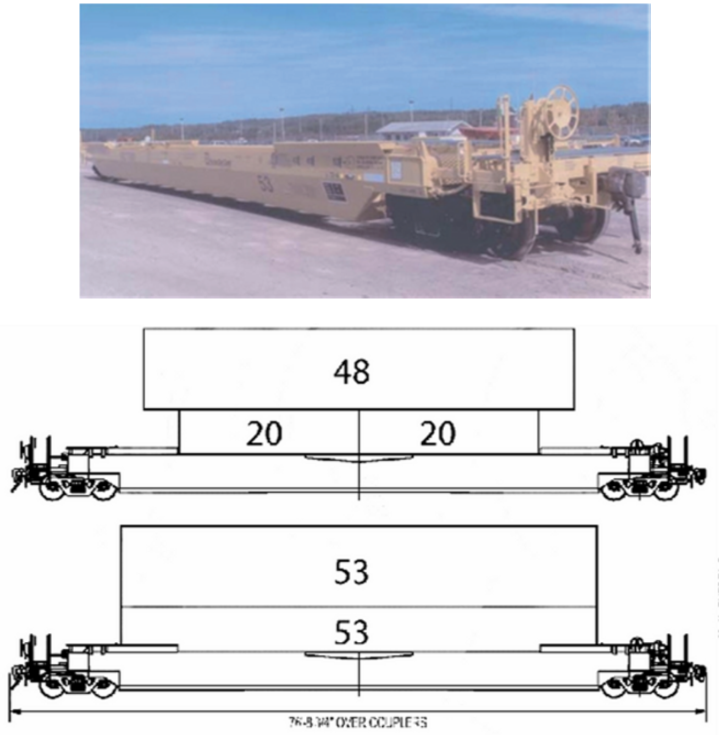

Fig. 1 Husky Stack Well-Type Intermodal Car. Schematic showing loading configuration with containers having lengths of 20’, 48’, and 53’

Two design features were modified to determine their effect on aerodynamic drag: 1) smooth sides versus exposed side posts, and 2) spacing between containers on adjacent cars. CFD models were coupled with an updated version of the AAR AERO program [42] to determine the drag area (see Equation 1) for various container loads and car position-in-train. A fuel consumption calculation was performed to determine the influence of reduced drag on locomotive fuel consumption.

$$S_d = DragArea = C_d A \tag{1}$$

where C_d = drag coefficient of rail car at zero degrees yaw
and A = reference area (projected frontal area of rail car)

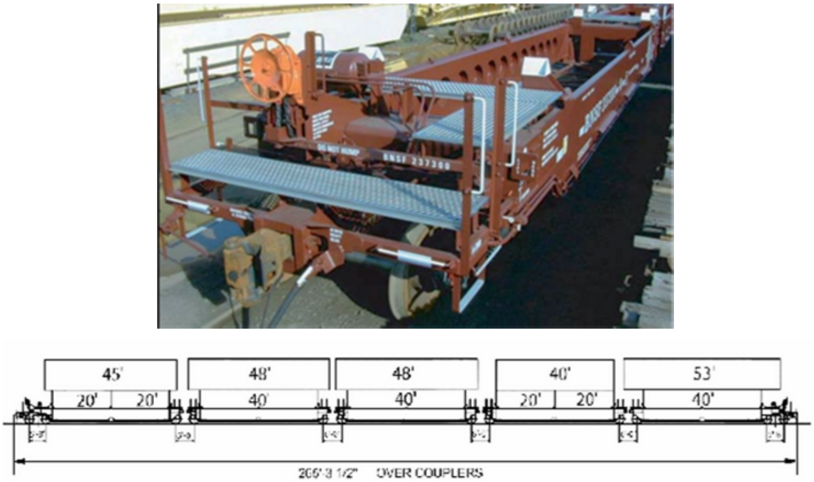

Fig. 2 Maxi-Stack Well-Type Intermodal Car. Schematic showing loading configuration with variety of container lengths.

Fuel consumption calculations are based on the equations developed by Paul, *et. al.* [26, pp. 8-9] [40, p.43]. Assuming the train is operating on straight, level track at constant speed, fuel consumption can be determined from a modified version of the Davis Equation [49]:

$$\begin{bmatrix}\text{Gallons of Fuel}\\ \text{Consumed per}\\ \text{1,000 miles}\end{bmatrix} = K\,(0.0015\,W + 0.00256\,S_d\,V^2 + C\,W) \tag{2}$$

where: K = Fuel consumed per distance traveled per unit of tractive resistance
= 0.2038 gallons/1,000 miles/lbf
S_d = Consist Drag Area (ft^2)
V = Train Speed (miles/hour)
W = Consist Weight (lbf)
C = Hill Factor = 0.0 for level routes and 0.0007 for hilly routes

The first two terms on the right side of Equation 2 represent resistance due to rolling friction and aerodynamic drag, respectively. The last term accounts for the effects of hill climbing. The constant, K, relating fuel consumed per distance traveled per unit of tractive resistance is based on locomotive operational data obtained by members of the Association of American Railroads. Similarly, constant C, the hill factor, is based on operational data for U.S. railroads.

Effects of Modifying Well Car Side Posts

Several researchers have evaluated the effects of modifying external structures on rail cars to reduce aerodynamic drag. Replacing exposed external ribs with smooth sides is particularly effective and offers the advantages of being low cost and easy to install. The table below provides a summary of several rib modification studies that were verified in the wind tunnel and during over-the-track test programs:

Table 1. Effects on Aerodynamic Drag of Rail Cars Due to Modification of Exposed External Ribs (Zero Degrees Yaw, Center Location in Train Consist)

Train Car Type	External Surface Configuration	Modification	Drag Reduction	Reference
Passenger Car	External Ribs and Structure	Smooth Side	6%	[21] pp. 12-10 to 12-11
ISO Container	External Ribs	Smooth Side	10%	[4] pp. 434-435
Hopper Car	External Ribs	Smooth Side	20%	[37] pp. 230-231
Gondola Car	External Ribs	Smooth Side	13%	[37] pp. 230-231
Well Type Intermodal	External Ribs on Trailers	Smooth Side	10%	[36] p. 214
Skeleton Type Intermodal	Platform Support Ribs	Shielded Ribs	15%	[36] p. 78
Gondola Car	External Ribs	Smooth Side	15%	[34] p. 101
Gondola Car	External Ribs	Shielded Ribcaps	17%	[39] p. 186
Open Top Hopper Car	External Ribs	Smooth Side	30%	[41] p. 105

The external ribs comprising the structure of rail cars, containers, and trailers are typically of a size that extends beyond the boundary layer. Flow enters the inter-rib spaces along the vehicle side surfaces and creates a high pressure condition on the upstream side of each rib and a low pressure wake on the downstream side. Experiments have indicated this pressure distribution is essentially the same for each rib, except those located near the ends of the car, container, or trailer.

The original design of the well-type intermodal cars evaluated during the current study included exposed external side ribs along the side of the well as shown in Figs. 1 and 3. The high pressure on the upstream side and low pressure on the downstream side of each rib can be seen in the surface pressure plot of Fig. 3. Details of the flow at a mid-height horizontal plane for one of the exposed ribs are plotted in Fig. 4.

To reduce drag, a smooth, external surface was positioned at the outboard portion of the exposed side posts. This shielded the inter-rib cavities from the external flow as shown by the calculated pressure distribution in Fig. 5. The change in drag area between the exposed ribs and smooth side versions of the well car was calculated based on the surface pressure changes obtained from the numerical model. This $\Delta C_d A$ was referenced to the wind tunnel data using program AERO. The results are summarized in Table 2 for a single car loaded with various length containers. It is noted that drag reductions of 23% are obtained for the five-unit well car due to covering the exposed ribs with a smooth side. This result is similar to those presented in Table 1.

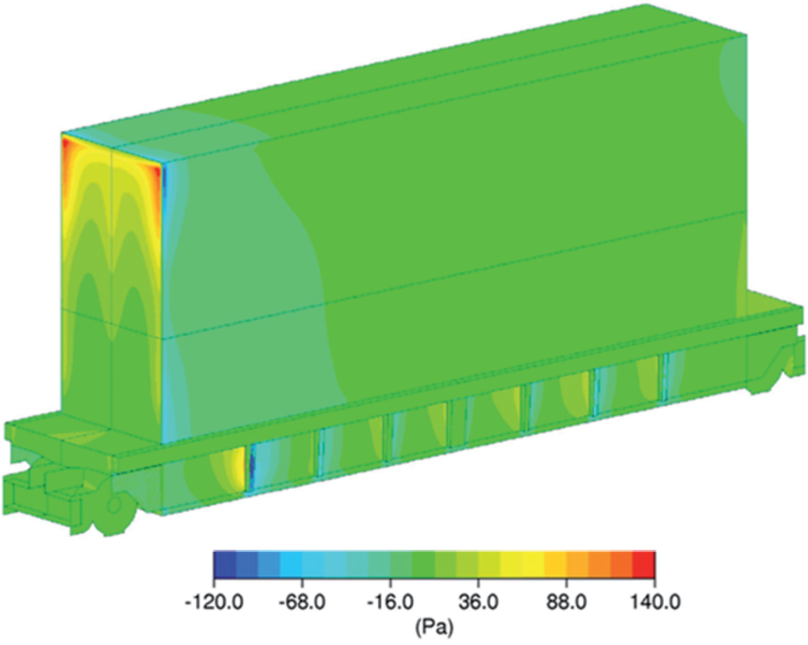

Fig. 3 Calculated Pressure Distribution on Well-Type Intermodal Car with Exposed Ribs (Side Posts), Train Direction is to the Left.

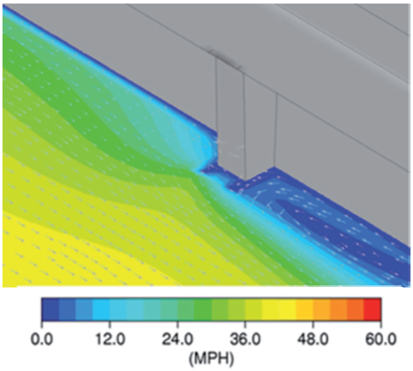

Fig. 4 Detail of Flow Near Well Car External Side Post at Mid-Height Horizontal Plane

Table 2 Drag Area Reduction for 5-Unit Well-Type Intermodal Car

Load Case	Drag Area (ft^2) Smooth Sides	Drag Area (ft^2) Exposed Side Posts
Two 40' long, 9.5' high containers stacked in the well	71.6	93.2
One 40' long, 8.5' high container in the well and one 40' long, 9.5' high container on top	70.6	92.3
Two 20' long, 8.5' high containers in the well and one 40' long, 8.5' high container on top	69.7	91.3

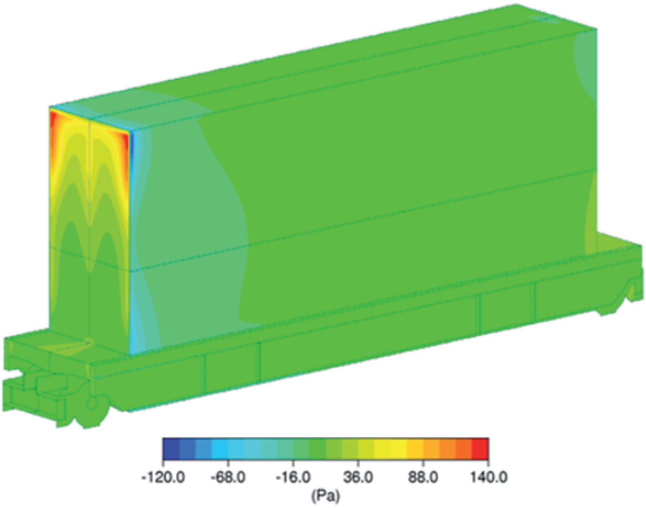

Fig. 5 Calculated Pressure Distribution on Well-Type Intermodal Car with Smooth Sides. Train Direction is to the Left.

Effects of Inter-Car Spacing

Many researchers have evaluated the effects of position-in-train and inter-car spacing on aerodynamic drag [21, 40, 41]. For the case of small gaps between adjacent cars, the flow appears to move smoothly from the rear of the upstream car to the front of the downstream car. The flow in the gap region is a trapped vortex that does not interact substantially with the free-stream. Adjacent cars with narrow inter-car gaps thus act as a single body. As gap distances increase, the drag approaches that of multiple, single bodies [41 p. 99]. This observation has been applied to open top bulk materials cars, such as hopper and gondola cars, where vertical baffles have been employed to provide multiple trapped flow regions, thus preventing high speed air from impacting forward-facing surfaces [41, 50, 51]. For well-type intermodal cars, of course, the gap distance is determined by the container lengths on adjacent cars. The maximum allowable gap is defined by the design of the car ends and couplers. Car manufacturers have proposed placing smaller containers (e.g. 20' ISO containers) on support structures located above the couplers to reduce inter-car gaps. Figure 6 shows the calculated velocity field along the train longitudinal centerline for both a standard well car and a modified well car equipped with spine containers in the region above the couplers. The simulations indicated the drag area of the well car decreased from 44.1 ft^2 to 38.1 ft^2 with the addition of the spine containers. However, the spine containers contributed 6.0 ft^2 of drag area, so no net gain was realized at zero degrees yaw [52].

The results of the various inter-car gap studies (both wind tunnel and CFD model results) were combined to produce the graph shown in Fig. 7. The baseline inter-car gap for the subject well cars is 61.5 inches. The graph provides an indication of the magnitude of the drag changes as the gap distance is increased or decreased from the baseline value. It is interesting to note that the baseline gap places the adjacent containers well into the regime where they are exhibiting the behavior of multiple, sequential bodies. By decreasing the gap from 61.5 inches to 40 inches, the drag can be decreased by 25%.

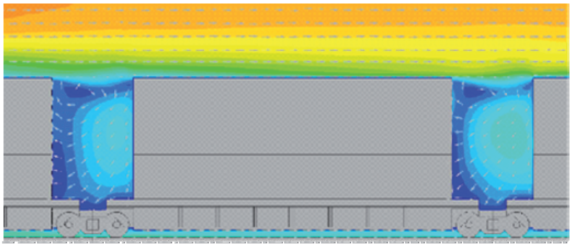

Standard Well Car

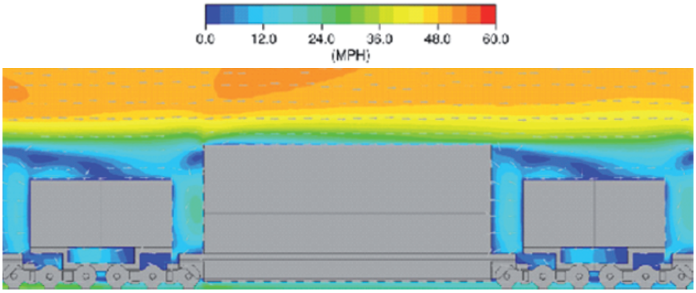

Well Car with Spline Containers

Fig. 6 Comparison of Centerline Flows for Standard and Spline-Type Well Cars

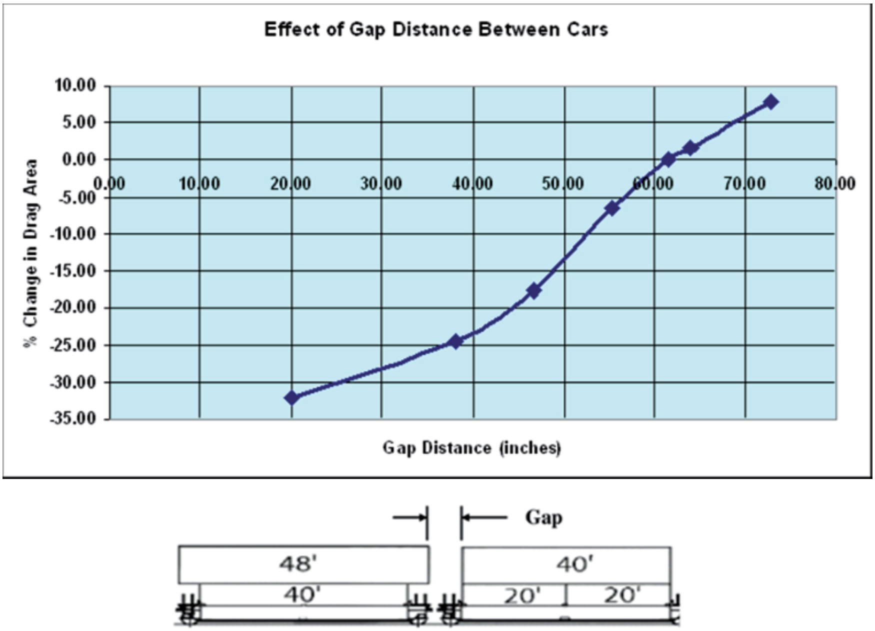

Fig. 7 Effect if Inter-Car Gap in Well Car Drag Area (Baseline Gap Distance is 61.5 Inches)

Results and Conclusions: Section I: Aerodynamic Drag Reduction

The calculated drag reductions resulting from 1) covering the exposed well ribs with smooth sides and 2) reducing the gap distance between adjacent cars were utilized to produce the fuel savings projections shown in Tables 3 and 4. For these comparisons, the following consist was assumed:

5 Locomotives, Twenty 5-Unit Well Cars (= 200 48' Containers)
Total Train Weight: 15,942,000 lbf

Table 3 Fuel Consumption: Gallons per 1,000 Miles: Well Car Intermodal Train with Exposed Ribs and Smooth Sides.

Configuration	Level Route			Hilly Route		
	40 MPH	50 MPH	60 MPH	40 MPH	50 MPH	60 MPH
Exposed Side Posts	6,785	7,860	9,175	9,059	10,135	11,449
Smooth Sides	6,287	7,082	8,053	8,561	9,356	10,328

Table 4 Fuel Consumption: Gallons per 1,000 Miles: Well Car Intermodal Train with Various Inter-Car Gaps.

Gap (inches)	Level Route			Hilly Route		
	40 MPH	50 MPH	60 MPH	40 MPH	50 MPH	60 MPH
61.5	6,785	7,860	9,175	9,059	10,135	11,449
55	6,661	7,666	8,895	8,935	9,940	11,169
47	6,450	7,337	8,421	8,725	9,612	10,696
20	6,173	6,904	7,798	8,447	9,179	10,072

Adding smooth sides to the well car improves fuel economy on level routes by 7.3% for low speeds up to 12% for high speeds. For hilly routes, fuel economy improvements vary from 5% at low speeds to 6% at high speeds. Reducing the inter-car gap also provides significant improvements in fuel economy. For level routes, reducing the inter-car gap from 61.5 inches to 47 inches reduces fuel usage by 5% at low speeds and 8% at high speeds. For hilly routes this reduction in gap distance improves fuel economy by 4% at low speeds and 7% at high speeds.

Section II: Wind Induced Tip-Over

Strong cross winds can lead to tip-over and derailment of train cars exhibiting large profiles and/or light weight, such as passenger coaches and intermodal equipment. The safety of railroad workers and the public is at risk during these events. The photo in Fig. 8 shows a tip-over accident that occurred during 2006 on the Kahnawake Bridge (Montreal, Quebec, Canada). Several other recent wind-related accidents, including those listed below, have led to engineering studies aimed at preventing their occurrence.

- 28 January 1987: Union Pacific Railroad: 4 empty containers blown from two TTX cars near Laramie, Wyoming; crosswind speeds measured to be 45 miles/hour.
- 24 March 1987: Union Pacific Railroad: 25 cars were derailed near Brule, Nebraska due to high winds, measured at 53 miles/hour.
- 11 November 1988: Consolidated Rail Corporation: 64 Road Railer intermodal cars derailed on the Sandusky Bay Causeway (Ohio) during high winds.
- 11 February 2003: Norfolk Southern Railway: train derailment on Sandusky Bay Causeway during high winds.

Cleanup costs can be significant and hence create an additional incentive for seeking an effective train speed restricting system aimed at reducing these events.

Photo Credit: http://www.citynoise.org, February 2006

Fig. 8 Freight Train Derailment: 18 February 2006, Montreal Quebec, Kahnawake Bridge, 67 mile/hour crosswinds.

Three primary goals were established for the current study:

- Develop railcar tipping moment (defined below) data base. This included gathering wind tunnel test data for high-population railcars and performing CFD simulations to gain additional insight into the aerodynamic conditions leading to tip-over events.
- Develop a real-time computer algorithm to signal appropriate train speed reductions during hazardous cross wind conditions.
- Select and locate wind sensors and configure and implement the train speed restricting system.

Review of Past Work

The wind tunnel studies funded by the Association of American Railroads included force measurements of a wide variety of cars and locomotives at yaw angles up to 90°. Much of this work is summarized by Furlong, *et. al.* [41]. These studies provide a large database of car side forces and rolling moments under crosswind conditions.

Matschke, *et. al.* [53] performed a risk assessment of cross winds on high speed trains to define countermeasures for safe railway operation. Andersson, *et. al.* [54] identified locations in Sweden prone to high winds and possible train overturning and performed a risk assessment for safe train operation. Experimental methods for measuring side forces and rolling moments for high-speed trains were developed by Sanquer, *et. al.* [55]. Pressure measurements on double-stack freight cars during train passing conditions were made by MacNeill, *et. al.* [56] and used for comparison with CFD simulations. The simulations were employed to define conditions under which double-stack container cars are subject to tip-over [57]. Hoppmann, *et. al.* [58] developed a wind prediction model as part of a railway safe operations system. Tipping effects on rail cars caused by jets emanating from tunnel pressure relief ducts were investigated by Polihonki, *et. al.* [59]. During 1988, Gielow, *et. al.* [60] conducted a series of wind tunnel tests using 16% scale models to determine the aerodynamic forces acting on a variety of rail cars, including intermodal and automobile transporters. The study culminated in development of a train-speed-restricting system to achieve safe operating conditions under high wind conditions along routes operated by Union Pacific Railroad. Additional evaluations on the tip-over behavior of autorack rail cars was performed by Airflow Sciences Corporation during 1998 [61]. Tipping moments were calculated as a function of train speed and cross wind speed and found to be less than half those of double-stack intermodal cars under the same cross wind conditions, primarily because of the higher pressures on the leeward side of the rounded-top autorack cars.

Approach and Speed Restricting System Description

The Sandusky Bay Causeway is located at the southwestern end of Lake Erie northwest of Sandusky, Ohio (see Fig. 9). Trains moving across the causeway are subject to the high winds that occur frequently in this region. Norfolk Southern Railway funded an engineering effort to develop a train speed restricting system with the goal of eliminating tip-over accidents at this location. The project was divided into several phases and concluded during 2006 with the implementation of wind sensors located on the causeway, data acquisition hardware, and data analysis computers linked by the Norfolk Southern network [62].

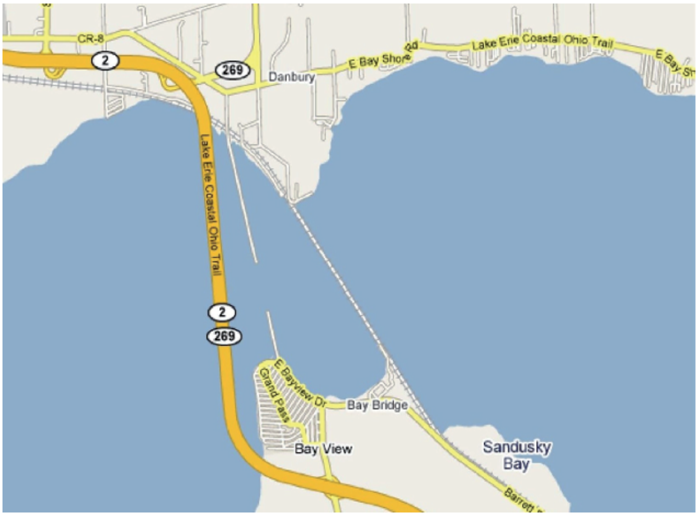

Fig. 9 Map Showing Sandusky Bay Causeway (*Map Credit: Google Maps)*

The main components of the Sandusky Bay Causeway Speed Restricting System are shown in the block diagram of Fig. 10.

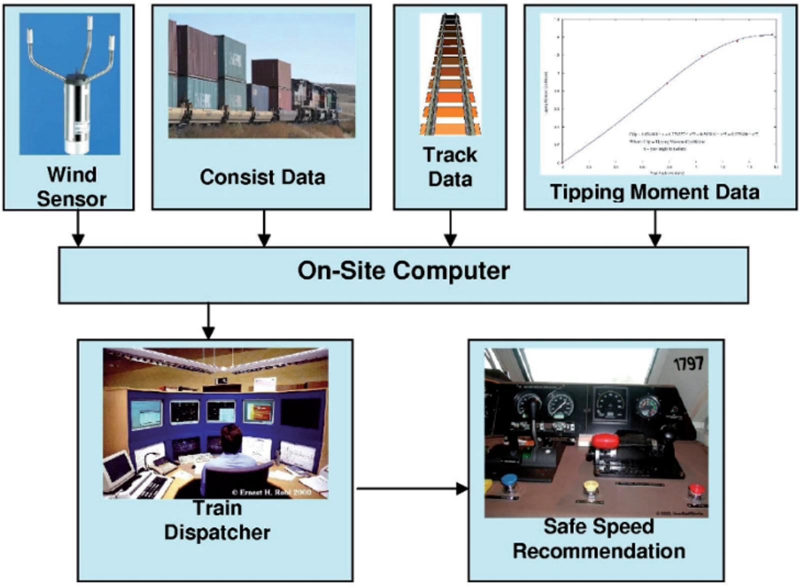

Fig. 10 Sandusky Bay Causeway Train Speed Restricting System Components

Tipping moment data were obtained from wind tunnel tests and CFD simulations. Data for the following car types were obtained from earlier wind tunnel tests [36, 37, 60, 63]. An example of the wind tunnel tipping moment coefficient plots is shown in Fig. 11. CFD models were constructed for each of the cars represented in the wind tunnel tests. Comparisons between forces and moments obtained from the CFD models compared favorably with those obtained during the wind tunnel tests. As noted earlier, the FLUENT RANS models provide good correlation with the average pressures on the leeward side of the vehicle, leading to good agreement with the measured rolling moments. Peters [64, p. 464] showed similarly good agreement between calculated tipping moments (using FLUENT) and wind tunnel data. Additional CFD models were developed to obtain tipping moments for car types not included in the original wind tunnel tests. Car types were selected from lists, provided by Norfolk Southern Railway, of representative freight train consists that traverse the Sandusky Bay Causeway. Rail cars aerodynamic characteristics obtained from the CFD models are listed in Table 5 and those obtained from earlier wind tunnel tests are listed in Table 6. Velocity profiles and pressure distributions for typical CFD models, in this case a 53' well-type intermodal car at 90° yaw, are shown in Figs. 12 and 13, respectively.

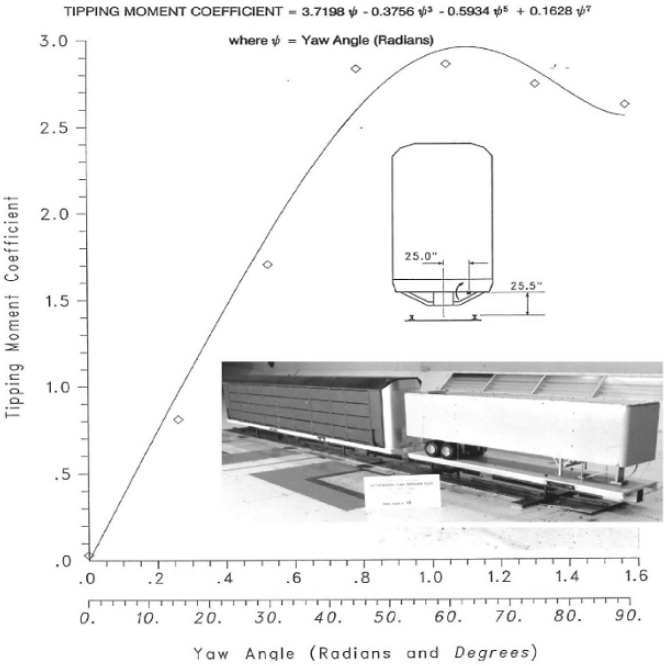

Fig. 11 Example Tipping Moment Plot Obtained from Wind Tunnel Test Data: Autorack Car.

Table 5 Rail Cars Evaluated Using CFD Models (C = Container)

Rail Car	Lading
BS177 Box Car	Empty
BS216 Box Car	Empty
BS89 Box Car	Empty
RoadRailer (53’ Trailer)	Empty
HS46 Hopper Car	Empty
H11D Hopper Car	Empty
G86 Gondola Car	Empty
53’ Well Car	53’ C on 53’ C

Table 6 Rail Cars Evaluated Using Wind Tunnel Models (C = Container, T = Trailer)

Rail Car	Lading
48’ Thrall Well Car	40’ C on 40’ C
48’ Thrall Well Car	53’ C on 48’ C
Gunderson Bulkhead Well Car	40’ C on 40’ C
Gunderson Bulkhead Well Car	40’ C on 40’ C
Gunderson Bulkhead Well Car	48’ C on 40’ C
Gunderson Bulkhead Well Car	48’ C on 40’ C
89’ Flat Car	Two 40’ T
89’ Flat Car	Two 45’ T
89’ Flat Car	One 40’ C
89’ Flat Car	Autorack

For each rail car, simulations were performed at yaw angles of 0°, 45°, 60°, 75°, and 90°, with 0° representing a pure headwind and 90° a pure cross wind condition. Forces and moments were computed for the center cars only for both the wind tunnel and CFD models. The upstream and downstream cars were included to provide an accurate representation of the flow field [50, pp. 151-152].

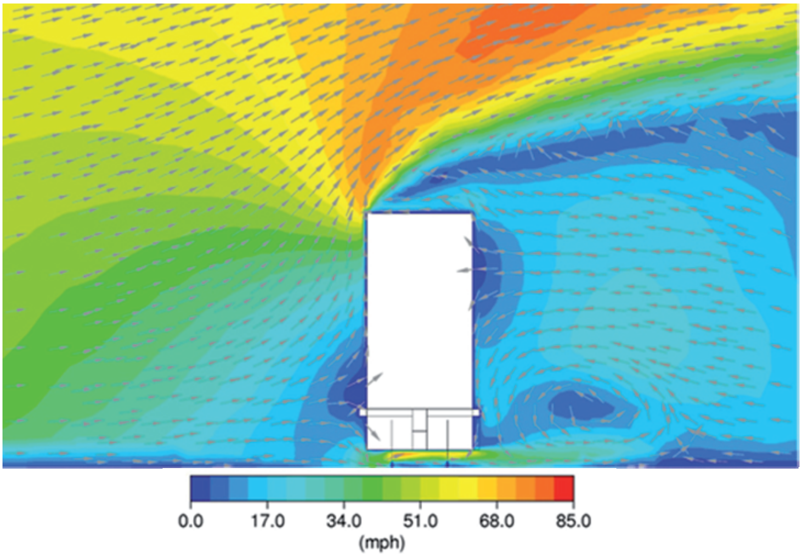

Fig. 12 Velocity Profile for 53’ Well-Type Intermodal Car at 90° Yaw, Flow in Plane Perpendicular to Train Longitudinal Axis at Mid-Car Location.

Once the tipping moment relationships were established, 7th order polynomial curve fits were developed (see Fig. 11) and supplied as input to the train speed restricting algorithms.

A rail car will begin to rotate when the aerodynamic tipping moment exceeds the restoring moment. The restoring moment is taken as the weight of the railcar acting through the tipping arm. The aerodynamic tipping moment is taken as the weight of the rail car acting through the tipping arm, as illustrated in Figure 14. Note that dynamic effects are not included since they have been shown to be small compared to the wind forces and rail car weights.

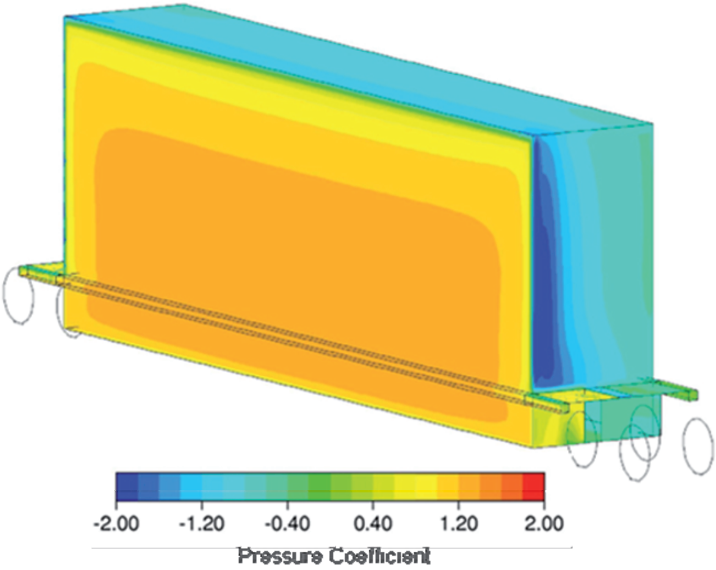

Fig. 13 Pressure Distribution, Windward Side, 53' Well-type Intermodal Car at 90° Yaw

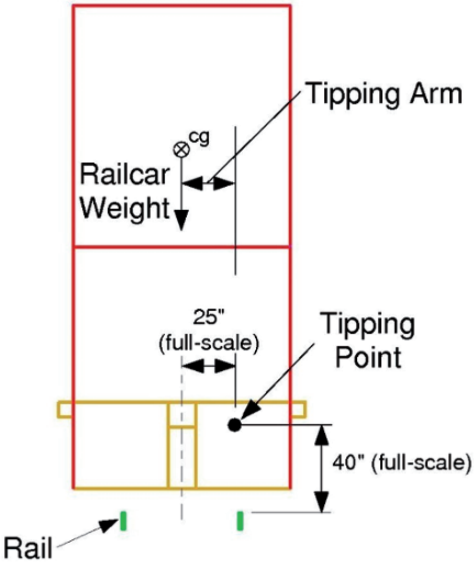

Fig. 14 Relationship Between Aerodynamic Tipping Moment and Restoring Moment

At the onset of tipping:

Restoring Moment = Aerodynamic Tipping Moment

$$W \cdot L = \tfrac{1}{2} \cdot \rho \cdot V^2 \cdot C_{tip} \cdot A_{ref} \cdot L_{ref} \tag{3}$$

where:

W = Light Weight of Railcar (Less Trucks) Plus Empty Containers or Trailers
L = Tipping Arm (Horizontal Distance between Railcar cg and Tipping Point)
ρ = Air Density
V = Wind Velocity Relative to Train
C_{tip} = Tipping Moment Coefficient
A_{ref} = Reference Area = 100 ft^2
L_{ref} = Reference Length = 50 ft

As noted above, C_{tip} is defined as a function of yaw angle (ψ) using a 7th order polynomial curve fit of the form:

$$C_{tip} = a \cdot \psi + b \cdot (\psi)^3 + c \cdot (\psi)^5 + d \cdot (\psi)^7 \tag{4}$$

The parameters a, b, c, d are the polynomial curve fit coefficients. Yaw angle and relative wind speed (V) are both functions of train speed (V_t), wind speed (V_w), and wind angle (θ) relative to the track. The sketch below shows the relationship between these variables.

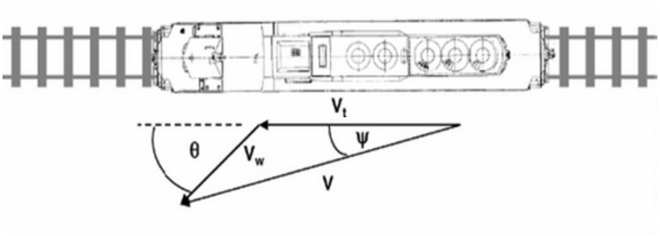

Thus, relative wind speed and yaw angle can be expressed as:

$$V^2 = (V_t + V_w \cdot \cos(\theta))^2 + (V_w \cdot \sin(\theta))^2$$
$$\psi = \tan^{-1}[V_w \cdot \sin(\theta) / (V_t + V_w \cdot \cos(\theta))] \tag{5}$$

Recall that the equation for safe train speed comes from a balance of the aerodynamic tipping moment and the restoring moment:

$$0 = W \cdot L - \tfrac{1}{2} \cdot \rho \cdot V^2 \cdot C_{tip} \cdot A_{ref} \cdot L_{ref} \tag{6}$$

Substituting the expressions for V and C_{tip} into the above equation yields the expression to be solved for safe train speed:

$$0 = W \cdot L - \tfrac{1}{2} \cdot \rho \cdot [(V_t + V_w \cdot \cos(\theta))^2 + (V_w \cdot \sin(\theta))^2] \cdot [a \cdot \psi + b \cdot (\psi)^3 + c \cdot (\psi)^5 + d \cdot (\psi)^7] \cdot A_{ref} \cdot L_{ref} \quad (7)$$

Because ψ is a function of V_t, numerical methods must be used to solve the above equation.

The weight used for each railcar is the light weight (less the truck weight) plus the empty weight of the appropriate container(s) or trailers. Unloaded weights are used in order to obtain the most conservative (lowest) tipping speeds for each railcar. The weight (W), and tipping arm (L), and tipping point for each rail car were included in the train speed restricting system database.

Wind data were obtained using an ultrasound-based anemometer located at the Causeway. The sensor was located 500 feet north of the bridge on the lake side to avoid interference by the bridge structure. The sensor is programmed to provide wind speed and direction at 5 second intervals.

Three separate computer algorithms work together to form the core of the Sandusky Bay speed restricting system. The names of these algorithms are SRS (acronym for Speed Restricting System), Wind, and Safespeed. Each performs a specific task in the computation and display of safe train speeds. Program SRS is installed on the Train Dispatcher's computer. Programs Wind and Safespeed are installed on the computer located at the Causeway. Program Wind acquires data from the anemometer and provides the information to Program Safespeed which, in turn, calculates the tipping speed for each rail car in the consist. These files are transferred to SRS for display on the Dispatcher's console.

Results and Conclusions, Section II: Wind-Induced Tip-Over

Wind tunnel and CFD investigations of a variety of freight cars were used to assemble a tipping moment data base for cross wind conditions. Each of the rail cars included in the data base exhibits a particular type of tip-over behavior as summarized in Table 7. These data served as the basis for development of a real-time speed restricting system for the Sandusky Bay Causeway. The system includes a set of computer algorithms for calculating safe train speeds based on wind data obtained from a site-mounted anemometer.

Table 7a Rail Car Tipping Characteristics, Car Parameters

Railcar	Tipping Point Relative to Centerline Top-of-Rail Position		Railcar Light Weight Including Trucks (lbs)	Unloaded Lading Weight (lbs)
	Horizontal Location (in.)	Vertical Location (in)		
BS177 Box Car	25	30	66,400	0
BS216 Box Car	25	30	77,400	0
BS 89 Box Car	25	30	111,800	0
53 Foot RoadRailer	28.25	0	-	15,800
HS46 Hopper Car	25	30	80,000	0
H11D Hopper Car	25	30	56,300	0
G86 Gondola Car	25	30	59,000	0
53 Foot Well Car	25	40	50,000	20,000
48 Foot Thrall Well Car	25	40	48,900	14,800
48 Foot Thrall Well Car	25	40	48,900	19,000
Gunderson Bulkhead Well Car	25	40	41,000	14,800
Gunderson Bulkhead Well Car	50.3	125.5	-	7,400
Gunderson Bulkhead Well Car	25	40	41,000	16,400
Gunderson Bulkhead Well Car	53.3	125.5	-	9,000
89 Foot Car	25	25.5	68,000	26,000
89 Foot Car	25	25.5	68,000	28,000
89 Foot Car	48	47.5	68,000	7,400
89 Foot Car	25	25.5	97,000	0

Table 7b Rail Car Tipping Characteristics, Manner of Tipping

Railcar	Total Weight of Tipping Railcar and Lading (lbs)	Manner of Tipping
BS177 Box Car	42400	Railcar tips off trucks
BS216 Box Car	53400	Railcar tips off trucks
BS 89 Box Car	87800	Railcar tips off trucks
53 Foot RoadRailer	27400	Combined trailer & trucks tip off rail
HS46 Hopper Car	56000	Railcar tips off trucks
H11D Hopper Car	32300	Railcar tips off trucks
G86 Gondola Car	35000	Railcar tips off trucks
53 Foot Well Car	46000	Combined trailer & trucks tip off rail
48 Foot Thrall Well Car	39700	Combined trailer & trucks tip off rail
48 Foot Thrall Well Car	43900	Combined trailer & trucks tip off rail
Gunderson Bulkhead Well Car	43800	Combined trailer & trucks tip off rail
Gunderson Bulkhead Well Car	7400	Top container tips off bottom container
Gunderson Bulkhead Well Car	45400	Combined trailer & trucks tip off rail
Gunderson Bulkhead Well Car	9000	Top container tips off bottom container
89 Foot Car	70000	Combined trailer & trucks tip off rail
89 Foot Car	72000	Combined trailer & trucks tip off rail
89 Foot Car	51400	Container blows off Railcar
89 Foot Car	73000	Railcar tips off trucks

Section III: Diesel Exhaust Plume Behavior

Many studies have indicated a relation between occupational exposure to diesel exhaust and diseases of the lung [65-68]. The relative risk (RR) for lung cancer, for example, among those classified as having been exposed to diesel exhaust, is approximately 1.2 to 1.5 times the risk in those classified as unexposed. Diesel exhaust emissions contain hundreds of chemical compounds, which are partly in the gaseous phase and partly in the particulate phase. Railroad locomotive operators have issued complaints regarding diesel exhaust entering the cab through open windows [69]. Most diesel particles are small enough (0.02 to 0.5 μm) to be transported deep into the lungs, where they pose the greatest hazard to human health [70, 71]. The goal of the current study is to evaluate the behavior of exhaust plumes issuing from diesel locomotives and quantify the levels of exhaust components at the operator cab window.

Review of Past Work

It is well known that separation zones on the leeward sides of large rectangular objects can entrain exhaust flows. To prevent “sick building” syndrome, for example, the American Society of Heating, Refrigeration, and Air Conditioning Engineers publishes guidelines for exhaust stack heights and intake vent locations for buildings and industrial facilities [72]. During wind tunnel tests completed for General Electric Transportation Systems during 1986 [73], smoke flow visualization methods were employed to assess the behavior of the simulated diesel engine exhaust plume for a locomotive. The study showed the plume was relatively unaffected by passive changes to the locomotive surface (strakes, baffles, vanes). As the photo in Fig. 15 shows, the exhaust is entrained within a strong vortex pattern on the leeward side of the locomotive that envelopes the operator’s cab when the locomotive is operated with the long hood forward. It was shown that an auxiliary blower is effective at moving the plume above the operator’s cab as shown in Fig. 16. Operating the locomotives with the short hood forward significantly reduces the concentration of the plume on the lead locomotive operator’s cab.

Fig. 15 Diesel Exhaust Plume Behavior: 1/15-Scale Wind Tunnel Test, Yaw Angle = 10°, Long Hood Forward, Baseline Exhaust System

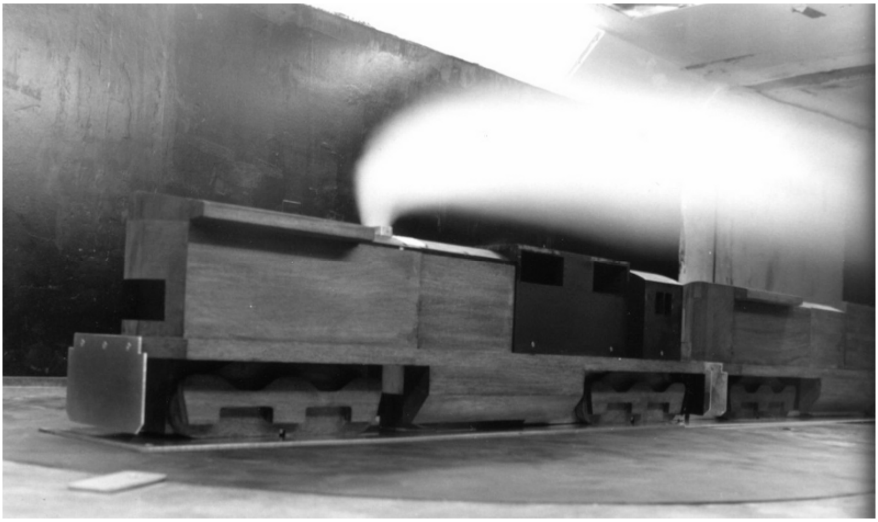

Fig. 16 Diesel Exhaust Plume Behavior, 1/15-Scale Wind Tunnel Test, Yaw Angle = 10°, Long Hood Forward, with Auxiliary Blower in Operation.

Approach

To quantify the concentration of exhaust at the locomotive operator's cab window, a significant research and simulation effort was required. The approach to performing this study is outlined below and shown schematically in Fig. 17.

Specific tasks included a) identification of typical switchyard and line-haul locomotives. Various references were employed, including the latest edition of *The Car and Locomotive Cyclopedia of American Practices*, locomotive manufacturer specifications, inventories of locomotives in various railroad fleets, and interviews with industry experts [74], b) assessment of U.S. track surveys and meteorological data, c) an evaluation of typical crosswind conditions (wind yaw angles) experienced within switchyards and line-haul operations, d) identification of typical locomotive throttle (notch) positions and train speeds for both switchyard and line-haul operations (these were used to calculate typical exhaust flow rates), e) diesel exhaust characteristics (flow rates, composition, and temperature) were obtained for a variety of locomotives, and f) other field test and wind tunnel test data relating to locomotive exhaust plume behavior were reviewed including field tests, wind tunnel tests, and CFD simulations. Concentrations of exhaust gas components and particulate matter at the leeward side windows of locomotives operating in both switchyard and line-haul conditions were identified for a range of operating conditions, based on the concentrations defined by the numerical models and the exhaust composition information obtained from the literature.

Full details of the exhaust concentration studies can be found in Paul and Linfield [75, 76]. A study of weather conditions [77] along a large number of railroad routes indicates that cross wind conditions occur during a majority of the time. Locomotives operating in cross wind conditions exhibit two distinct flow regions: 1) windward side of the vehicle, and 2) leeward side of the vehicle. Air flow patterns on the leeward side are characterized by large vortex formations and strong recirculating conditions. This recirculating, leeward-side wake acts to entrain gases emitted at the diesel engine exhaust stack.

To define effects of cross winds, both the track orientation and ambient wind patterns must be evaluated. During earlier studies [75, 76], specific track orientations were obtained from survey data and combined with historical wind records to determine the relative angle and speed of the air approaching the train. Analyses of train routes, train speeds, and ambient wind conditions indicate yaw angles vary from 5° to 69°. Lower yaw angles apply to higher train speeds and lower wind speeds. Higher yaw angles correspond to lower train speeds and higher wind speeds.

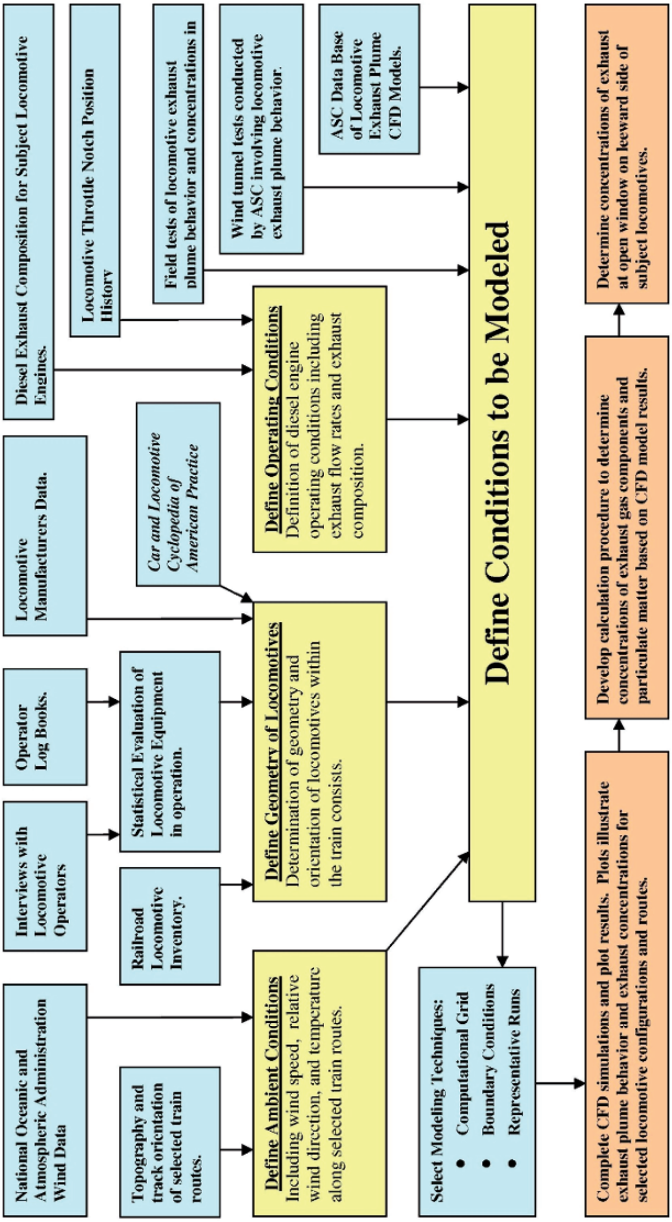

Fig. 17 Determination of Diesel Exhaust Plume Concentrations within Locomotive Cabs, Project Flow Chart.

A review of existing locomotive exhaust test data indicated flow rates are linearly proportional to engine horsepower [78]. Thus, for each throttle setting (also called "notch setting") used in the numerical simulations, the diesel exhaust flow rate can be scaled from available test data for similar 2-cycle engines. Test data available in the literature, such as that reported by Southwest Research Institute [79], were used to calculate exhaust gas temperatures and flow rates for a variety of locomotive models and manufacturers.

Exhaust gas composition was determined based on locomotive diesel engine test data reported in the literature (*Bosch Automotive Handbook* [80], Southwest Research Institute [81]). Exhaust gas components included in the current and previous studies were: 1) oxides of nitrogen (NO_x), 2) carbon monoxide (CO), 3) unburned hydrocarbons, 4) sulfur dioxide (SO_2), and 5) particulate matter. The exhaust composition for typical 2-cycle diesel engines is summarized in Table 8:

Table 8. Exhaust Composition for 2-Cycle Diesel Locomotive Engines

Exhaust Component	Low Value (g/bhp-hr)	High Value (g/bhp-hr)	Low Value (kg/bhp-sec)	High Value (kg/bhp-sec)
NO_x	10.01	16.11	2.78E-06	4.48E-06
CO	0.37	3.68	1.03E-07	1.02E-06
Unburned Hydrocarbons	0.20	0.45	5.56E-08	1.25E-07
SO_2	0.69	1.18	1.92E-07	3.28E-07
Particulate Matter	0.14	0.24	3.89E-08	6.67E-08

g/bhp-hr = grams per brake horsepower hour
kg/bhp-sec = kilograms per brake horsepower second

The mass fraction of diesel exhaust concentrations in the vicinity of a variety of locomotives has been calculated using the VISCOUS finite volume RANS code [5]. This code employs a staggered pressure-based solver over a Cartesian grid. The grid extended four train lengths forward of the locomotive, three train lengths aft of the trailing locomotive, 10 train heights above the locomotives and 5 train widths to each side. Initial models were evaluated using a range of grid sizes from fine to coarse in order to confirm grid independence. Boundary conditions, representing ambient wind conditions, were imposed at the outer edges of the computational domain. Additional boundary conditions relating to locomotive operation (exhaust flows, dynamic brake flows, electronics cooling flows, engine cooling system, etc.) were imposed at the appropriate geometric locations within the grid structure. The local concentrations of exhaust components were determined from the numerical simulation results (exhaust concentrations) and the exhaust components for 2-cycle diesel locomotive engines

In addition to ambient conditions (wind direction, speed, temperature), locomotive geometry, and operating conditions (exhaust flow rates, exhaust temperatures, throttle positions), field tests of locomotive exhaust plume behavior and exhaust component concentration measurements taken within cabs of operating locomotives were included in the analysis [82, 83, 84]. The models and field tests confirmed the characteristic windward/leeward side delineation of the flow field in the vicinity of operating locomotives operating under crosswind conditions. The strong recirculation region on the leeward side of the locomotive acts to entrain the gases emitted from the diesel engine exhaust and moves these gases along the longitudinal axis of the train.

Numerical simulations of diesel exhaust plume behavior were completed for seven locomotive types and 27 configurations (train orientation, wind speed, wind direction, exhaust flow rate). Three examples have been selected and are presented in Figs. 18 through 20. Each of these figures shows the calculated concentrations at various planes along the length of the train. The red colors correspond to regions having exhaust concentrations equal to the concentration at the stack outlet plane. Orange represents regions having exhaust concentrations equal to 1/10th of the concentration at the stack exit. The yellow regions have concentrations equal to 1/100th of the concentration at the stack exit, and so forth. The color scale is logarithmic, so the numbers represent concentration changes that vary by powers of 10.

The exhaust plume enters the wake on the leeward side and travels along this side of the train. Concentrations of exhaust components are higher in those wakes corresponding to higher train speeds and smaller yaw angles, such as those encountered in city-to-city runs (Figs. 19 and 20). Higher yaw angles, which occur at lower train speeds and higher cross wind speeds (Fig. 18), tend to enlarge the wake on the leeward side of the train and reduce the exhaust concentrations compared to those encountered at higher speeds where the wake tends to remain closer to the side of the train.

The numerical simulations indicate exhaust concentrations in the lead locomotive are highest for locomotives operated with the long hood forward. For switchyard operations (low speeds), exhaust concentrations in the lead locomotive increase with increasing yaw angles. For line-haul operations (high speeds), exhaust concentrations in the lead locomotive decrease with increasing yaw angles. Higher concentrations of exhaust occur at the leeward windows of the trailing locomotive for both the switchyard and line-haul operations.

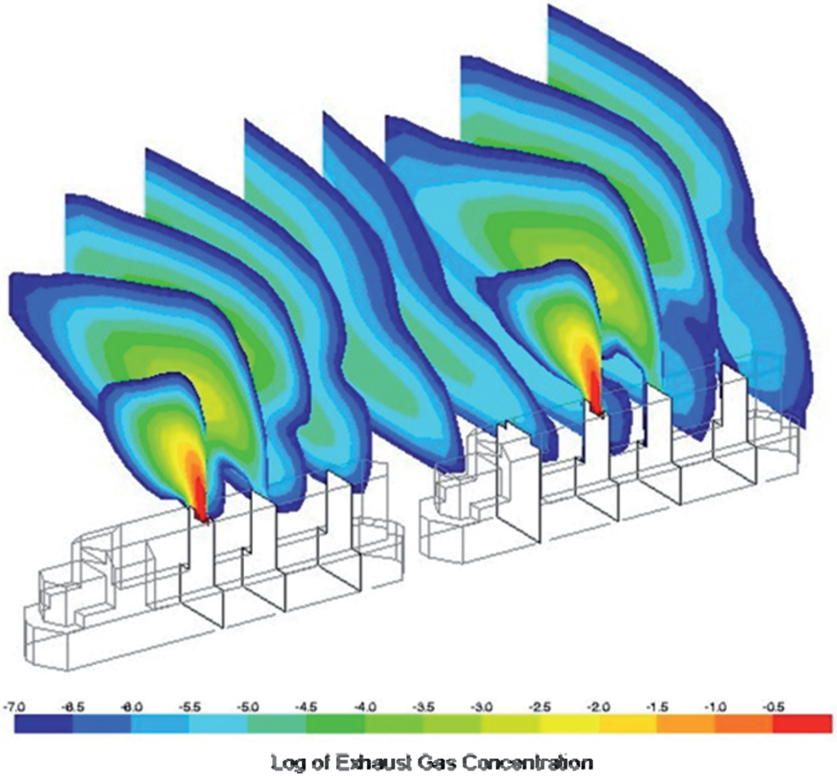

Fig. 18 Two GM EMD GP38 Locomotives, Both Oriented with Short Hood Forward, Throttle Position = Notch 8, Train Speed = 5 miles/hour, Wind Speed = 5 miles/hour (45° Yaw), Typical Low Speed (Switchyard) Operation. Train Direction: to the left; Crosswind: into the page.

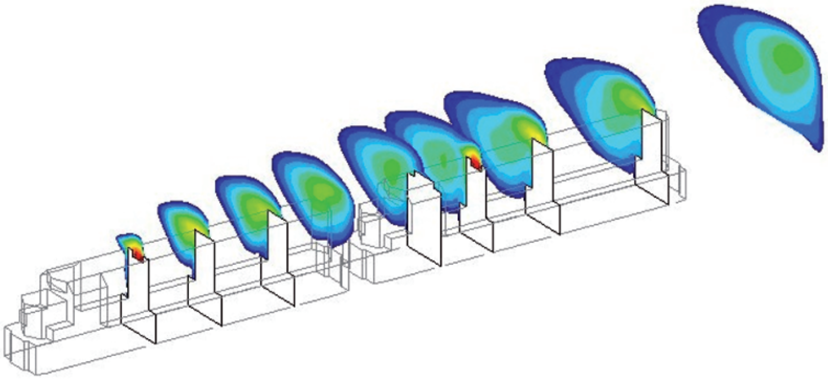

Fig. 19 Two GM EMD SD40 Locomotives, Both Oriented with Short Hood Forward, Throttle Position = Notch 5, Train Speed = 45 miles/hour, Wind Speed = 7 miles/hour (8.8° Yaw), Typical High Speed (Linehaul) Operation. Train Direction: to the left; Crosswind: into the page.

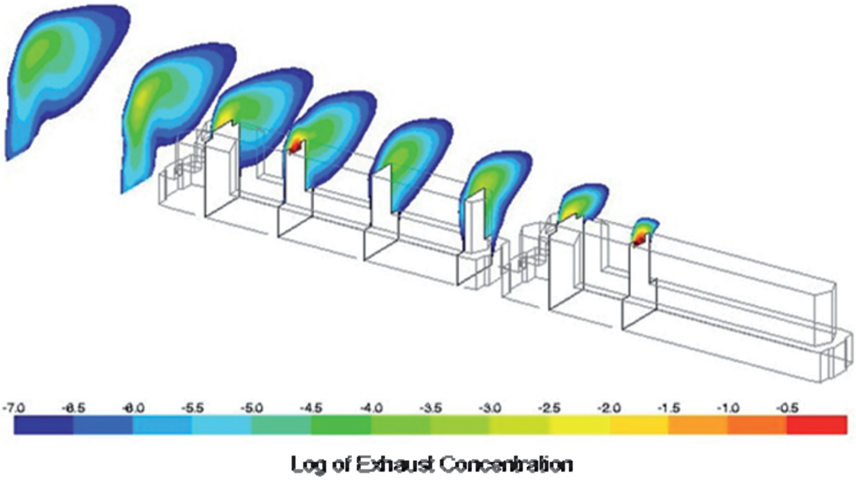

Fig. 20 Two GM EMD SD40 Locomotives, Both Oriented with Long Hood Forward, Throttle Position = Notch 5, Train Speed = 45 miles/hour, Wind Speed = 7 miles/hour (8.8° Yaw), Typical High-Sped (Linehaul) Operation. Train Direction: to the right; Crosswind: into the page.

Maximum exhaust concentrations for the lead locomotive occur for locomotives operating in line-haul service with the long hood forward and were as high as 0.008% of the concentration at the stack exit. Concentrations of exhaust at the leeward-side window of trailing locomotives were found to be relatively higher than that of the lead locomotive for either hood orientation.

Concentrations for both the gaseous components and the particulate matter present in the exhaust plume were calculated. Exhaust concentrations were obtained from the numerical simulations and component concentrations were defined using the calculation procedures. The diesel exhaust components of Table 8 can be converted to mass fractions for comparison to the results of the numerical models as shown in Table 9.

Table 9 Exhaust Flow Composition (Mass Fraction) for 2-Cycle, 12-Cylinder Diesel Engine as a Function of Throttle Position

Exhaust Gas Component	**Throttle Notch 5 Flow Rate (grams/hr)**	**Throttle Notch 5 Flow Rate (kg/sec)**	**Throttle Notch 5 Mass Fraction***	**Throttle Notch 8 Flow Rate (grams/hr)**	**Throttle Notch 8 Flow Rate (kg/sec)**	**Throttle Notch 8 Mass Fraction***
NO_x	25,584	0.0071	0.0027	47,133	0.0131	0.0038
CO	3,895	0.0011	0.0004	3,034	0.0008	0.0002
Hydrocarbons	595	0.0002	0.0001	1,375	0.0004	0.0001
SO_2	1,568	0.0004	0.0002	3,361	0.0009	0.0003
Particulate	348	0.0001	0.00004	697	0.0002	0.00006
0_2	(reported as mass fraction):		0.139	(reported as mass fraction):		0.119

* Component Mass Fraction = (component flow Rate kg/sec)/(Total Exhaust Flow Rate kg/sec)

Total Exhaust Flow Rate = 3.446 kg/sec (Notch 8) and 2.639 kg/sec (Notch 5)

Gaseous Components:

The molecular weight of the exhaust gas mixture at Notch Position 5 was calculated to be 28.875 [75]. Similarly, the molecular weight of the exhaust gas mixture at Notch Position 8 was determined to be 28.803. The following procedure was then applied to determine the mole fractions of each gaseous exhaust component at the leeward side windows for each of the simulated locomotives at both the leading and trailing positions.

A. For each of the selected simulations, obtain the mass fraction of exhaust present at the operator's cab leeward side window.
B. Determine the mass fraction of each exhaust component at the operator's cab window for each of the eight simulations and for both the leading and trailing locomotive (multiply component mass fraction by exhaust concentration at that location).
C. Calculate the mole fraction of the exhaust gas component.
D. Multiply the mole fraction by 1,000,000 to obtain the concentration for each component in ppmv.

The results for the gaseous component concentrations at the leeward-side window for the leading and trailing locomotives are shown in Tables 10 and 11, respectively.

Table 10a Calculated Exhaust Concentrations at the Leeward-Side Window of the Leading Locomotive, NO_x, CO, Hydrocarbons, SO_2.

Locomotive	Hood Forward	Yaw Angle	NO_x (ppmv)	CO (ppmv)	HCs (ppmv)	SO_2 (ppmv)
GP38	Short	45°	0.00000	0.00000	0.00000	0.00000
GP38	Short	21.8°	0.00000	0.00000	0.00000	0.00000
GP38	Long	45°	0.11646	0.00832	0.00830	0.00546
GP38	Long	21.8°	0.04037	0.00288	0.00288	0.00189
SD40	Short	49.7°	0.00000	0.00000	0.00000	0.00000
SD40	Short	8.84°	0.01252	0.00252	0.00126	0.00055
SD40	Long	49.7°	0.00621	0.00125	0.00062	0.00027
SD40	Long	8.84°	0.17326	0.03483	0.01738	0.00762

Table 10b Calculated Exhaust Concentrations at the Leeward-Side Window of the Leading Locomotive, O_2, CO_2, Aldehydes, and N_2.

Locomotive	Hood Forward	Yaw Angle	O_2 (ppmv)	CO_2 (ppmv)	Aldehydes	N_2 (ppmv)
GP38	Short	45°	0.00000	0.00000	0.00000	0.00000
GP38	Short	21.8°	0.00000	0.00000	0.00000	0.00000
GP38	Long	45°	4.33325	1.85280	0.00054	32.5184
GP38	Long	21.8°	1.50206	0.64225	0.00019	11.27201
SD40	Short	49.7°	0.00000	0.00000	0.00000	0.00000
SD40	Short	8.84°	0.76606	0.28042	0.00008	4.80206
SD40	Long	49.7°	0.38001	0.13911	0.00004	2.38212
SD40	Long	8.84°	10.5982	3.87951	0.00114	66.43475

It is noted that the concentrations in Tables 10 and 11 are for the exhaust components only. In other words, the oxygen and nitrogen components originate at the stack. Of course, oxygen and nitrogen from the surrounding air would also be present at these locations. Since the goal of the current study is to calculate the levels of exhaust components present at the operator's cab windows that originated in the engine, the concentrations of components present in the ambient air were not included.

Table 11a Calculated Exhaust Concentrations at the Leeward-Side Window of the Trailing Locomotive, NO_x, CO, Hydrocarbons, SO_2.

Loco-motive	Hood Forward	Yaw Angle	NO_x (ppmv)	CO (ppmv)	HCs (ppmv)	SO_2 (ppmv)
GP38	Short	45°	0.04893	0.00349	0.00349	0.00229
GP38	Short	21.8°	0.06834	0.00488	0.00487	0.00320
GP38	Long	45°	1.44415	0.10314	0.10296	0.06765
GP38	Long	21.8°	0.30381	0.02170	0.02166	0.01423
SD40	Short	49.7°	0.36723	0.07383	0.03685	0.01614
SD40	Short	8.84°	10.4923	2.10936	1.05280	0.46116
SD40	Long	49.7°	1.06756	0.21462	0.10712	0.04692
SD40	Long	8.84°	9.59582	1.92914	0.96285	0.42175

Table 11b Calculated Exhaust Concentrations at the Leeward-Side Window of the Trailing Locomotive, O_2, CO_2, Aldehydes, and N_2.

Loco-motive	Hood Forward	Yaw Angle	O_2 (ppmv)	CO_2 (ppmv)	Alde-hydes	N_2 (ppmv)
GP38	Short	45°	1.82078	0.77852	0.00023	13.6638
GP38	Short	21.8°	2.54299	1.08732	0.00032	19.0835
GP38	Long	45°	53.7351	22.9759	0.00673	403.248
GP38	Long	21.8°	11.3044	4.83351	0.00142	84.8327
SD40	Short	49.7°	22.4631	8.22271	0.00241	140.810
SD40	Short	8.84°	641.808	234.937	0.06886	4,023.18
SD40	Long	49.7°	65.3021	23.9042	0.00701	409.347
SD40	Long	8.84°	586.971	214.864	0.06298	3,679.43

Particulate Matter:

Emissions and exposure guidelines for diesel particulate matter are generally given in units of mass per unit volume, typically, milligrams per cubic meter. As was done with the gaseous components, a calculation procedure was developed to determine the concentrations of diesel particulate at the leeward-side windows of the leading and trailing locomotives represented in the numerical simulations. The initial calculations involve determination of the total exhaust concentration at the locomotive window locations. The concentration of exhaust, in units of percent of total mass, at the leeward-side windows of both the leading and trailing locomotives can be taken from the computer simulations. If we multiply these concentrations by 1×10^6, we obtain the entries in Table 12, which are in units of parts per million based on mass.

Table 12 Concentrations of Exhaust at Cab Windows of Leading and Trailing Locomotives on a Mass Basis

Loco-Motive	Hood Forward	Yaw Angle	Train Speed (mph)	Concentration of Exhaust at Cab Window of Lead Locomotive (ppm_{mass})	Concentration of Exhaust at Cab Window of Trailing Locomotive (ppm_{mass})
GP38	Short	45°	5	0.000	16.994
GP38	Short	21.8°	5	0.000	23.734
GP38	Long	45°	5	40.448	501.519
GP38	Long	21.8°	5	14.019	105.506
SD40	Short	49.7°	5	0.000	179.038
SD40	Short	8.84°	45	6.106	5,115.433
SD40	Long	49.7°	5	3.029	520.481
SD40	Long	8.84°	45	84.471	4,678.365

To determine the mass flow rates of particulate, the following relationship is used:

$$Mdot_p = P_s \cdot HP \qquad (8)$$

where:

$Mdot_p$ = Mass Flow Rate of Particulate (kg/sec)
P_s = Measured Particulate Emissions (kg/bhp-sec)
HP = Engine Power (bhp)

For the selected engine, throttle position Notch 5 corresponds to 1,463 horsepower and Notch Position 8 corresponds to 2,120 horsepower. Thus, the particulate flow rates at the exhaust stack for these two conditions are:

Table 13 Particulate Mass Flow Rates at Exit Plane of Diesel Engine Exhaust Stack

Loco-motive	Throttle Notch Setting	Engine Power (bhp)	Tested Emissions		Particulate Mass Flow	
			Low Value (kg/bhp-sec)	High Value (kg/bhp-sec)	Low Value (kg/sec)	High Value (kg/sec)
GP38	8	2,120	3.89×10^{-8}	6.67×10^{-8}	8.25×10^{-5}	1.41×10^{-4}
SD40	5	1,463	3.89×10^{-8}	6.67×10^{-8}	5.69×10^{-5}	9.76×10^{-5}

To calculate the particulate concentrations at the cab window locations, the following relationship was used:

$$\text{Particulate Concentration (mg/m}^3) = [(MF_e) \times (MFR_p / MFR_e)] \times [\rho_m] \times (10^6 \text{ mg/kg}) \qquad (9)$$

where: MF_e = mass fraction of exhaust at leeward window location (from simulation)
MFR_p = mass flow rate of particulate at exhaust stack (kg/sec)

MFR_e = mass flow rate of exhaust (kg/sec)
ρ_m = density of air and exhaust gas mixture

The density of the air and exhaust gas mixture can be determined from the ideal gas law:

$$\rho_m = [(T_{ssc} + 273\ °C)/(T_w + 273\ °C)] \times [\rho_{ssc}] \tag{10}$$

where: T_{ssc} = Temperature (°C) at sea level, standard conditions
T_w = Temperature at window location (°C)
ρ_{ssc} = Density at sea level, standard conditions

The results of the particulate concentration analysis for both the leading and trailing locomotives and for the lower and upper value of measured particulates at the stack are presented in Tables 14 and 15.

Table 14 Particulate Concentrations at Cab Windows of Leading and Trailing Locomotives Based on Lower Value of Particulate Emissions at Stack.

Loco-Motive	Hood Forward	Yaw Angle	Train Speed (mph)	Concentration of Particulate at Cab Window of Lead Locomotive (mg/m^3)	Concentration of Particulate at Cab Window of Trailing Locomotive (mg/m^3)
GP38	Short	45°	5	0.0000	0.0005
GP38	Short	21.8°	5	0.0000	0.0007
GP38	Long	45°	5	0.0011	0.0142
GP38	Long	21.8°	5	0.0004	0.0030
SD40	Short	49.7°	5	0.0000	0.0046
SD40	Short	8.84°	45	0.0002	0.1303
SD40	Long	49.7°	5	0.0001	0.0133
SD40	Long	8.84°	45	0.0022	0.1192

Table 15 Particulate Concentrations at Cab Windows of Leading and Trailing Locomotives Based on Upper Value of Particulate Emissions at Stack.

Loco-Motive	Hood Forward	Yaw Angle	Train Speed (mph)	Concentration of Particulate at Cab Window of Lead Locomotive (mg/m^3)	Concentration of Particulate at Cab Window of Trailing Locomotive (mg/m^3)
GP38	Short	45°	5	0.0000	0.0008
GP38	Short	21.8°	5	0.0000	0.0012
GP38	Long	45°	5	0.0020	0.0244
GP38	Long	21.8°	5	0.0007	0.0051
SD40	Short	49.7°	5	0.0000	0.0078
SD40	Short	8.84°	45	0.0003	0.2234
SD40	Long	49.7°	5	0.0001	0.0228
SD40	Long	8.84°	45	0.0037	0.2044

Results and Conclusions, Section III: Diesel Exhaust Plume Behavior

Calculation procedures have been developed to determine the concentrations of diesel exhaust components, both gaseous and particle, at the leeward-side operator's cab window for both leading and trailing locomotives. Exhaust concentrations were obtained from CFD simulations and component concentrations were defined using the calculation procedures.

Calculations of the exhaust concentrations and exhaust components at the locomotive leeward-side windows showed several interesting results.

a) In switchyard and low-train-speed operations, exhaust concentrations at the trailing locomotive window are typically 10 to 800 times greater than those at the leading locomotive window when both locomotives have the same hood orientation.

b) In switchyard and low-train-speed operations, exhaust concentrations at the leeward-side window of the leading locomotive when operated with the long-hood-forward are between 3 and 30 times greater than those at the same location when the locomotive is operated with the short-hood-forward.

c) For line-haul operations, the recirculation zone on the leeward side of the locomotives is very strong and remains in closer proximity to the leeward side of the train. Exhaust concentrations at the leading locomotive cab leeward-side window with the locomotives oriented with the long-hood-forward are 14 times greater than those at the same location when the locomotives are oriented with the short hood forward. For the trailing locomotive, the exhaust concentrations at the leeward window are nearly equal for both the short-hood-forward and long-hood-forward orientations, again due to the strong vortex (recirculation zone) present in this area during high-speed operation.

d) The same trends were seen with the concentrations of particulate matter.

e) Because of the strong vortex pattern and high levels of turbulence on the leeward side of the locomotive, the diesel exhaust components are transported to the interior of the operator's cab through open windows. For high-speed line-haul operation, diesel exhaust components are present at the operator's cab window even when the locomotive is operated with the short-hood forward.

Conclusions and Suggestions for Future Research

CFD methods have been shown to be effective at evaluating the aerodynamics of rail cars and locomotives. The methods were employed to quantify the drag characteristics of external railcar features including well car side-posts and inter-platform gaps. Simulation results were coupled with wind tunnel tests to develop a database of tip-over tendencies for a variety of car types. Additionally, CFD models were developed for several locomotives operating under a number of ambient conditions (wind speed, wind direction). The concentration of diesel exhaust at the operator cab window was quantified. Correlations of the CFD results with previously collected wind tunnel and field data were performed for many of the simulations.

Additional research is suggested including: continued evaluation of rail car drag reduction designs using advanced CFD methods, additional wind tunnel and field tests to verify the various CFD models, and wind tunnel measurements of exhaust plume concentrations to verify simulation results.

Acknowledgments

This work was funded by the following organizations, which also approved release of the results: 1) Aerodynamic Drag Reduction: The Greenbrier Companies, 2) Wind-Induced Tip-Over: Norfolk Southern Railway Company, and 3) Diesel Exhaust Plume Behavior: Doffermyre Shields Canfield Knowles & Devine, LLP, and Romanucci & Blandin, LLC. Preparation of this paper was funded by Airflow Sciences Corporation.

References

[1] Anderson D., Tannehill J and Pletcher R, *Computational Fluid Dynamics and Heat Transfer*, Washington, Hemisphere Publishing Corporation, 1984.
[2] Wesseling P, *Principles of Computational Fluid Dynamics*, Heidelberg, Springer-Verlag, 2000.
[3] McCallen R, Browand F and Ross J (Editors), *The Aerodynamics of Heavy Vehicles: Trucks, Buses, and Trains,* New York, Springer-Verlag, 2004.
[4] Hucho W (Editor), *Aerodynamics of Road Vehicles*, Fourth Edition, Society of Automotive Engineer, Warrendale, Pennsylvania, 1998.
[5] Nelson R and Banka A, *VISCOUS Users Guide*, Livonia, Michigan, Airflow Sciences Corporation, 1993.
[6] Patankar S, *Numerical Heat Transfer and Fluid Flow*, New York, Hemisphere Publishing Corporation, 1980.
[7] *FLUENT 6.3 User's Manual,* Lebanon, New Hampshire, ANSYS, Inc., 2007.

[8] Launder B and Spalding D, *Mathematical Models of Turbulence*, New York, Academic Press, 1972.
[9] Launder B and Spalding D, “The Numerical Computation of Turbulent Flow”, *Comp. Methods Appl. Mech. Eng.,* vol. 3, 1974, p. 269.
[10] Ahmed S, “Some Applications of RANS Methods”, Section 15.6.3.2, Computational Fluid Dynamics, Chapter 15, *Aerodynamics of Road Vehicles*, Hucho, W. H. (Editor), Fourth Edition, Society of Automotive Engineer, Warrendale, Pennsylvania, 1998.
[11] Ellis H, *The Pictorial Encyclopedia of Railways*, New York, Hamlyn Publishing Corporation, 1968, pp. 12-30.
[12] Hammitt A, “Aerodynamic Forces on Freight Trains, Volume I – Wind Tunnel Test of Containers and Trailers on Flatcars”, U. S. Department of Commerce, NTIS PB-264 304, December 1976.
[13] Joshi P, “Aerodynamic Forces on Freight Trains, Volume II – Full-Scale Aerodynamic Validation Tests of Trailer-On-A-Flat-Car (Series II)”, U.S. Department of Commerce, NTIS PB-281 823, March 1978.
[14] Hammitt A, “Aerodynamic Forces on Freight Trains, Volume III – Correlation Report, Full Scale Trailers on Flat Cars and Comparison with Wind Tunnel Results”, U.S. Department of Commerce, NTIS PB-288 137, September 1978.
[15] Hammitt A, “Aerodynamic Forces on Freight Trains, Volume IV – Wind Tunnel Tests of Freight Cars and New Trailer and Container Car Designs”, U.S. Department of Commerce, NTIS PB80-174 899, June 1979.
[16] Hammitt A, “Aerodynamic Forces on Various Configurations of Railroad Cars for Carrying Trailers and Containers. Wind Tunnel Tests of Six Scale Model Configurations”, U. S. Department of Commerce, NTIS PB80-174881, January 1979.
[17] Arnold G, “Synopsis, Full-Scale Aero-Drag-Measuring Gondola Car”, Workshop on the Aerodynamic Drag of Trains, Derbyshire College of Higher Education, Derby, U.K., April 7-9, 1986.
[18] Gawthorp R, “Aerodynamics of Trains in the Open Air”, *Railway Engineer International*, Volume 3, No. 3, May-June 1978, pp. 7-12.
[19] Dayman D, “Demonstration of the Coast-Down Technique for Determining Train Resistances”, Final Report, Jet Propulsion Laboratory, Pasadena, California, Publication No. 83-85, October 1983.
[20] Goss W, “Atmosphere Resistance to the Motion of Railway Trains”, *The Engineer*, 1898 (conducted at Purdue University).
[21] Hoerner S, “Efficiency of Railroad Trains”, *Fluid Dynamic Drag*, Hoerner Fluid Dynamics, Brick Town, New Jersey, 1965, pp. 12-10 to 12-15.
[22] Tietjens O and Ripley K, “Air Resistance of High-Speed Trains and Interurban Cars”, *Transactions ASME*, Vol. 54 (APM-54-23), 1932, pp. 235-251.
[23] Davis W, “The Traction Resistance of Electric Locomotives and Cars”, *General Electric Review*, Vol. 29, October 1926, pp. 685-707.
[24] Hay W, *Railroad Engineering*, New York, John Wiley and Sons, 1982, pp. 69-89.
[25] Engdahl R, Gielow R and Paul J, “Train Resistance – Aerodynamics, Volume I of II, Intermodal Car Aerodynamics”, Association of American Railroads, 1987.
[26] Paul J, Gielow R, Holmes A and Hickey P, “Reduction of Intermodal Car Aerodynamic Drag through Computerized Flow Simulation”, American Society of Mechanical Engineers, Paper 83-RT-4, 1983.
[27] Arad U, *The 1973-1974 Arab Oil Embargo: Facts, Figures and Analysis*, Washington, D.C., Hudson Institute, 1974.
[28] Widjaja D, Scofield J, Holmes A and Gielow R, “An Application of Airflow Modeling Methods to the Santa Fe 10-Pack Fuel Foiler”, Livonia, Michigan, Airflow Sciences Corporation Report R-80-004, 1 October 1980.

[29] MacFadyen A, Widjaja D, Holmes A, Paul J and Gielow R, “An Aerodynamic Drag Comparison of Streamlined and Conventional Locomotives Utilizing Numerical Airflow Simulation Methods”, Livonia, Michigan, Airflow Sciences Corporation Report R-81-011, June 1981.

[30] Hickey P, MacFadyen A, Holmes A, Paul J and Gielow R, “An Aerodynamic Analysis of the Trailer Train Company 4-Runner Intermodal Car Using Numerical Flow Simulation Methods”, Livonia, Michigan, Airflow Sciences Corporation Report R-82-005, 7 May 1982.

[31] Hickey P, Gielow R, Holmes A and Paul J, “Aerodynamic Drag Analysis of the Lo-Pac 2000 Intermodal Car”, Livonia, Michigan, Airflow Sciences Corporation Report R-82-011, 15 September 1982.

[32] Gielow R, Holmes A and Paul J, “Aerodynamic Drag Analysis of the Ortner 100-Ton Rapid Discharge Car”, Livonia, Michigan, Airflow Sciences Corporation Report R-82-014, 15 December 1982.

[33] Hickey P, Gielow R, Holmes A and Paul J, “Aerodynamic Modifications to the Budd Lo-Pac 2000 Intermodal Car”, Livonia, Michigan, Airflow Sciences Corporation Report R-83-001, 31 January 1983.

[34] Hickey P, Holmes A, Paul J and Gielow R, “Aerodynamic Design Study of an Aluminum Gondola Car for Pullman Standard”, Livonia, Michigan, Airflow Sciences Corporation Report R-83-005, 1 April 1983.

[35] Hickey P, Gielow R and Paul J, “An Aerodynamic Treatment Package for the Ortner Four Pocket Rapid Discharge Coal Car”, Livonia, Michigan, Airflow Sciences Corporation Report R-83-013, 5 August 1983.

[36] Paul J, Smith T, Gielow M and Gielow R, “ 3/10 Scale Wind Tunnel Test of Skeletonized and Well-Type Intermodal Rail Cars”, Livonia, Michigan, Airflow Sciences Corporation Report R-83-019, 1 October 1983.

[37] Paul J, Nelson R, Groesbeck P, Polihonki D, Banka A, Keeler D and Gielow R, “3/10 Scale Hopper and Gondola Rail Car Wind Tunnel Test”, Livonia, Michigan, Airflow Sciences Corporation Report R-84-019, 28 December 1984.

[38] Paul J and Gielow R, “Aerodynamic Enhancements of the Trailer Train Front Runner Single Platform Rail Car”, Livonia, Michigan, Airflow Sciences Corporation Report R-84-009, 1 June 1984.

[39] Gielow R, Keeler D, Polihonki D, deJager D and Paul J, “16% Scale Gondola, Locomotive, and 89 Foot Car Wind Tunnel Test”, Livonia, Michigan, Airflow Sciences Corporation Report R-85-011, 31 January 1986.

[40] Engdahl R, Gielow R and Paul J, “Train Resistance – Aerodynamics, Volume II of II, Open Top Car Applications”, Association of American Railroads, 1987.

[41] Furlong C, Gielow M., Gielow R Paul J and Nelson R, “Results of Wind Tunnel and Full-Scale Tests Conducted from 1983 t 1987 in Support of The Association of American Railroad’s Train Energy Program”, Livonia, Michigan, Airflow Sciences Corporation Report Number R-88-010, 30 December 1988, AAR Report R-685.

[42] Furlong C, Gielow R, Paul J and Nelson R, “Aerodynamic Subroutine User’s Guide, Train Aerodynamics Simulator”, Livonia, Michigan, Airflow Sciences Corporation Report R-88-003, 15 July 1988.

[43] Polihonki D, Paul J and Banka A, “An Aerodynamic Optimization of the Front End Design for a Proposed Euroshuttle Train Double Deck Loader”, Livonia, Michigan, Airflow Sciences Corporation Report R-90-003, 15 January 1990.

[44] Johnson R, “Fuel Consumption Analysis of Various Railcars”, Livonia, Michigan, Airflow Sciences Corporation Report L-94-GB1-4, 12 September 1994.

[45] Johnson R, “Auto Hauler Fuel Consumption Analysis”, Livonia, Michigan, Airflow Sciences Corporation Report L-98-GBC-1, 28 April 1998.

[46] Johnson R, “Wind Tunnel Results of a 16%-Scale Partitioned Gondola Car”, Livonia, Michigan, Airflow Sciences Corporation Report L-04-ICE-1, 15 December 2004.

[47] Johnson R, “CFD Analysis of Smooth-Side (Husky-Stack 53) and Side Post 53 Foot Well Cars”, Livonia, Michigan, Airflow Sciences Corporation Report L-06-GB5-3, 29 November 2006

[48] Johnson R, “Coal Car Aerodynamics”, Livonia, Michigan, Airflow Sciences Corporation Reports L-06-BNS-1 and L-07-BNS-1, 5 December 2006 and 18 April 2007.

[49] Johnson R, “Maxi-X AP1 and Maxi-X MS Fuel Consumption Results”, Livonia, Michigan, Airflow Sciences Corporation Report L-94-GBI-1, 24 June 1994.

[50] Watkins S, Saunders J and Kumar H, “Aerodynamic Drag Reduction of Goods Trains”, *Journal of Wind Engineering and Industrial Aerodynamics”*, Vol. 40 (1992) pp. 147-178.

[51] Saunders J, Watkins S and Cassar R., “Vortex Optimisation of Slotted Tops and Cavities of Two Different Open Rail Wagons”, *Journal of Wind Engineering and Industrial Aerodynamics*, Vol. 49 (1993), pp. 421-430.

[52] Johnson R, “CFD Analysis of Enhanced HS 40X US Well Car”, Livonia, Michigan, Airflow Sciences Corporation Report L-07-GB3-1, 27 February 2007.

[53] Matschke G, Tielkes T, Deeg P and Schulte-Werning B, “Effects of Strong Cross Winds on High-Speed Trains – A Risk Assessment Approach”, International Association for Probabilistic Safety Assessment and Management, PSAM5 Conference, Osaka, Japan, 27 November 2000.

[54] Andersson E, Haggstrom J, Sima M and Stichel S, “Assessment of Train-Overturning Risk Due to Strong Cross-Winds”, Proceedings of the I MECH E Part F *Journal of Rail and Rapid Transit*, Volume 21 B, Number 3, 1 September 2004.

[55] Sanquer S, Barre C, Dufresne de Virel M and Cleon L, “Effects of Cross Winds on High-Speed Trains: Development of a New Experimental Methodology”, *Journal of Wind Engineering and Industrial Aerodynamics*, Vol. 92, Issues 7-8, June 2004, pp. 535-545.

[56] MacNeill R, Holmes S and Lee H, “Measurement of the Aerodynamic Pressures Produced by Passing Trains”, *Proceedings of the 2002 ASME/IEEE Joint Rail Conference*, Washington, DC, 23-25 April 2002.

[57] Holmes S, Toma E and Schroeder M, “High-Speed Passenger and Intercity Train Aerodynamic Computer Modeling”, *Proceedings of ME2000*, The 2000 International Mechanical Engineering Congress & Exposition, Orlando, Florida, 5-10 November 2000.

[58] Hoppmann U, Koenig S, Tilkes T and Matschke G, “A Short-Term Strong Wind Prediction Model for Railway Application; Design and Verification”, *Journal of Wind Engineering and Industrial Aerodynamics*, Vol. 90, 2002, pp. 1127-1134.

[59] Polihonki D, Paul J, Gielow R and Nelson R, “An Aerodynamic Evaluation of the Front End Design for a Bombardier Mass Transit Division Proposed Euroshuttle Train Double Deck Loader (DDL) Wagon, Livonia, Michigan, Airflow Sciences Corporation Report R-90-003, 15 January 1990.

[60] Gielow M, Polihonki D, Gielow R Paul J and Nelson R, “A Train-Speed-Restricting System to Achieve Safe Operations under High Wind Conditions Along Certain Union Pacific Routes”, Livonia, Michigan, Airflow Sciences Corporation Report R-88-006, 26 August 1988.

[61] Johnson R, “Auto-Max Tip-Over Analysis”, Livonia, Michigan, Airflow Sciences Corporation Report L-98-GB1-1, 12 August 1998.

[62] Johnson R and Nelson R, “Norfolk Southern Company Sandusky Bay Speed Restricting System”, Livonia, Michigan, Airflow Sciences Corporation, Report R-06-NF1-1, 3 April 2006.

[63] Paul J, Groesbeck P, Gielow M, Keeler D, Banka A and Gielow R, “Southern Pacific Transportation Company 3/10 Scale Double-Stack Container Car Wind Tunnel Test”, Livonia, Michigan, Airflow Sciences Corporation Report R-84-015, 4 October 1984.

[64] Peters J, “How to Reduce the Cross Wind Sensitivity of Trains”, *The Aerodynamics of Heavy Vehicles: Trucks, Buses, and Trains,* McCallen, R., Browand, F., and Ross, J. (Editors), New York, Springer-Verlag, 2004, pp. 453-467.

[65] Bhatia R, Lopipero P and Smith A, "Diesel Exhaust Exposure and Lung Cancer", *Epidemiology*, Vol. 9 (1), January 1998, pp. 84-91.

[66] Nauss K, "Diesel Exhaust: A Critical Analysis of Emissions, Exposure, and Health Effects; Summary of a Health Effects Institute (HEI) Special Report: HEI Diesel Working Group", Cambridge, Massachusetts, DieselNet Technical Report, October 1997.

[67] Woskie S, Smith T, Hammond S, Schenker M, Garshick E and Speizer F, "Estimation of the Diesel Exposures of Railroad Workers: I. Current Exposures", *American Journal of Industrial Medicine*, Vol. 13, 1988, pp. 381-394.

[68] Woskie S, Smith T, Hammond S, Schenker M, Garshick E and Speizer F, "Estimation of the Diesel Exhaust Exposures of Railroad Workers: II. National and Historical Perspectives", *American Journal of Industrial Medicine*, Vol. 13, 1988, pp. 395-404.

[69] Correspondence, Brotherhood of Locomotive Engineers and Trainsmen, Cleveland, Ohio, 1986-1989.

[70] Liukonen L, Grogan J and Myers W, "Diesel Particulate Exposure to Railroad Train Crews", *American Industrial Hygiene Association Journal*, Vol. 63 (5), Sep.-Oct. 2002, pp. 610-616.

[71] "Diesel Engine Exhaust", *Health Hazard Advisory*, Hazard Evaluation System & Information Service, California Department of Health Services, Occupational Health Branch, November 2002.

[72] American Society of Heating, Refrigeration, and Air Conditioning Engineers (ASHRAE), *2007 ASHRAE Handbook*, Chapter 44, "Building Air Intake and Exhaust Design, Atlanta Georgia, 2007.

[73] Banka A, Gielow M., Paul J and Gielow R, "A Wind Tunnel Evaluation of Engine Exhaust Flow Patterns from a C39-8 Locomotive, Long Hood Forward", Livonia, Michigan, Airflow Sciences Corporation Report R-86-015, 26 September 1986.

[74] Ellsworth K, (Editor), and Houser F and Whitney D (Contributing Editors), *The Car and Locomotive Cyclopedia of American Practice*, Fourth Edition, Simmons-Boardman Publishing Corporation, Omaha, Nebraska, 1980.

[75] Paul J, Linfield K and Banka A, "Determination of Diesel Exhaust Plume Concentrations within Operator Cabs of Selected Locomotives", Livonia, Michigan, Airflow Sciences Corporation Report R-04-DS1-01, 3 December 2004.

[76] Paul J and Linfield K, "Assessment of Diesel Exhaust Plume Exposure Levels within Operator Cabs of Railroad Locomotives", Livonia, Michigan, Airflow Sciences Corporation Report R-06-RBL-01, 19 October 2006.

[77] National Climatic Data Center, Asheville, North Carolina, *Climatic Wind Data for the United States*, November 1998, for the time period 1930 through 1996. Refer to Web Site: www.ncdc.noaa.gov.

[78] Fritz S, Southwest Research Institute, "Locomotive Exhaust Emissions: Past Studies, Present Work, and Future Challenges", Presentation to the Society of Automotive Engineers, TC-9 Committee Meeting, Salt Lake City, Utah, January 1998.

[79] Fritz S, Southwest Research Institute, "Emissions Measurements – Locomotives", EPA Work Assignments 1-4 and 2-4, Contract No. 68-C2-0144, SwRI Report No. 5374-024, August 1995.

[80] Bauer H, Editor in Chief, *Bosch Automotive Handbook*, 4th Edition, 1996, Published by Robert Bosch GmbH, "Exhaust Emissions from Diesel Engines", pp. 530-531.

[81] Fritz S, Southwest Research Institute, "Diesel Fuel Effects on Locomotive Exhaust Emissions", 23rd CIMAC Congress, Paper No. 7A-05, May 2001.

[82] Video Tape (VHS Format) provided by General Electric Transportation Systems, GE WMM Loco Track Test on NS Smoke Ventilation", 17 August 1989.

[83] Whitaker L, "Diesel Exhaust Fume Study in GE C39-8 Cabs", Norfolk Southern Corporation, Mechanical Department, File 142.3, 22 August 1988.

[84] Beem D, "Diesel Fume Monitoring, Locomotive 3532", Norfolk Southern Corporation, File IH13, 13 September 1994.

Data Acquisition of a Tractor-Trailer Combination to Register Aerodynamic Performances

Gandert M.R. Van Raemdonck and Michel J.L. van Tooren

Faculty of Aerospace Engineering - Delft University of Technology - 2629HS Delft, The Netherlands
g.m.r.vanraemdonck@tudelft.nl

Abstract The design, production and verification of a data acquisition system to measure aerodynamic and mechanical characteristics of a tractor-trailer combination, operating in a real life environment, are presented. The main goal of this work is to derive a reference level of a truck with respect to its aerodynamic and mechanical performances. This way, if the truck is equipped with different aerodynamic aids, a correct comparison can be made between the aerodynamic drag reductions obtained by these devices. Also, a relation can be defined which links the aerodynamic drag reduction with fuel consumption savings. The acquisition system consists of an anemometer, which measures the wind speed and direction, and a two-axis inclination indicator, which is coupled to the FMS of the tractor via the CAN communication system and to the wipers to indicate if it is raining or not. The FMS of the tractor is measuring, for instance, the vehicle speed, the engine torque, the rpm, acceleration pedal position, cruise control, fuel rate, cargo weight and the like. All the measured data are registered on a hard disk and can be accessed through a simple USB connection. The processed data gives insight in the performance of the driver and in the aerodynamic behavior (C_D value of 0.430) as well as the mechanical characteristics (power required breakdown; 47% rolling resistance, 39% aerodynamic drag and 15% mechanical losses; average speed of 75 km/h; fuel consumption of 30 liters per 100 km) of the truck.

1 Introduction

The heavy duty transport industry which uses trucks to transport cargo is a very large business area since it is still the most used transport solution to deliver consumer goods. This fact manifests itself in an increasing amount of trucks on the road and in increased total fuel consumed, together with the related cost, for road transport. Due to the rising fuel prices it is crucial however, to find solutions for this high fuel cost in order to stay competitive in this aggressive and fast changing market due to, for instance, the growth of the European Union. Generally there are two ways to reduce the fuel consumption of a vehicle. One can improve the efficiency of the available power which means an increase of the power delivered by the engine or, on the other hand, the required power that is needed to overcome the forces needs to be lowered. Considering the latter, it signifies achieving a reduction of fuel consumption by minimizing the weight of the vehicle and/or reducing its aerodynamic drag. Also the friction resistance of the tires is an important aspect with respect to the fuel consumption of road vehicles.

The reduction of fuel consumption of trucks by aerodynamic means has become an accepted practice in the last decades by mounting add-on devices for the tractor and the trailer. Also modifications of the main shape of the vehicle improved the aerodynamic efficiency in a positive way. Besides extensive wind tunnel testing, road testing of the aerodynamic devices is needed to convince the transportation market of the effectiveness of the aids. In this perspective a data acquisition system is designed, built and installed on a truck for the purpose of collecting data of the aerodynamic and mechanical performances of the vehicle and to register the behavior of the truck driver. The following collected parameters offer a complete overview of the performances: wind speed and direction, inclination and banking angle, vehicle speed, torque, rpm, vehicle weight, fuel consumption, distance traveled, cruise control activation, brake and acceleration pedal position.

The data acquisition system will be used to define a reference level of a particular truck, which is the starting point to compare different measured fuel economy improvements of several aerodynamic aids consistently. It also makes it possible to define a relation between the aerodynamic drag reduction and the fuel savings like M.J. Rose [1]. Previous road tests and investigations [2, 4, 3] have shown that the side wind is responsible for a small, but impossible to ignore, drag rise. In this respect it is important to consider a certain range of side winds during the design of vehicles and aerodynamic devices. Therefore the vehicle speed and wind direction are being measured and can be used as input data for numerical simulations and wind tunnel experiments.

The results which are discussed below are obtained from the installed data acquisitions system in a European tractor-trailer configuration of Jan de Rijk Transport (DAF XF95 type Space-cab with 3-axle trailer) which was transporting cargo all through West Europe in the period of February until July 2006. The registered data was downloaded weekly and processed with the aid of Matlab in order to get the desired output.

2 Sensors

WindSonic

The wind direction and speed is measured with the Windsonic [5], Fig.1, provided by Gill instruments. The WindSonic is a lightweight unit (0.5 kg) of robust construction, manufactured in a polycarbonate blend material which proved to installation and use without damage. The WindSonic measures the time taken for an ultrasonic pulse of sound to travel from the North transducer to the South transducer, and compares it with the time for a pulse from S to N transducer. In the same way the times are compared between West and East, and E to W transducers. The output of the WindSonic goes via a RS232 protocol and is picked up by a RS232 to CAN (Controller Area Network) device developed by Squarell Technology [6]. In order to guarantee the accuracy of the measurements it is important to know if it's raining. Therefore a sensor cable is connected to the engines of the windscreen wipers.

2-axis incline indicator

The second sensor mounted on the chassis of the truck is the two-axis incline indicator [7], which measures the pitching and banking angle, fig.1. The two-axis incline indicator has die cast aluminum housing with two integrated sensors for measuring inclinations along two axes. As well as the sensors, the box contains two independent signal conditioners, each with a 4-20mA, 2-wire output, and two separate voltage supply feeding of the corresponding current loop, one for each sensor. The two-axis incline indicator gives a range of 4 to 20 mA as output signal that corresponds to the calibrated range of angles. The Volt-mAmpere device of Squarell Technology receives the mA signals in a proper way.

Fleet Management System

Recent modern trucks are equipped with a Fleet Management System (FMS) which is a communication system with CANbus cable connections that measures and can register many variables amongst others engine power and torque, fuel consumption, velocity, rpm, vehicle weight, etc. according to the performance and the behavior of the truck and its driver. This data should enable us to create a blueprint of the circumstances of the surroundings and break up the total required power in the different components. The sensors that are being used by the FMS to measure the truck related data are standard and already present on the truck.

3 Data Acquisition System

The desired data is logged with the aid of an ILogCan device developed by Squarell Technology. The ILogCan which is being used can store a total amount of 516MB and is linked simply with a USB-cable connected to a laptop to log the data. A special cable will link the ILogCan trough the FMS-plug to the CANbus communication system of the truck.

The total data acquisition system together with both the WindSonic and the 2-axis incline indicator are being installed in the cabin, on the roof of the cabin and onto the chassis of the truck behind the cabin of the DAF XF95. The different Squarell devices (RS323 to can, digital input device, V-mA device and ILogCan) are orderly assembled together into a waterproof electro box, Fig.1.

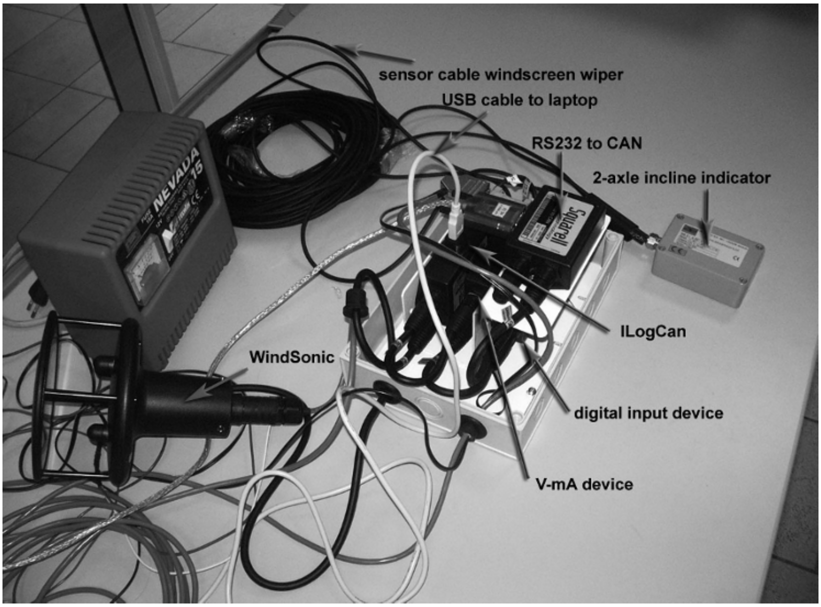

Fig. 1 Assembly of the data acquisition system.

The ILogCan is linked to the board computer of the truck through a special FMS to a DAF cable plugged in the CDM (Command Data Module) unit in the fuse box of the truck. The 12V power supply for the data acquisition system and the Wind- Sonic are also situated in this fuse box behind the passenger dashboard. A special bracket of stainless steel for the WindSonic is made to provide enough stiffness and is mounted in the symmetric plane just in front at the top roof of the cabin. The two-axis incline indicator is fixed onto the chassis behind the cabin with a small stainless plate together with simple vibration dampers and bolts.

4 Results

The 500MB of data obtained by the measurement system is saved in four different text-files and are analyzed and processed with the aid of Matlab. The data acquisition system and the sensors were installed in the DAF XF95 at the beginning of February. Only the measurements from the 22th of May until the 28th of June 2006 will be discussed. The 28th of June was the last day of the measurements and the day the system was disassembled from the truck. To reduce the amount of working and memory time, the number of cells are reduced by taking an average over four measuring points, meaning that each value represents 2 seconds in time. With the aid of descriptive statistics and SPSS more general insight in the performance of the vehicle is possible. Besides the descriptive statistics possible relations between the different measured parameters are being investigated.

4.1 Descriptive Statistics

Vehicle velocity

Figure 2a shows the frequencies (number of measuring points during the test period) of the vehicle speed during the measuring period. The first thing that catches the eye is the large amount of time (in terms of percentage) when the vehicle is standing still. Also two different peaks at 80 km/h and 90 km/h are noticeable. Apparently the driver is driving at different maximum velocities in different countries. The average speed considering the whole data set is equal to 60 km/h while the average vehicle speed without the stops of the vehicle is 75 km/h. This second data set showed that 40% of the time the velocity was higher than 89 km/h.

Wind direction and wiper

Defining a range of wind directions is important for the wind tunnel tests to obtain a realistic representation of the real circumstances concerning the wind direction. The wind directions which are corresponding with the zero vehicle velocities are filtered out of the data set. A histogram of all the different measured wind directions (180° corresponds with straight ahead wind) during the described period can be seen in Fig.2b. The percentile table indicates that 30% of the total number of occurring wind directions is centered around 178° and 179°. The range 170°-190° represents 88% of the total range of wind directions. The histogram tell us that more directions are measured which are coming from the left (direction lower than 180°). This statement is also supported by a skewness of 1,288 for the data set. The wipers were activated when it was raining during the registration period. Within rainy conditions the WindSonic is not measuring well. Only 4% of the testing period, it was raining, meaning that only 4% of the total data measured by the WindSonic and plot in the above figures is not reliable. This 4% is plausible due to the very hot weather between 22th of May and 28th of June 2006.

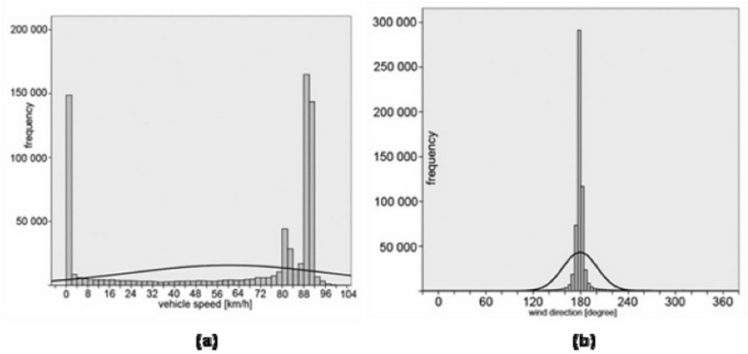

Fig. 2 (a) Overview of the measured vehicle velocities together with the mean; (b) Overview of the filtered wind directions together with the mean.

Acceleration pedal position, cruise control activation and brake switch

The behavior of the truck driver with respect to the acceleration pedal position is summarized in the next Fig.3a. Very remarkable is that during almost 75% of the time he does not touch the acceleration pedal. 8.6% of the rest of the time the driver is touching the pedal full throttle. Figure 3b tells us that 44.7% of the total time the driver has activated the cruise control. From the time the truck driver is not pushing down the acceleration pedal 6.7% he is braking to decelerate the vehicle.

Fuel rate and total fuel

The ratio between the total fuel used and the total distance traveled for the whole testing period is 0.3. In other words, 30 liters of diesel is consumed per 100 km traveled.

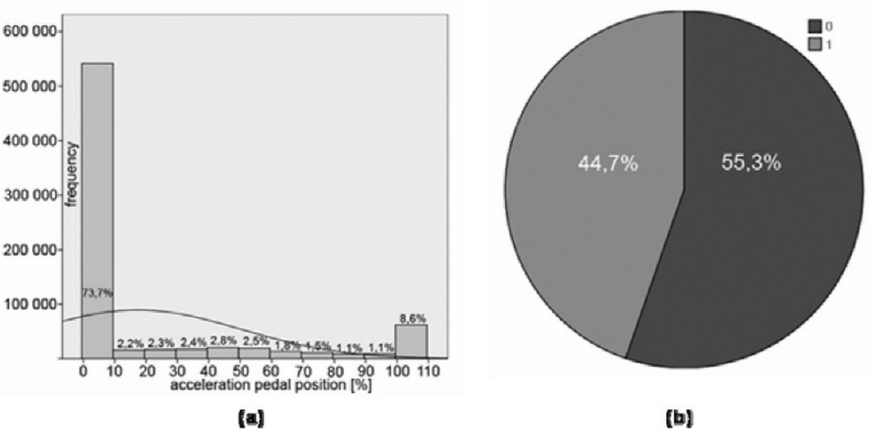

Fig. 3 (a) Overview of the acceleration pedal position together with the mean; (b) Indication of the cruise control activation.

4.2 Relations

Drag coefficient estimation

Equation.1 below describes the measured delivered power in relation to the different required power contributions to overcome the aerodynamic and friction forces and the total losses.

$$P_{req} = D_{aero} \cdot V + F_{friction} \cdot V + P_{losses} \tag{1}$$

P_{req} corresponds to the required power that is produced by the engine and is registered by the data acquisition system whereas $D_{aero} \cdot V$ is the aerodynamic force multiplied by the vehicle velocity. The friction force $F_{friction}$ originates from the friction between the wheels of the truck and the road. The friction force is dependent on the normal force N and the rolling resistance coefficient μ. The normal force N equals the weight m times the gravitational acceleration g. The weight m is composed out of the weight of the truck together with the trailer and the cargo.
Due to the absence of the required sensor to measure the cargo weight only a rough estimation could be made of the cargo weight. The rolling resistance coefficient depends mainly on the load, the inflation pressure; the speed and the remaining tire tread depth. A rolling coefficient of 0.0072 is suggested by Goodyear. The last variable in Eq.1 is the total power loss P_{losses} due to mechanical friction. If these total losses are known one can make an estimation of the drag coefficient of the truck with the aid of the measured delivered power and the calculated wheel

friction force. People of the DAF distribution center in Zwolle, The Netherlands provided a performance diagram of a DAF XF95 tractor which was equipped with the same engine (280kW/381hp) identical to the truck being used. This performance diagram can be seen in Fig.4a and is obtained by testing the particular tractor on a testing bench with a load of a half ton on the traction axis. The figure resembles the power delivered by the engine, the power measured at the wheels, the power loss (which is the difference between power engine and power loss) and finally the torque with respect to the engine revolutions per minute.

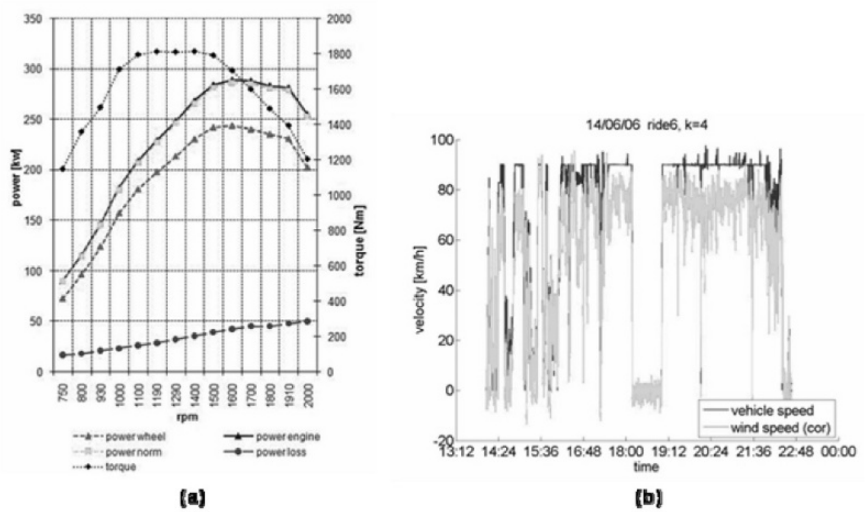

Fig. 4 (a) Engine performance diagram for a DAF XF95; (b) Estimated drag coefficient together with vehicle velocity.

With this data, a relation can be defined between the engine power and the power loss. This way the power due to total losses P_{loss} can be calculated with respect to the required power that is measured by the data acquisition system. In Fig.4b the estimated drag coefficient is plotted together with vehicle speed, the velocities below the 23m/s are filtered away in order to get the maximum constant velocity.

The average drag coefficient, based on a frontal area of $10.34m^2$, for the whole testing period of two months is 0.430. Within this estimation also the assumption is made that the vehicle does not generates downforce, which has an influence on the friction forces between the tires and the surface. Van Raemdonck [8] performed numerical simulations of a full scale symmetrical model of the same truck used during the data acquisition. A drag coefficient $C_D = 0.384$ was obtained after the numerical simulations. The difference between the estimated drag coefficient and the one simulated with the aid of computation fluid dynamics (CFD) is probably related to the fact that the model used during CFD was a simplified semi-model, not equipped with a radiator, no side-winds were simulated and the known short comings of the used turbulence model.

Power required contributions

All the different contributions in terms of percentage to the total power required P_{req} are known. Therefore it is possible to plot these contributions for a particular day, Fig.5a. At certain moments the total losses are reduced to zero, these are the moments when the truck driver releases the acceleration pedal position and the vehicle velocity drops. When the vehicle velocity is zero and the engine of the truck stays on, it is obvious that all power is lost to mechanical friction of the engine and axis.

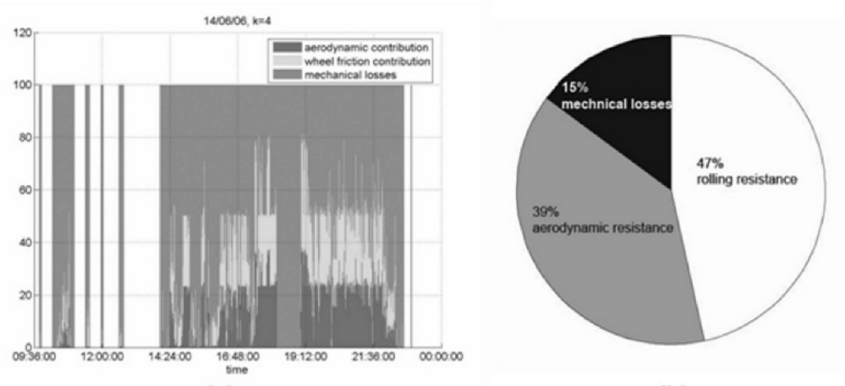

(a) (b)

Fig. 5 (a) Overview of the different contributions with respect to the delivered power; (b) Average contributions for the whole testing period considering velocities higher than 23 m/s.

If the average for the whole testing period is calculated for the three different contributions, a summarizing pie-chart, Fig.5b, can be made. The figure illustrates that almost 15% of the delivered power is lost into the mechanical friction of the engine, the gearbox and the drive shafts. The rolling resistance is responsible for 47% of the total delivered power, while the aerodynamic forces consume 39%. Only the vehicle velocities which are equal or higher than 23m/s are considered.

Vehicle speed and wind velocity

It is interesting to compare both velocities, the vehicle speed registered by the FMS system of the truck and the wind velocity measured by the WindSonic. Figure 6a immediately shows that the wind speed is often lower than the vehicle velocity whereas the opposite is to be expected due to acceleration of the flow by the rounded cabin edge and by the roof deflector. A possible reason for this lower wind speed can be the fact that the bent flow, due to the presence of the cabin edge, separates when it comes along the front edge of the WindSonic and causes a wake and lower velocities in the horizontal measuring plane of the sensor. Therefore the WindSonic is being tested in the wind tunnel. It turned out that even for major inclination angles up to 40 degrees no flow separation was occurring at the front edge of the Wind- Sonic and that the registered wind speeds and yaw angles were corresponding with speeds set through the wind tunnel. Numerical simulation of a full vehicle model of the cabin with roof and sun deflector together with the WindSonic can clarify the lower measured wind velocities. Another reason could be the fact that vehicle speed obtained through the FMS system is not correct. Unfortunately there was no access to the GPS data of the truck or a possibility of a short test run with the GPS of the truck at that moment to control the vehicle speed.

In order to prevent that the WindSonic is subject to an angle of incidence, the sensor should be placed far away from the front edge of the cabin edge. This is not possible for a truck due to practical and safety reasons and legislation.

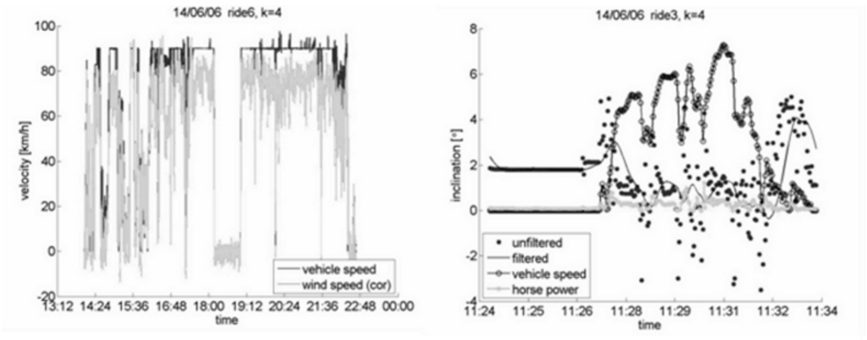

(a) (b)

Fig. 6 (a) Vehicle speed and wind velocity; (b) Inclination angle together with the vehicle speed and horse power.

Inclination and banking

During the analysis of the data from the 2-axis incline indicator it turned out that the sensor was suffering from the vibrations induced by the truck and its engine. Even after manipulating the data by filtering, it was not possible to indicate whether the truck is driving up- or downhill. The sensor was then mounted on the chassis with rubber connections in order to dampen the vibrations as can be seen in Fig.6b and which was not very helpful. The figure indicates the inclination angle together with the vehicle speed and the horse power. The constant inclination angle is always corresponding with a zero vehicle speed and horse power. This once again states that the inclination (and banking) angle is suffering from the vibrations initiated by the engine. It is then advisable to use a less sensitive sensor to indicate inclination and banking angles.

5 Discussion and Conclusions

Within a testing period of six weeks an enormous amount of information was collected and processed with the aid of an extensive self-written Matlab code in order to be able to interpret all the different parameters and their relation to each other.

Unfortunately a closer investigation of the registered inclination and banking angle and the wind speed revealed that these sensors are not suitable for their initial purpose. This type of 2-axis incline indicator is too sensible for vibrations due to its build-up. An inclination indicator which is constructed with other, less vibrations sensitive principles to measure an angle should give better and more reliable results in future testing activities.

The position of the WindSonic is unfortunate because the sensor is suffering from the bent flow due to the rounded cabin top front edge. The flow investigation and calibration in the wind tunnel gave more insight in the results of the WindSonic and its behavior in an inclined flow: no flow separation was induced at the WindSonic front edge even at an inclined flow of 40°. Further numerical simulations are required to explain the lower measured wind velocities. It is also advisable to use a wind sensor that measures the wind velocity in all three directions. Another option is to use a wind velocity and direction sensor which is mounted on a beam in front of the vehicle. This way the WindSonic can be calibrated with respect to the extra (correct) measurements. It is advisable to check the velocity difference by comparing the vehicle speed registered by the FMS system with a corresponding GPS signal.

During the test period a reference level of the truck is defined which makes it possible to compare different aerodynamic devices and their corresponding fuel economy impact. Also more insight in the aerodynamic (C_D value of 0.430) and mechanical performances (the power required is split into 47% rolling resistance, 39% of aerodynamic drag and 15% mechanical losses; fuel consumption of 30 liters in 100 km; average speed of 75 km/h) is obtained as well as in the behavior of the truck driver and its surroundings (the wind direction range of ±10° is most occurring).

Acknowledgments

The authors would like to acknowledge the support from Jan de Rijk Transport, Kees Mulder Carrosserieën and Squarell Technology. Additional thanks to Rose McCallen, Fred Browand, Jim Ross and ECI for the organization of The Aerodynamics of Heavy Vehicles II conference.

References

[1] Rose M J (1987) Commercial Vehicle Economy - The Correlation Between Aerodynamic Drag and Fuel Consumption of a Typical Truck. J of Wind Eng Ind Aerodyn, 9:89-100.
[2] Harwell and Didcot (2001). Truck Aerodynamic Styling. ETSU, Oxfordshire. http://www.energysavingtrust.org.uk/uploads/documents/fleet/GPG308.pdf
[3] Wood R M, Bauer S X S (2003) Simple and Low-Cost Aerodynamic Drag Reduction Devices for Tractor-Trailer Trucks. SAE paper 2003-01-3377.
[4] Gilhaus A M, Renn V E (1986) Driving-Stability-Related Aerodynamic Forces and Their Interdependence-Results of Measurements on 3/8-Scale Basic Car Shapes. SAE Technical Paper 860211.
[5] Gill Instruments Ltd. http://www.gill.co.uk/products/anemometer/windsonic.htm
[6] Squarell Technology. http://www.squarell.com
[7] AE Sensors. http://www.aesensors.nl/pdf/Seika/SB2I e.pdf
[8] Van Raemdonck G M R (2006) Design of an Aerodynamic Aid for a Tractor-Trailer Combination. Master’s thesis, Delft University of Technology, Faculty of Aerospace Engineering.

Automotive Testing in the DNW-LLF Wind Tunnel

Eddy Willemsen

German-Dutch Wind Tunnels (DNW), P.O. Box 175, 8300 AD Emmeloord, the Netherlands
eddy.willemsen@dnw.aero

Abstract The German Dutch Wind Tunnels is a foundation with the German Aerospace Center (DLR) and the Dutch National Aerospace Laboratory (NLR) as parent institutes. DNW operates ten aeronautical wind tunnels of DLR and NLR, located in Germany and the Netherlands. The main objective of the DNW organization is to provide the customer with a wide spectrum of wind tunnel test and simulation techniques, operated by one organization, providing the benefits of resource sharing, technology transfer, and coordinated research and development (R&D). The LLF is used for full-scale testing of trucks, buses, cars and alike. Heavy trucks are mounted in the 9.5m x 9.5m test section, whereby a wind speed of 60 m/s can be reached. The tested vehicle is connected to an external six-component balance with a resolution in drag measurement of 0.15N. In case of trucks, the front wheels and rear wheels are supported by air cushions. Flow visualization techniques (smoke, tufts, oil, laser light screen) are available, as well as PIV apparatus, pressure measurement equipment and an acoustic wall array for aerodynamic noise measurements. Smaller cars may also be tested with a moving ground plane of 10m long and 6.3m width. The belt has a maximum speed of 50 m/s. The poster will present an overview of the possibilities for automotive testing in the DNW-LLF wind tunnel.

Introduction

The German-Dutch Wind Tunnels (DNW) operates ten world class wind tunnels and one engine calibration facility of the German Aerospace Center (DLR) and the Dutch National Aerospace Laboratory (NLR). The main objective of the DNW organization is to provide its customers with a wide spectrum of wind tunnel test and simulation techniques, operated by one organization, providing the benefits of resource sharing, technology transfer, and coordinated research and development.

For a proper operation of the wind tunnels, it is of vital importance to keep the installations well maintained, but at the same time spend a sufficient amount of investment on the implementation of new measurement techniques. Over the years a continuous effort is made to offer customers the best quality of internal and external balances as well as electronically scanning pressure measurement systems, acoustic measurements, PIV technique and various flow visualization techniques.

Full-scale trucks and buses are tested in the LLF wind tunnel. Figure 1 shows a sketch of the layout of the LLF. This facility is located in the Netherlands, about 100 kilometers northeast from Amsterdam. At this site also a 37.5 percent scaled copy of the LLF is built. Figure 2 shows an aerial view of the testing site, where the two wind tunnels can be distinguished: the LST low in the middle and the large LLF in the upper right corner.

In fact, in the barn visible at the lower left corner a 10 percent pilot tunnel of the LLF is still operational and available and occasionally used for specific research concerning design matters of the LLF.

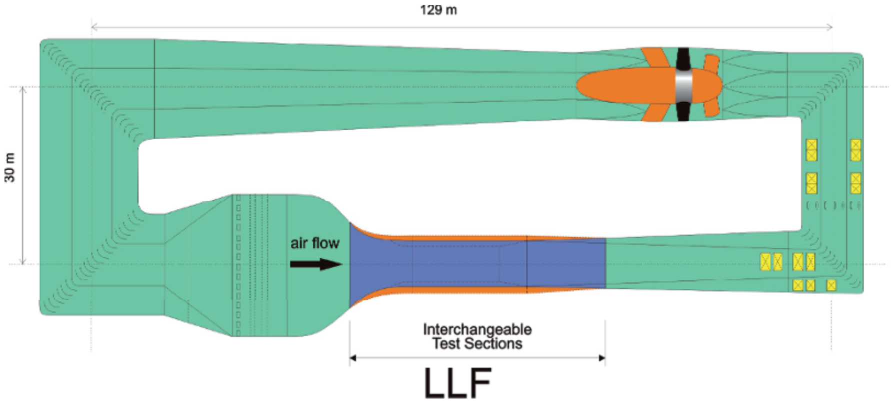

Fig. 1 Layout of the LLF

Test Setup

From the eleven different wind tunnels managed by DNW the largest wind tunnel LLF is suitable for full-scale testing of cars, buses and trucks.

The LLF is a closed loop atmospheric wind tunnel with interchangeable test sections of various dimensions. Large vehicles require the largest available test section of 9.5 m width and 9.5 m height. The cylindrical part of the test section is 20 m in length, succeeded by a transition part of 13 m in length between test section and a diffuser of 40 m length.

The 12.7 MW fan drive provides a maximum wind speed of 62 m/s. The flow quality is very good, with a turbulence level of less than 0.1 percent and velocity uniformity with less than 0.4 percent deviation from the centerline value.

Fig. 2 The LLF and LST wind tunnel

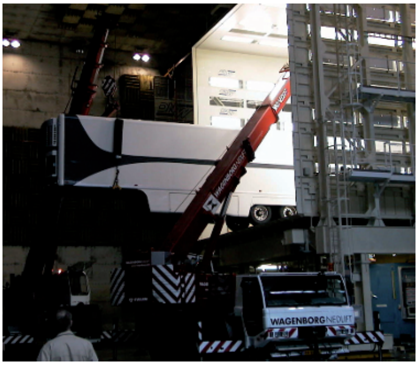

Fig. 3 Change of trailer

The drag is measured with the standard available external six-component platform balance, equipped with three horizontal and three vertical load cells. The horizontal load cells have a resolution of 0.15 N each, enabling accurate drag and side force measurements.

In the setup for trucks and buses, air cushions elements are mounted under the wheels to support the chassis. The height of these elements is kept very small in order to minimize the effect on the ground clearance. The air cushions are filled with pressurized air from a compressed air system. The vehicle is fixed by means of stiff struts to a supporting frame connected to the measuring part of the balance. The maximum yaw angle for an 18 m long truck is about 15°.

Figure 3 shows an action photo whereby the trailer is changed by means of two cranes during a test program.

Figure 4 shows a dimensional sketch of a truck mounted in the LLF test section at zero angle of yaw. The blockage is about 11 percent. In the 10 percent pilot tunnel of the LLF tests on models of a truck on four different scales were executed to determine a blockage correction specifically for trucks in the LLF.

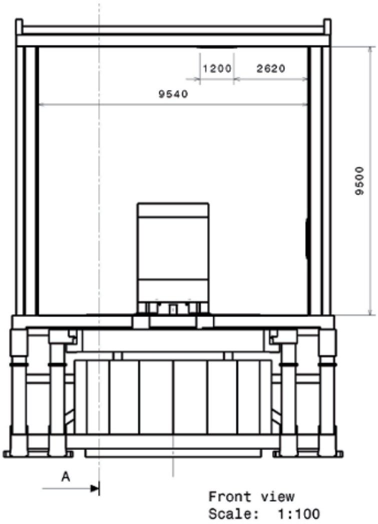

Fig. 4 Cross-sectional dimensions

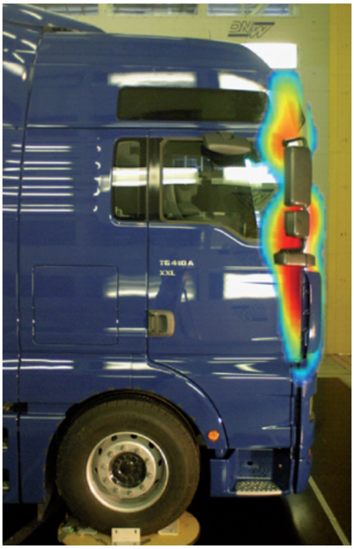

Fig.5 Acoustic test resluts

Test Equipment

At DNW all measuring techniques for aeronautical and aerospace testing are also available for tests on trucks, buses and the like.

The external balance provides the drag, side force and yawing moment.

Pressures can be measured with flat surface pressure taps, specially developed and manufactured for DNW.

Flow visualization can be realized with a hand-held smoke rod, with tufts, oil of different colors and laser light sheet.

Two microphone wall arrays may be used to measure the strength and location of acoustic sources. Figure 5 shows an example of test results, plotted in a side view photograph of a truck. The colors represent the strength of the sound production in the area of the side mirrors and corner vanes.

Beside standard testing techniques for trucks and buses DNW may also apply Particle Image Velocimetry or a traversing rake of eighteen five-hole pressure probes to obtain information about the flow field around the vehicle.

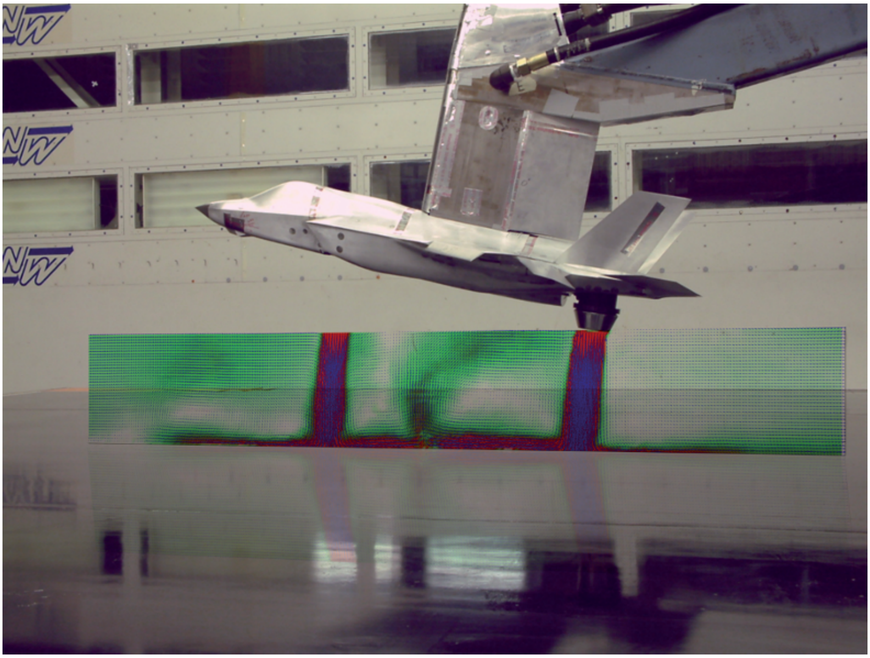

Fig. 6 Example of PIV results on a fighter aircraft

An Experimental Study of Tractor Base Bleed for Heavy Vehicle Aerodynamic Drag Reduction

Bruce Storms, Jason Ortega, Kambiz Salari

NASA Ames Research Center, USA
bruce.l.storms@nasa.gov

Abstract A significant contributor to heavy-vehicle aerodynamic drag is the tractor-trailer gap, especially when operating in a crosswind. At this condition, the freestream flow turns into the tractor-trailer gap, imparting a momentum exchange to the vehicle and subsequently increasing the aerodynamic drag. In common use today, tractor side-extenders provide significant drag reduction, but they are not without problems. Frequently damaged when the tractor pivots sharply with respect to the trailer, side extenders can incur additional costs for maintenance and repair. This issue can be alleviated by shortening extenders (thereby reducing their benefit) or devising an alternative drag-reduction concept. One such concept is tractor base bleed, in which air-flow is vented into the tractor-trailer gap through the back of the tractor. To study this concept, a wind-tunnel study was conducted for a generic 1:20-scale tractor-trailer configuration at width-based Reynolds number of 420,000. Delivered through a porous material embedded in the tractor base, the bleed flow was varied so as to generate velocities behind the tractor ranging from zero to 10% of the freestream velocity. Configurations were studied both with and without side extenders at two different tractor-trailer separation distances.

Application of High Fidelity Numerical Simulations for Vehicle Aerodynamics

Parviz Moin

Stanford University, USA
moin@stanford.edu

Abstract Interest in the use of the large eddy simulation (LES) technique for computation of turbulent flows of industrial relevance has increased considerably. This is in part due to the availability of low cost, powerful supercomputers. Today, a computer cluster capable of one TFOPS sustained performance for a complex flow LES calculation costs about one hundred thousand dollars. Another reason for the increased interest in LES is the recent added capabilities for multi-physics and integrated flow simulations. As part of Stanford's DOE/ASC program, we have demonstrated and validated high fidelity simulations of multi-phase reacting turbulent flows in highly complex configurations in propulsion systems. The overarching problem in this program is simulation of flow through a complete jet engine, which is an extremely complex machine. LES computations of the entire engine flow are not feasible even with the most advanced supercomputers available. The Reynolds averaged Navier-Stokes (RANS) technique was used for the turbomachinery components and the combustor was simulated using LES. These simulations provided an early example of integrated simulations where different codes with different fidelity compute different portions of the system. A simulation environment had to be developed for the various codes to communicate with each other in an efficient and stable fashion. This integration technology and the associated science are suggested as the means for using LES in vehicle aerodynamics where Reynolds numbers are too high for high fidelity computation of the flow around the entire vehicle. LES can then be used in regions where RANS models are known to be inaccurate, and where LES provides access to flow quantities such as turbulent pressure fluctuations for predicting noise. Several examples of integrated simulations will be presented, including separation control for a high-lift system using synthetic jets.

Scale-Adaptive Simulation in the Context of Unsteady Flow Simulations

Florian Menter

ANSYS/Fluent/CFX, Germany
florian.menter@ansys.com

Abstract In the last decade, the spectrum of methodologies for the modeling of unsteady flows has significantly increased. Historically, the two choices were Unsteady Reynolds Averaged Navier-Stokes (URANS) and Large Eddy Simulation (LES) methods. Both have severe limitations with respect to their application to engineering flows. URANS, typically produces no turbulent spectral information, even in regions, where time and space resolution would be sufficient to do so, whereas LES requires very high grid counts for modeling of wall-bounded flows at moderate to high Reynolds numbers. CFD users therefore had little choice than to concentrate on steady state RANS solutions, even for applications, where it was clear that these models are not adequate. Detached Eddy Simulation (DES) as proposed by Spalart in 1997, lead to a shift in paradigm, as it combined the elements of RANS and LES in a way that allowed the simulation of unsteady detached flows with available computing power. More recent studies by Menter and Egorov, have however shown that the inability of classical URANS models to resolve turbulent structures is not an inherent shortcoming of the URANS approach, but only related to the way the scale equations have historically been derived. After re-visiting an exact scale equation that Rotta had developed in the 1950s, it became clear that an important term was omitted in all scale equations, which resulted in the inability of classical RANS models to resolve unsteady structures. Closer inspection of Rotta's equation shows that the second derivative of the velocity field should be included in the length scale equation. This so-called Scale-Adaptive Simulation (SAS) methodology behaves in many ways and for many applications similar to the DES formulation, but avoids some of the dangers of DES. On the other hand, it is not the goal of SAS to replace DES and it will be shown that both methods have their place in the spectrum of unsteady turbulence models. The paper will discuss the practical implications, but also the limitations of the SAS technology. Many results produced during the European research project DESIDER on external aerodynamic flow will be shown.

Computational Simulation of the GCM Tractor-Trailer Configuration

K. Sreenivas, B. Mitchell, S. Nichols, D. Hyams, D. Whitfield

University of Tennessee SimCenter at Chattanooga, Chattanooga, TN 37403, USA
kidambi-sreenivas@utc.edu

Abstract Aerodynamic simulations were carried out for the Generic Conventional Model, a 1/8th scale tractor-trailer model, that was tested in the NASA Ames 7'x10' tunnel. The computed forces are compared for the zero, ten and fourteen degree yaw cases while the pressure coefficients are compared to experimental data for the ten and fourteen degree cases. A DES version of the one-equation Menter SAS is used in these simulations. Overall forces as well as pressure distributions matched well for the fourteen degree case. For the ten degree case, the forces were in reasonable agreement while the pressure distributions indicated a need for tighter grid resolution as well as possibly advanced turbulence models.

Introduction

In 1997, fuel consumption among Class 8 trucks was 18 billion gallons [1]. At typical highway speeds (70 mph), 65% of the overall output of the engine is used for overcoming aerodynamic drag [2]. Consequently, a reduction in aerodynamic drag will result in substantial fuel savings. Given the large number of tractor/trailers on the road in the United States, this could translate into a significant reduction in domestic fuel consumption as well as a reduction in emissions that contribute to pollution.

The main contributors to the aerodynamic drag are the gap between tractor and trailer, the vehicle underbody and the base flow region of the trailer [3]. Significant flow structures exist in these regions and several experimental studies have been carried out to characterize them. One of the experimental studies used a 1/8th scale Ground Transportation System (GTS) model that consisted of simplified tractor trailer geometry with a cab-over-engine design and no tractor-trailer gap. This geometry was tested both at the Texas A&M University Low Speed Wind Tunnel [4]as well as the NASA Ames 7'x10' tunnel [5]and extensive data was collected for validation of computational simulations. Modifications to the GTS geometry to include a tractor trailer gap were incorporated in tests carried out at USC [6] and the influence of the gap on the overall flowfield assessed. Detailed experimental studies were also carried out on a realistic tractor trailer combination, the Generic Conventional Model (GCM), in the NASA Ames 7'x10' as well as the 12' wind tunnel [7].

Computational studies aimed at evaluating the capabilities of current flow solvers for the prediction of heavy vehicle aerodynamics were carried out by a number of researchers [8]-[13]. Salari et al. [8] used the data from the GTS experiments and showed that with an appropriate choice of turbulence model, the overall drag coefficient could be predicted with reasonable accuracy. However, one of their key findings was that the details of the flow field, especially in the base flow region, were not being captured accurately. Pointer [9] used a commercial CFD flow solver to study the GCM model in the 7'x10' tunnel and the results indicated that the overall drag coefficient could be predicted with reasonable accuracy. However, no detailed flow field comparisons were presented. Maddox et al. [10] used another commercial CFD solver to simulate the flow around GTS model. They employed a detached eddy simulation (DES) approach and showed that an improvement in the predicted pressure (especially toward the base of the model) can be achieved. RANS simulations using the one-equation Spalart-Allmaras model and the two-equation Menter k-ω model were reported by Roy et al. [11]. LES simulations of a truncated GTS model were carried out by Ortega et al. [12]. Sreenivas et al. [13] simulated the flow field around the GTS model using an unstructured flow solver. They employed the DES version of the two-equation k-ε/k-ω turbulence model and showed that a single vortex structure that was observed experimentally could be reproduced by time-averaging an unsteady RANS simulation.

The present research effort focuses on *Tenasi*, a family of structured and unstructured flow solvers that have been developed at the University of Tennessee SimCenter at Chattanooga. The unstructured flow solver is used to simulate the flowfield around the GCM model inside the NASA 7'x10' tunnel at zero and ten degrees yaw. Results are presented comparing the axial and side forces as well as surface pressures with experimental data.

Numerical Approach

The governing equations solved by the *Tenasi* flow solver are the non-dimensional form of the Navier-Stokes equations in Cartesian coordinates. The variables appearing in the Navier-Stokes equations are nondimensionalized as follows: density ρ_r; velocity U_r; temperature T_r; pressure $\rho_r U_r^2$; length L_r; time $\frac{L_r}{U_r}$; energy and enthalpy h_r. This system of equations is closed by an equation of state the form $\rho = \rho(p,T)$. For a perfect gas with constant specific heat, $h_r \equiv C_p T_r$, and it follows that $E_c = (\gamma - 1) M_r^2$ where $M_r = \frac{U_r}{c_r}$ is a reference Mach number and $c_r^2 = \gamma R T_r$ is the reference speed of sound. $\gamma = \frac{C_p}{C_v}$ is the ratio of specific heats, and R is the specific gas constant. The equation of state is then given by

$$p = \frac{\rho T}{\gamma M_r^2} = \frac{\rho c^2}{\gamma}; c^2 = \frac{T}{M_r^2}$$

The governing equations are discretized using a node-centered, finite-volume approach. A single parameter based preconditioner is employed so that the baseline *Tenasi* solver is applicable over a wide range of Mach numbers. The numerical fluxes are computed using high resolution fluxes based on Roe averaging and a Newton subiteration procedure is employed to ensure time accuracy. The linear system at each time step is solved using a Symmetric Gauss-Seidel algorithm. The details of the numerical algorithm are available in Sreenivas et al. [14].

Results

The results presented here include the GCM at zero, ten and fourteen degree yaw. These were three of the test cases chosen from the available experimental data. The simulations were carried out to include the NASA Ames 7'x10' tunnel as well as the GCM geometry. The reason for this was the experimental pressure coefficient was referenced to a specific location on the test section wall and including the tunnel was an easy way of comparing computed and experimental pressure distributions. The grids for all the cases were generated using a combination of Gridgen (for the tetrahedral portion) and HUGG [15] (for inserting the viscous layers). The characteristics of the grids used are detailed in

Table 1.

Table 1 Grid Characteristics for the zero, ten and fourteen degree yaw cases for the GCM inside the 7'x10' Tunnel

Case	Nodes	Tetrahedral	Prism	Hex
0° yaw	20,636,180	40,366,718	25,870,856	680,800
10° yaw	18,937,191	41,828,550	23,253,152	0
14° yaw	19,842,249	42,832,190	24,564,782	0

All the cases presented here at a Reynolds number of 1.15×10^6 (based on GCM model trailer width of 12.75 inches) and a tunnel test section Mach number of 0.15. Given the (relatively) high freestream Mach number that is present in the GCM experiments, a single parameter based preconditioned formulation is used to avoid any convergence difficulties associated with using a pure compressible flow solver. A quadratic reconstruction procedure was used to ensure higher order spatial accuracy while three Newton iterations were employed to ensure second order accuracy in time. The Menter SAS turbulence model in DES mode was used to model the effects of viscosity and the average y^+ for all the viscous surfaces were less than unity. A typical run consisted of running 5,000 time steps in a constant CFL mode (CFL of 25.0) followed by 20,000 time steps in a constant time step mode, with the non-dimensional time step being 10^{-3}. Each run required about 2 days of CPU time and utilized 200 cores.

The computed axial and side forces were compared to two sets of experimental data (Runs 43 and 75) and the comparisons are shown in Figs. 1 and 2. As can be seen from Fig. 1, there is an indication of large scale separation (indicated by an abrupt change in the axial force coefficient) in the experimental data between approximately 10^o and 12.5^o angles of yaw. Furthermore, the experimental data is asymmetric between positive and negative yaw angles and between the two runs. The computed axial force coefficient agrees well with experimental data for the zero and fourteen degree yaw cases. For the ten degree case, the computed axial force is lower than the experimental values. Correspondingly, the side forces are higher than the experimental values for the ten degree case (Fig. 2). This could be caused by separation occurring slightly earlier in the computations as compared to the experiment. Given the uncertainty in the experimental values at ten degree yaw, the overall agreement between the computed and experimental axial and side forces is good.

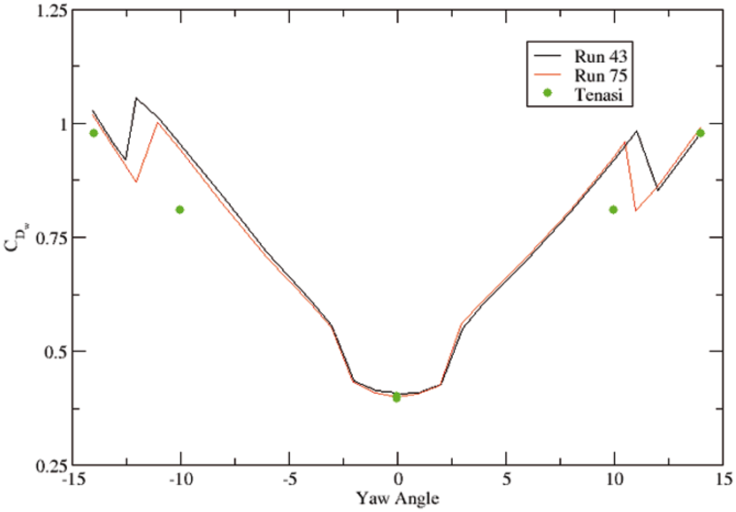

Fig. 1 Comparison of Axial Force Coefficient

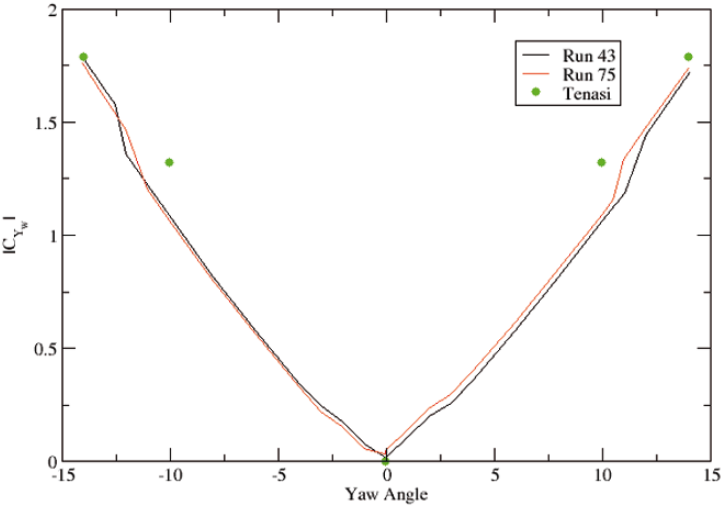

Fig. 2 Comparison of Side Force Coefficient

Detailed comparisons of surface pressure distributions are shown in Figs. 3 – 12 for the ten and fourteen degree yaw cases. The zero degree case results have been omitted for brevity. The experimental data shown in these graphs includes results from both the positive and negative yaw runs. The decision to include both sets of data was based on a couple of reasons:

(1) To get a measure of geometric asymmetry and experimental uncertainty: If the geometry and flow conditions were truly symmetric, then the values from the positive and negative yaw angles should be the same. Therefore any differences between the measured pressures would be an indication of geometric asymmetry and also provide a measure of experimental uncertainty.

(2) The instrumentation was not symmetric: The GCM model had more pressure taps on one side of the geometry relative to the other. Therefore, using data from both positive and negative yaw angles would enable an assessment of the computed solution.

Ten Degree Yaw

For the results presented here, the solutions were averaged over 1000 and 5000 time steps. The choice of time step in this particular instance was arbitrary; however, in a related study, an effort to define a convergence criterion for unsteady flows has been attempted with reasonable success [16]. This criterion was not employed in this study as it required the storage of considerable amount of data (on the order of a terabyte). Figures 3 and 4 show a comparison of pressure distribution along the centerline of the tractor. As can be seen from the figures, the agreement is very good between the experimental data and computations. The effect of the choice in averaging period can be seen in both the plots. The 5000 time-step averaged solution appears to match the experimental data slightly better than the 1000 time-step averaged solution. There also appears to be a significant discrepancy between the experimental data around the x/w = 1.5 or so (close to the base of the tractor). The computations match the +10° yaw results very closely in this area. Overall, the computations seem to lie between the experimental data over the bulk of the centerline of the tractor.

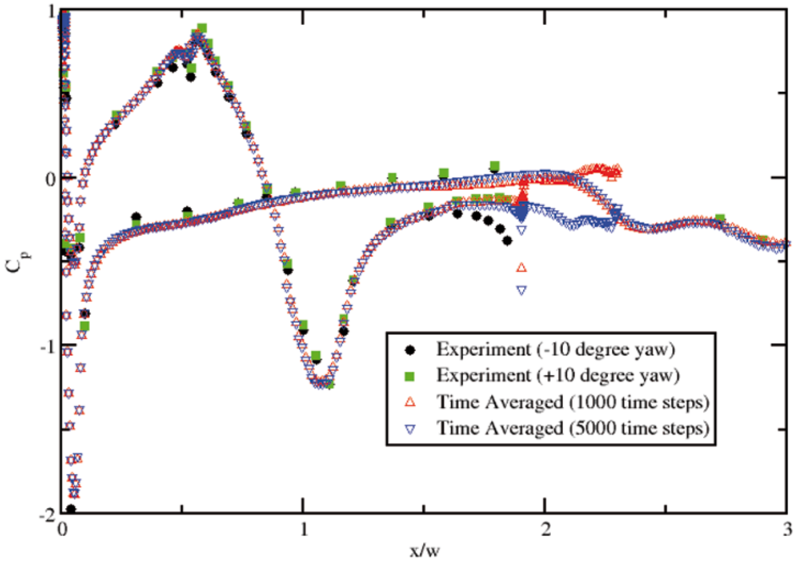

Fig. 3 Comparisons of Tractor Centerline Pressure Distribution along the x-axis for 10° yaw

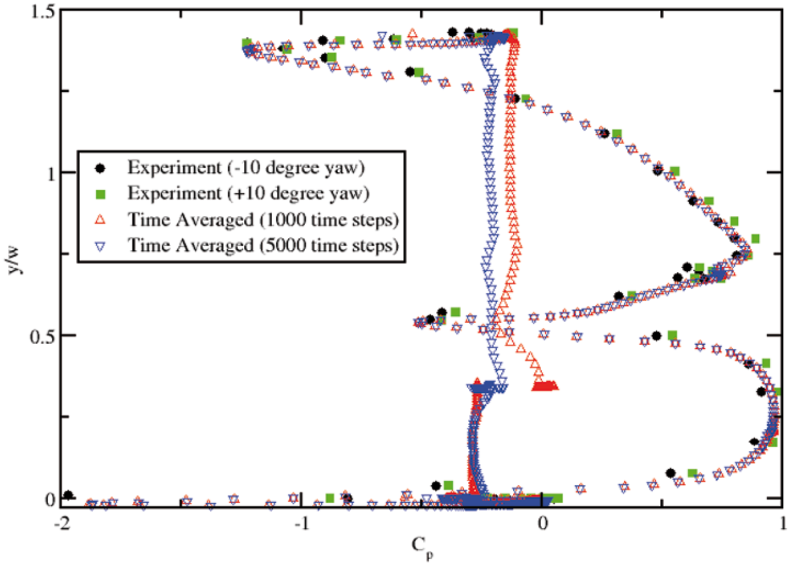

Fig. 4 Comparisons of Tractor Centerline Pressure Distribution along the y-axis for 10^o yaw

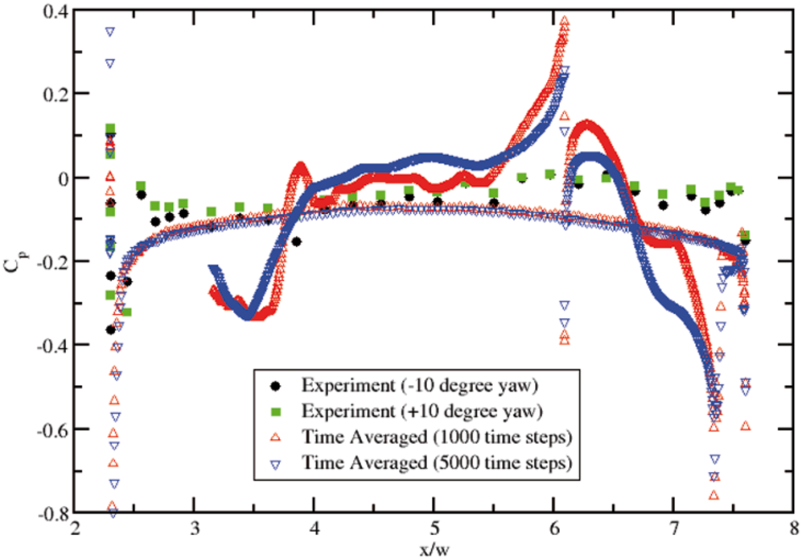

Fig. 5 Comparisons of Trailer Centerline Pressure Distribution (Top of trailer) for 10^o yaw

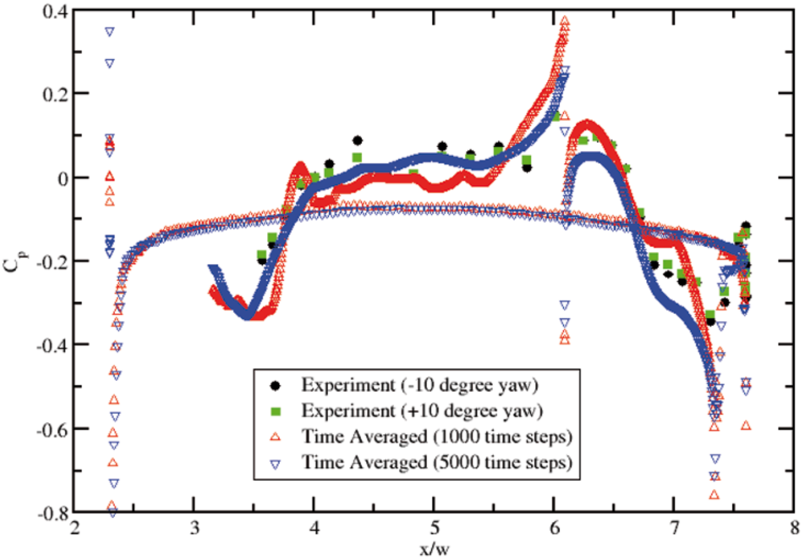

Fig. 6 Comparisons of Trailer Centerline Pressure Distribution (Bottom of trailer) for 10° yaw

A comparison of the trailer centerline pressure distribution is shown in Figs. 5 and 6. The data is presented in two different graphs for clarity. The computational results are repeated between the figures, while only the top of the trailer data is shown in Fig. 5 and only the bottom of the trailer is shown in Fig.6. As can be seen from Fig. 5, the trend towards the base of the trailer is not captured correctly by the computed results. There is also no significant difference between the 1000 and 5000 time-step averaged solutions. It is possible that the base flow region has a very strong influence on the pressure distribution in the neighborhood of the trailer base. The comparison for the bottom of the trailer fares much better with the trend as well as the magnitude of the pressures being captured reasonably well (especially the 5000 time-step averaged solution).

The next comparison shown is for a line that is halfway up the side of the trailer (Fig. 7). As can be seen from the figure, the experimental data from the ±10° yaw provides a better picture of the overall pressure distribution on the trailer. The computations are reasonably close to the experimental data over the bulk of the trailer. The 5000 time-step averaged solution has smoothed out a lot of the fluctuations that are visible in the 1000 time-step averaged solution. The biggest discrepancy between the computed results and experimental data is at the front corner of the trailer. The experimental data seems to indicate a larger low pressure region (possibly caused by a large-scale vortex) while the computations indicate a much smaller low pressure region. Again, the 5000 time-step averaged solution compares much better to the experimental data than the 1000 time-step averaged solution. This discrepancy could account for some of the variation in the axial and side forces between the computed results and experimental data.

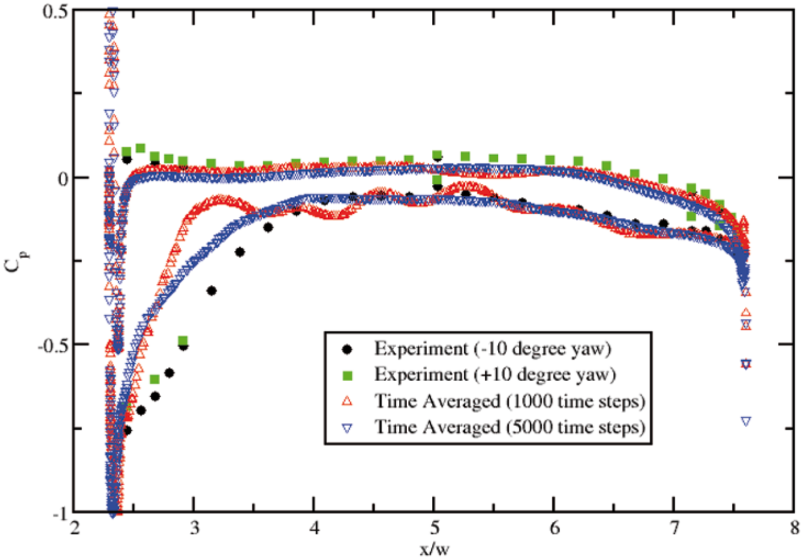

Fig. 7 Comparison of Trailer Pressure Distribution (y/w = 0.9137) for 10° yaw

Fourteen Degree Yaw

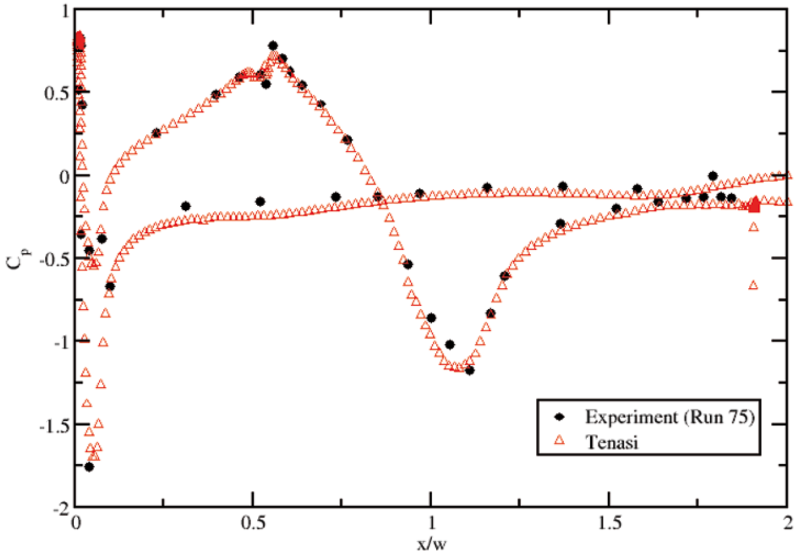

Fig. 8 Comparisons of Tractor Centerline Pressure Distribution along the x-axis for 14° yaw

An identical set of results is presented for the fourteen degree case as was done earlier for the ten degree case. This is done in an attempt to understand the similarities and differences between the solutions and also to shed light on the better agreement between the computed forces for the fourteen degree case as opposed to the ten degree case. Since the results for the ten degree case showed a better agreement between the 5000 time-step averaged solutions and experiment, only the 5000 time-step averaged results are presented for the fourteen degree case.

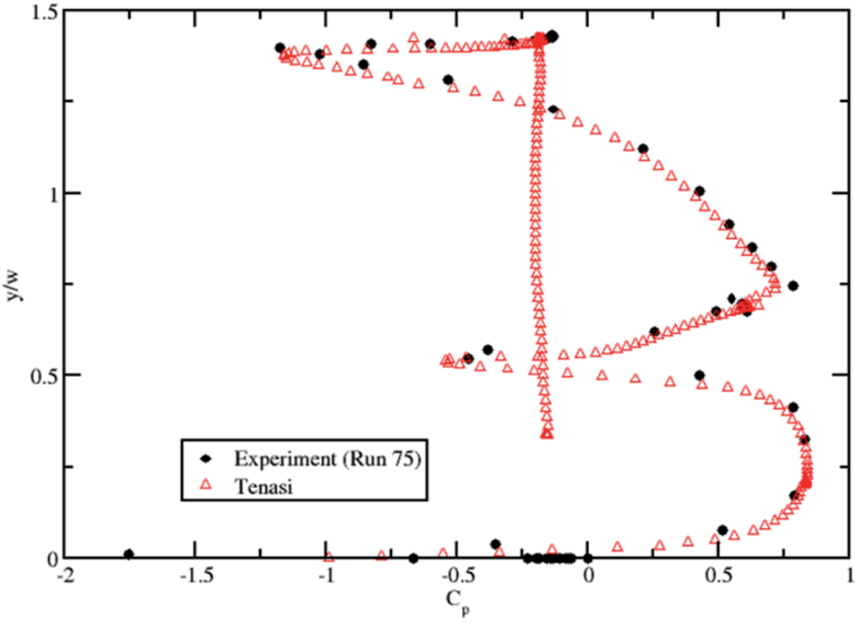

Fig. 9 Comparisons of Tractor Centerline Pressure Distribution along the y-axis for 14° yaw

The first sets of results are for the pressure distributions along the centerline of the cab and are shown in Figs. 8 and 9. The overall agreement in the pressure distribution is good and compares well with the agreement obtained for the ten degree case. The trailer centerline pressure distributions are compared in Figs. 10 and 11. As can be seen from these figures, the differences between the experimental data for the positive and negative yaw angles are quite evident with the computed data matching well with the -14° data over the front half of the trailer top surface (Fig. 10). The discrepancy in the pressure distribution over the back half of the top surface of the trailer is similar to that observed for the ten degree case; however, the magnitude here is much smaller than the ten degree case. The overall agreement over the bottom of the trailer centerline is similar to that obtained for the ten degree case.

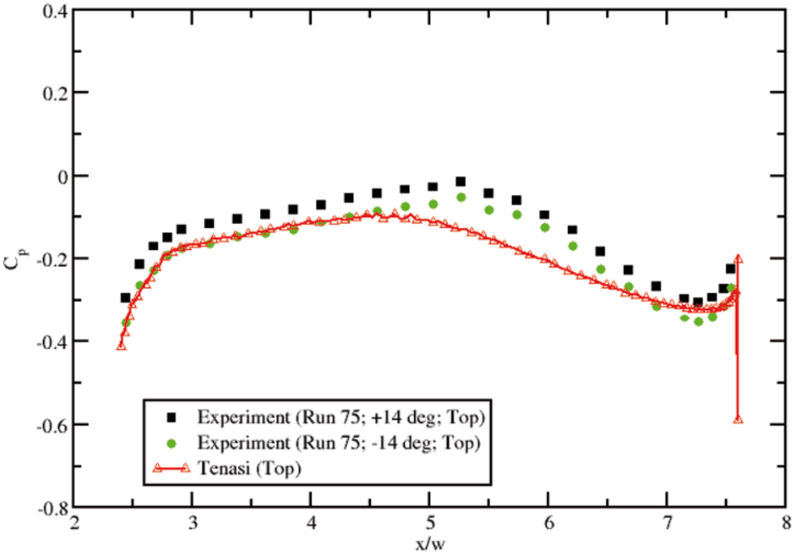

Fig. 10 Comparisons of Trailer Centerline Pressure Distribution (Top of trailer) for 14° yaw

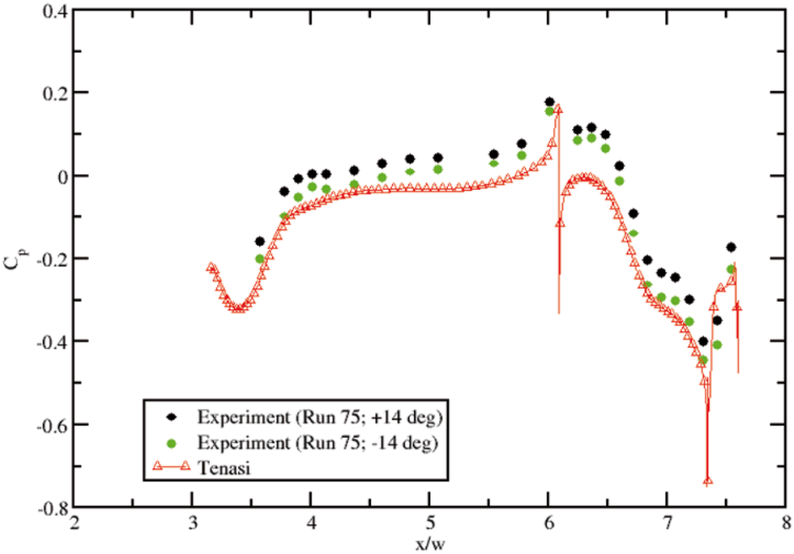

Fig. 11 Comparisons of Trailer Centerline Pressure Distribution (Bottom of trailer) for 14° yaw

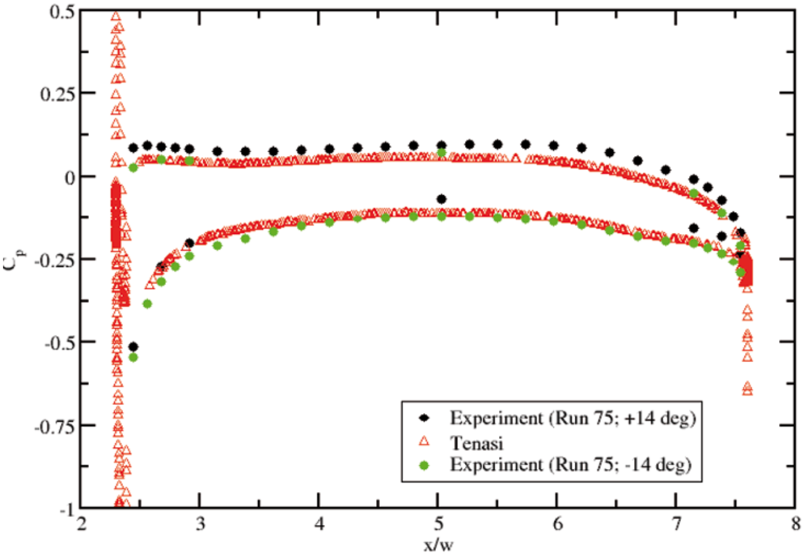

Fig. 12 Comparison of Trailer Pressure Distribution (y/w = 0.9137) for 14° yaw

The comparison of pressure distributions at the mid-plane (in the vertical direction) of the trailer are shown in Fig. 12. The overall agreement between the experimental data and computed results is good with the -14° data matching the computed results well. The biggest differences between the ten and fourteen degree cases can be seen by comparing Figs. 7 and 12. In the ten degree case (Fig. 7), the computed results are clearly not predicting the flow at the front of the trailer correctly while in the fourteen degree case (Fig. 12), there is good agreement everywhere. This could explain the differences in the agreement of the computed forces between the ten and fourteen degree cases.

Conclusions

Computed forces and pressure coefficient distributions were compared to experimental data for the GCM tractor-trailer configuration for ten and fourteen degrees yaw. Good agreement was obtained for the fourteen degree case while the ten degree case was in fair agreement with experimental data. The ten degree case pointed to the potential need for grid refinement in specific regions of the computational domain. It is also possible that the overall agreement for all the test cases could be improved by employing advanced turbulence models.

Acknowledgements

This work was supported in part by the US Department of Energy and the Oak Ridge National Laboratory through UT-Batelle contract number 4000035270 with Dr. W. Keith Kahl as technical monitor. This support is gratefully acknowledged. Thanks are also due to Dr. Rose McCallen, Dr. Jules Routbort and the late Dr. Sid Diamond for their generous guidance and encouragement. This work was also supported by the THEC Center of Excellence in Applied Computational Science and Engineering with Dr. Harry McDonald as technical monitor. Their support is greatly appreciated.

References

1 http://www.transportation.anl.gov/research/technology_analysis/truck_fuel_use.html
2 McCallen R, Couch R, Hsu J, Browand F, Hammache M, Leonard A, Brady M, Salari K, Rutledge W, Ross J, Storms B, Heineck J, Driver D, Bell J, and G Zilliac, "Progress in Reducing Aerodynamics Drag for Higher Efficiency of Heavy Duty Trucks(Class 7-8)," SAE Paper 1999-01-2238.
3 Cooper K, "Truck Aerodynamics Reborn – Lessons from the Past," SAE Paper 2003-01-3376, 2003.
4 Croll R, Gutierrez W, Hassan B, Suazo J and Riggins A, "Experimental Investigation of the Ground Transportation Systems (GTS) Project for Heavy Vehicle Drag Reduction," .SAE Paper 960907, February 1996.
5 Storms B, Ross J, Heineck J, Walker S, Driver D and Zilliac G, "An Experimental Study of the Ground Transportation System (GTS) Model in the NASA Ames 7-by 10-Ft Wind Tunnel," NASA/TM-2001-209621, February 2001.
6 Arcas D, Browand F and Hammache M, "Flow Structure in the Gap Between Two Bluff Bodies," AIAA Paper 2004-2250, June 2004.
7 Storms B, Satran D, Heineck J, Walker S, "A Summary of the Experimental Results for a Generic Tractor-Trailer in the Ames Research Center 7- by 10-Foot and 12-Foot Wind Tunnels," NASA TM-2006-213489, July 2006.
8 Salari K, Ortega J, and Castellucci P, "Computational Prediction of Aerodynamic Forces for a Simplified Integrated Tractor-Trailer Geometry", AIAA Paper 2004-2253, 34th AIAA Fluid Dynamics Conference and Exhibit, Portland, Oregon, June 2004.
9 Pointer D, "Evaluation of Commercial CFD Code Capabilities for Prediction of Heavy Vehicle Drag Coefficients," AIAA Paper 2004-2254, June 2004.
10 Maddox S, Squires K, Wurtzler K and J Forsythe, "Detached-Eddy Simulation of the Ground Transportation System," *The Aerodynamics of Heavy Vehicles: Trucks, Buses and Trains*, Springer, 2004, pp 89-104.
11 Roy C, Payne J, McWherter-Payne M and Salari K, "RANS Simulations of a Simplified Tractor/Trailer Geometry," *The Aerodynamics of Heavy Vehicles: Trucks, Buses and Trains*, Springer, 2004, pp 207-218.
12 Ortega J, Dunn T, McCallen R and Salari K, "Computational Simulation of Heavy Vehicle Trailer Wake," *The Aerodynamics of Heavy Vehicles: Trucks, Buses and Trains*, Springer, 2004, pp 219-233.

13 Sreenivas K, Pankajakshan R, Nichols D, Mitchell B, Taylor L and Whitfield D, "Aerodynamic Simulation of Heavy Trucks with Rotating Wheels," AIAA Paper 2006-1394, January 2006.
14 Sreenivas K, Hyams D, Nichols D, Mitchell B, Taylor L, Briley W and Whitfield D, "Development of an Unstructured Parallel Flow Solver for Arbitrary Mach Numbers," AIAA Paper No. 2005-0325, January 2005.
15 Karman S, "Unstructured Viscous Layer Insertion Using Linear-Elastic Smoothing," AIAA Paper 2006-0531, January 2006.
16 Pankajakshan R, Sreenivas K, Mitchell B and Whitfield D, "CFD Simulation of Class 8 Trucks," SAE Paper 2007-01-4293, October 2007.